SCALE EFFECT ON THE SHEAR BEHAVIOR OF A FRACTURE IN THE DIRECT SHEAR TEST

AUSAMA ALI GIWELLI
A5GD5203

August 2010

Doctoral Thesis
Geosystem and Energy Sciences Course
Graduate School of Environmental Studies
Tohoku University

ABSTRACT

Over the past decade, considerable efforts have been made to better understand the mechanical behavior of a fracture since it governs that of rock mass. Fractures in rock mass range in scale from a microfissure to a large fault system. Therefore, size effect on the mechanical behavior of a fracture has to be considered when estimating the mean aperture and the hydraulic conductivity of a fracture under stress. Previous studies showed that the closure of a fracture at a given normal stress significantly increases with fracture size. This effect can be attributed to an increase with fracture size in the standard deviation (SD) of the aperture, which gives a measure for the matedness of the fracture. For a sheared fracture, it has also been numerically shown that the SD of the aperture of a sheared fracture increases with fracture size when shear displacement is greater than a certain percentage of the fracture size, since the matedness of the fracture decreases with fracture size. Accordingly, fracture size may affect the shear behavior of a fracture. There have been a few experimental studies on the size effect on the mechanical behavior of a fracture under both normal and shear stresses. However, the aperture of the fracture has been rarely measured in these studies, and accordingly the mechanism for the size effect has not yet been well understood, whereas understanding of the aperture evolution during shear may be a prerequisite to clarifying the mechanism for the size effect on the mechanical behavior of a sheared fracture.

In this work, a decision was made to investigate the effects of size and normal stress on the shear behavior of a single tensile fracture by using the direct shear test (DST), but it should be mentioned that the DST has been criticized for the non-uniform distributions of the stress and deformation in a fracture, which may affect the estimation of the hydraulic properties of the fracture, since non-uniform normal stress may cause non-uniform closure. Therefore, in this study, both analytical and experimental investigations were performed.

First, a 3D FEM analysis with quadratic joint elements as a fracture model was performed for a limited case of a set of normal and shear stresses (σ_n = 10 MPa and τ = 7 MPa) 1) to examine the validity of the DST for a rock fracture by analyzing both the stress and deformation in a fracture and 2) to clarify the effects of specimen height on the stress and deformation in a fracture. The results obtained from the simulation showed that the normal and shear stresses are significantly concentrated near the end edges of the fracture, while they are fairly uniform in the central part of the fracture plane. Although the closure value is greater near the edges of the fracture, where the normal stress is concentrated, this concentration of the closure is not so significant due

to the non-linear behavior of the closure. According to the simulation result, the practical specimen height was determined for the standard height to be used throughout this work, and a compact direct shear test apparatus was designed and constructed.

Second, in order to study the effect of size and shear displacement on the shear behavior of a single facture, a tensile fracture was created in granite with sizes of 100 mm × 100 mm, 150 mm × 150 mm and 200 mm × 200 mm, and the direct shear tests were performed with a normal stress of 10 MPa. In this experiment, normal and shear stresses were unloaded at designated shear displacements and the change in the surface topography was measured by using a non-contact surface profile measurement system with a laser profilometer, to determine the evolution of surface damage and aperture during shear. The results showed that the SD of the initial aperture increases with both shear displacement and fracture size. As a result, the closure curve tends to become more non-linear with shear displacement since the matedness of the fracture surfaces decreases with shear displacement. Thus, shear dilation is not only governed by the surfaces sliding over, but the increase in the non-linearity of the closure curve with shear displacement also has significant effects on shear dilation. Furthermore, the results showed that the normal and shear stiffnesses in the initial stage decrease with fracture size because the matedness decreases as the SD of the initial aperture increases with fracture size. However, the shear stiffness in the residual stage increases with fracture size. This can be attributed to the fact that only small asperities with short wavelengths are mainly damaged by shear, as indicated by the change in the PSD of the surface heights during shear. Additionally, the damaged zones are enlarged and localized with shear displacement, and tend to form perpendicular to the shear displacement.

Finally, to clarify the effect of normal stress and gouge material on the shear behavior of a fracture, a tensile fracture in granite were reproduced by using mortar replicas with sizes of 100 mm × 100 mm, 150 mm × 150 mm and 200 mm × 200 mm, and the fracture replicas were tested in the direct shear test under two different values of normal stress (0.3 and 1 MPa) and shear displacements of 2 and 20 mm with and without cleaning the gouge materials that were produced during shear. The results showed that the SD of the initial aperture increases with normal stress since the matedness decreases due to the increase in the damage of the asperities as the normal stress increases. Moreover, the normal stiffness decreases with normal stress because the matedness decreases as the SD of the aperture increases with normal stress. Consequently, the non-linearity in the closure curve increases with normal stress. The results also showed that the non-linearity of the closure curve increases with gouge material. Therefore, the

normal stiffness decreases with the presence of gouge material. Since almost all numerical simulations have neglected such effect of gouge material that is produced by shearing on the closure curve, the closure curve obtained in the simulation should have been underestimated.

Keywords: Finite element method (FEM); Direct shear test; Cyclic shear loading; Shear stress Closure; Normal stress; SD of the initial aperture; Damage zones; Asperity degradation

CONTENTS

1. INTRODUCTION

1.1 Background and motivation

A fracture consists of two rough surfaces that are in partial contact under stress. The surface roughness produces a void space between the fracture surfaces having typically sparse contact areas with a complex geometry. The mechanical response of fractures is strongly related to the amount and geometry of the contact area, while the hydrological response is governed by the connectivity and size of the voids. Changes in the state of the stress in a rock mass, due to both natural changes and those induced by engineering activities, can have a substantial effect on fluid flow and material/heat transport with the fluid.

Accurate understanding of fluid flow through a rock fracture is the most fundamental and essential issue for the progress of the earth's crust in environmental science. The prediction of the mechanical and hydraulic properties of rock mass is essential for designing rock structures and safety assessment in various engineering projects such as underground disposal of high-level radioactive waste, construction of dams, CO_2 disposal, as well as the development of petroleum and geothermal energy reservoirs. As a consequence, many rock mechanics researchers have focused on the mechanical and hydraulic properties of rock fractures during the last decade [1-4].

Brown [5] showed that a fracture that is closed macroscopically due to normal rock stress may, nevertheless, provide a path for fluid flow because the fracture surfaces do not match perfectly and an aperture exists between the surfaces. Thus, aperture distributions in a fracture are governed by the rock stresses, the mechanical properties of rock, and the topography of the fracture surfaces.

In this study, the initial aperture of a fracture was defined as the thickness of the void space when the fracture surfaces are in contact at a single point. Fig. 1.1 shows the definition of a fracture aperture. As a matter of fact, there are many experimental difficulties in precisely evaluating the apertures of a large fracture, which is also time consuming. Hence, most studies on the mechanical and hydraulic properties of a fracture have been conducted using small samples in the laboratory.

Bandis et al. [6] investigated size effect on the shear behaviors of natural joint replicas by performing the direct shear test. The results showed significant scale effects on both the shear strength and deformation characteristics. Tanoli and Stesky [7] studied the effect of surface roughness and rock type on fracture closure under uniaxial stress of about 30 MPa. The results showed that the amount of fracture closure at a given normal stress largely depends on the rock type as well as on the facture surface roughness.

Matsuki et al. [8] investigated the size effect of a small-scale hydraulic fracture on the mean and standard deviation (SD) of the aperture. Raven and Gale [9] studied the effect of sample size ranging from 100 mm to 249 mm in diameter on the closure and permeability of a natural fracture in granite under uniaxial compression of up to 30 MPa. The results showed that the closure of the fracture tends to increase with the sample size and that the fracture flow rate decreases with an increase in the sample size. Yoshinaka and Yamabe [10] experimentally investigated the deformation of artificially created joints with different roughness and different sizes ranging from 60 mm to 422 mm. They showed that the normal stiffness decreases with the joint size and the maximum closure increases approximately in proportion to the joint size. Fardin [11] studied the size effect on the morphological and hydromechanical behavior of the rock fractures by conducing several normal loading and direct shear tests on concrete fracture replicas of different sizes. Marache et al. [12] studied the closure behavior of a fracture under normal stress by using approaches based on both experimentation and model analysis. They discussed the influence of fracture size on the closure curve, the normal stiffness and the contact area.

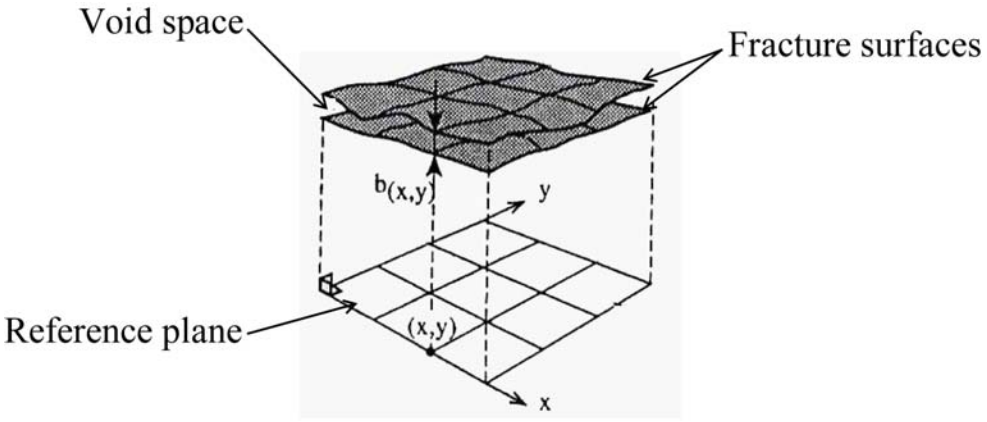

Fig. 1.1. Definition of a fracture aperture, b(*x*,*y*) (Hakami, 1995).

Most recently, Giwelli et al. [13] have shown that the closure of a fracture at a given normal stress significantly increases with fracture size and that this effect can be attributed to an increase in the SD of the aperture with fracture size, since the SD of the aperture gives a measure for the matedness of the fracture. It should be mentioned that the closure of a fracture is a highly non-linear function of stress and levels out to an asymptotic value at high values of the stress. This non-linear behavior is mainly due to complex development of the contact area during loading/unloading process [14].

However, most of the fractured samples used in the previous studies were small in comparison with real natural fractures that can be larger than one meter. This difficulty could be overcome by using large synthetic fractures created on a computer based on the frequency characteristic of the surface roughness and the matedness of a fracture [15, 16]. In recent years, Matsuki et al. [17] clarified the size effect on the aperture and permeability of a large synthetic fracture of up to 12.8 m × 12.8 m, which were created on a computer based on data for a tensile fracture with a size of 1 m [18]. They reported that the SD of the aperture of a sheared fracture increases with fracture size when shear displacement is greater than a certain percentage of the fracture size, since the matedness of the fracture decreases with fracture size. Additionally, they proposed an empirical formula for estimating the permeability of a large fracture from the SD of the initial aperture as well as the mean aperture for fractures during both normal closure and closure after shearing.

In general, to estimate the permeability of a given fracture under given normal and shear stresses, it is necessary to estimate the mean aperture of the fracture by determining the closure/opening of the fracture under both stresses. On the other hand, the fact that the SD of the initial aperture shows a size effect suggesting that the closure/opening of a fracture under normal and shear stresses may also depend on the fracture size because the mechanical behavior of a fracture is governed not only by the initial aperture distribution but also by the mechanical properties of rock [17]. Accordingly, to estimate the mean aperture of a fracture, the size effect on the mechanical behavior of a fracture should be taken into consideration.

In fact, there have been only a few experimental studies on the size effect on the mechanical behavior of a fracture under both normal and shear stresses (e.g. [6, 11, 19, 20]). However, the surface topography of the fracture during shear has not been measured in these studies, and consequently, the mechanism for the size effect is not yet well understood. Understanding the damage evolution under shear stress may be a prerequisite to clarifying the mechanism for the size effect on the mechanical behavior of a sheared fracture.

1.2 Literature review

1.2.1 Aperture characterization of a rock fracture

A rock fracture consists of two rough surfaces, which are usually in contact with each other under stresses. The fracture void geometry, defined as the volume between the two rock surfaces, is strongly related to several properties of rock fractures, such as roughness, contact area, matedness and spatial correlation. The void geometry is

described by using an aperture of a rock fracture and the roughness is a measure for the shape of the rock surface. By assuming that the two fracture surfaces are nominally parallel in a reference *x*-y plane, the aperture, e_{ij}, is defined as the separation between the surfaces in the *z*-direction at each point. However, the aperture distribution of a rock fracture is affected by the states of rock stress and fluid pressure.

The aperture in a fracture can be characterized by the probability density function (PDF) and the power spectral density (PSD), similar to the surface heights, and the SD of the aperture (σ_e) provides the degree of scatter in the aperture distribution, as given by

$$\sigma_e = \sqrt{\frac{\sum\sum (e_{ij} - \bar{e})^2}{N}}, \tag{1.1}$$

where $\bar{e}$ is the mean value of the initial aperture and *N* is the number of the aperture data.

Several different techniques have been proposed to measure fracture aperture. However, measurement methods can be grouped with regard to the basic measurement procedure as shown in Fig. 1.2 (a, b and c):

a) Surface topographical measurement of the two fracture surfaces forming a void space to define the aperture as the space between the surfaces. In the literature, the topography was measured by both a mechanical device and a laser beam profilometer [4, 21].
b) Injection of wood's metal [22], resin [1], epoxy [23] or cement grout [3] into a fracture to fill up the void space. The specimen containing a fracture can then be cut into slices and the aperture can be measured by the resin thickness along the fracture on each slice by photo-microscope and image analysis techniques.
c) Casting by making a silicon-rubber replica of the void space between the fracture surfaces of a fracture, or to make a replica of the fracture surfaces [2, 24-27]. Since the specimen is not broken, this approach can be applied for the same specimen several times.

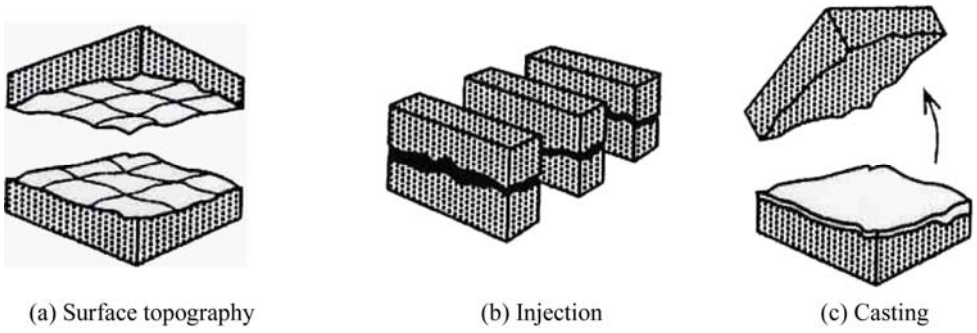

Fig. 1.2. Different methods to measure fracture aperture (Hakami, 1995).

In the group a), the surface heights of both sides of the fracture are summed to generate a "composite topography" (which is used in this work to estimate the initial aperture value). Generally, when the heights of the surfaces on the opposing walls of the fracture are $z_1(x,y)$ and $z_2(x,y)$, the composite topography is defined as (Fig 1.3):

$$z(x,y) = z_1(x,y) + z_2(x,y). \quad (1.2)$$

Thus, the aperture (e) is given by $e = d\text{-}z$, where d is the distance between two reference planes. In this work, topographical measurement of the fracture surfaces were carried out by means of a laser profilometer scanning system.

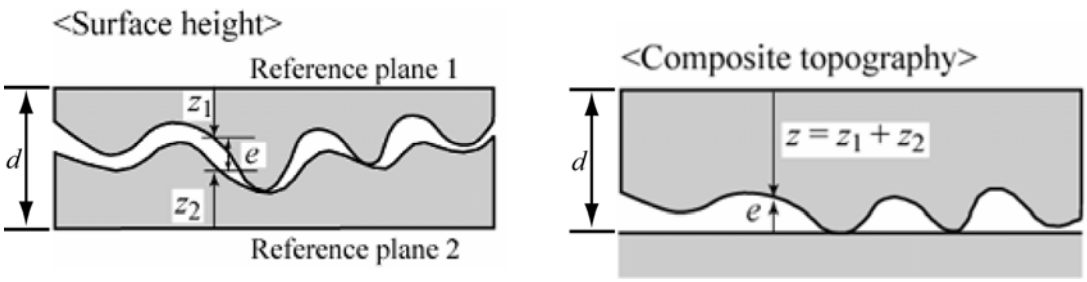

Fig. 1.3. Composite topography of a fracture.

1.2.2 Direct shear test for rock fractures

Shear failure of rock mass most often occurs in the field. Moreover, the mechanical and hydraulic behaviors of a rock mass are greatly controlled by discontinuities, such as fractures, faults and bedding. Therefore, the determination of the shear strength of both intact and jointed rocks has been the subject of innumerable investigations conducted

both in the laboratory and in situ. Accordingly, several types of laboratory apparatus have been developed to determine and understand the shear behavior of a rock mass/joint.

Several experimental methods are available for measuring the shear strength properties of fractured rock, such as the biaxial loading test [28], the triaxial compression test [29-33] and the direct shear test (DST). Among them, the DST can directly reveal the relations between stresses and displacements that are necessary to characterize the deformability and strength properties of a fracture, such as the peak shear strength, the residual shear strength and the angle of friction. Moreover, the DST provides a practical way to investigate the hydro-mechanical behavior of fractured rock. As a consequence, the DST is most commonly used in the laboratory in geotechnical engineering (sands/rocks) [34-37].

For the last two decades, researchers have been involved in modifying the design of DST apparatus to be used for a wide range of application. Thus, there is continued interest in the development of shear apparatus [33, 38-51]. The different types of DST apparatuses developed so far with the basic mechanisms/principles are shown in Fig. 1.4 to Fig. 1.7.

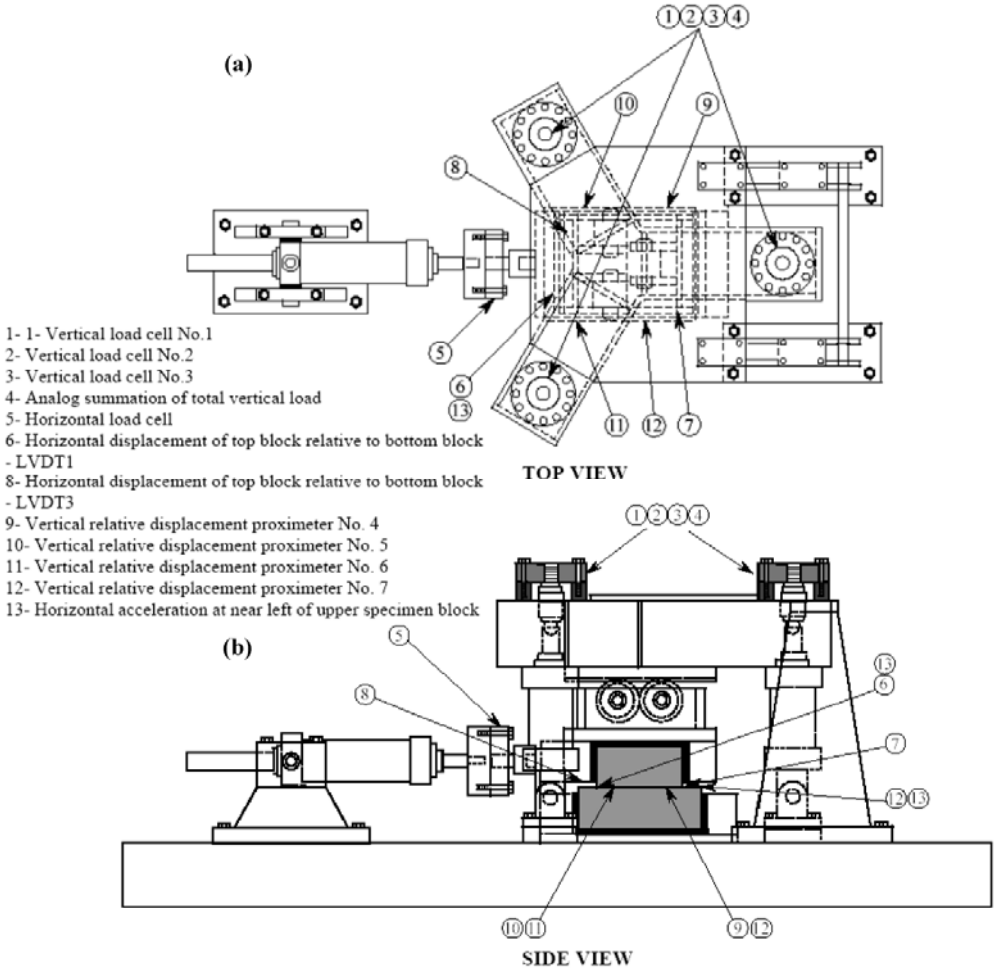

Fig. 1.4. The direct shear test apparatus developed by Ahola et al. (1996) ((a) top view and (b) side view).

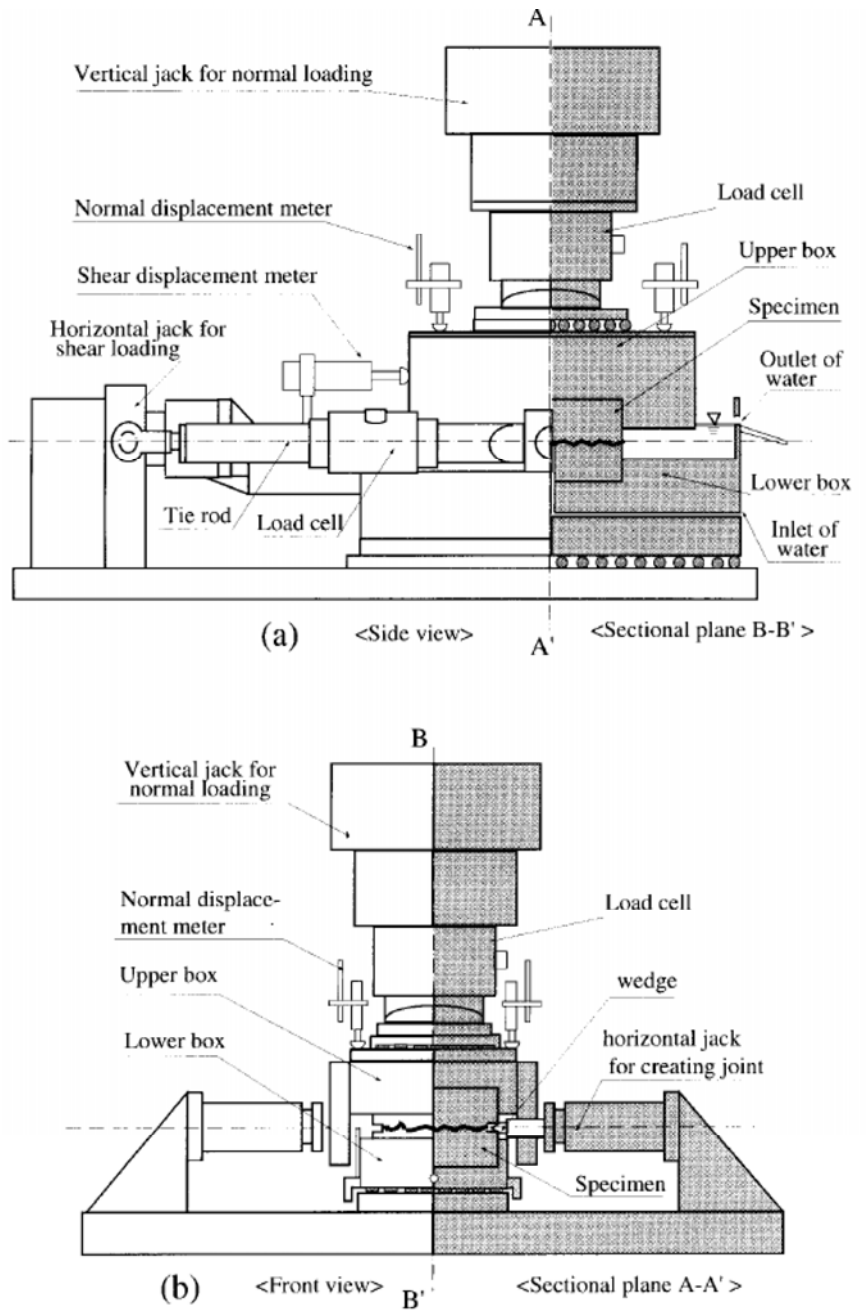

Fig. 1.5. A schematic diagrams of direct shear test apparatus developed by Esaki et al. (1999) ((a) side view and (b) front view).

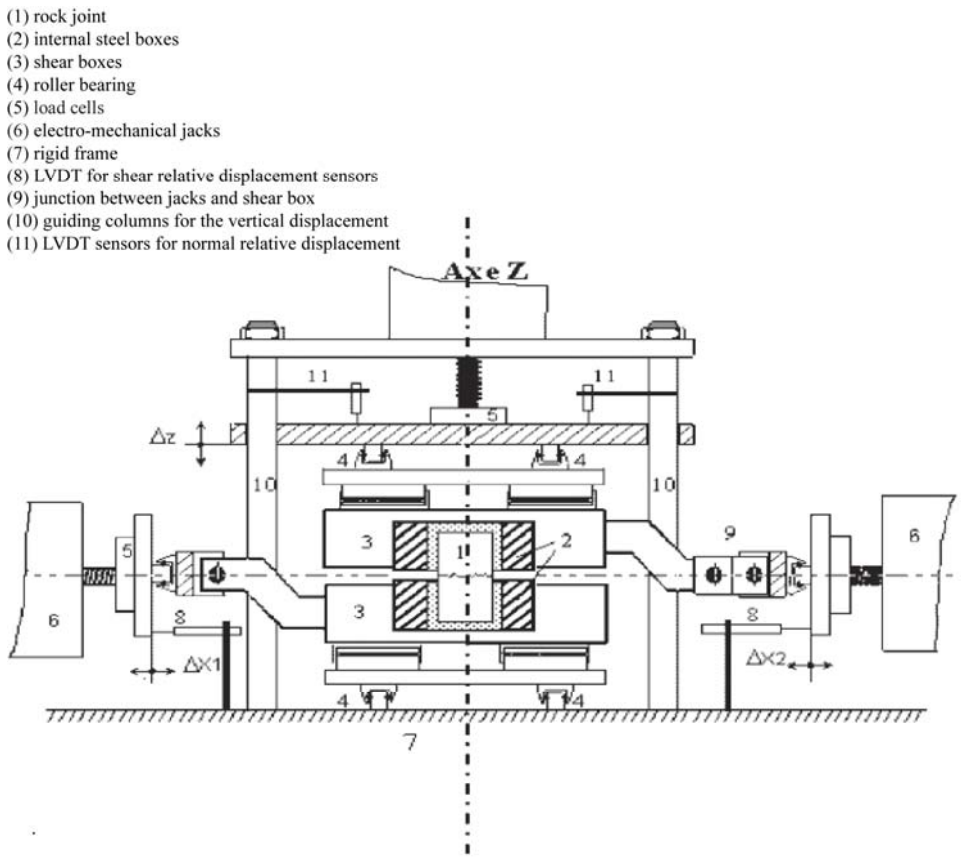

Fig. 1.6. Schematic cross section along one shearing axis of the experimental device BCR-3D developed by Hans and Boulon (2003).

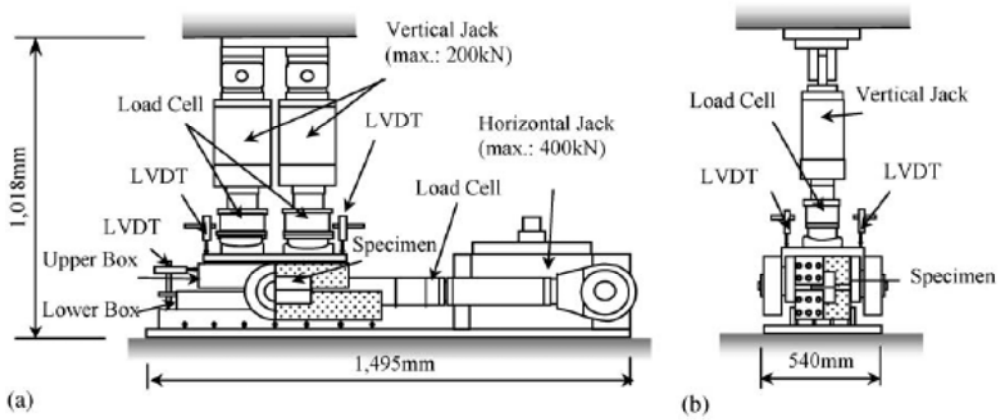

Fig. 1.7. A schematic diagrams of digital-controlled direct shear apparatus developed by Jiang et al. (2004) ((a) side view and (b) front view).

In principle, the DST is performed for a rock specimen that is placed between a fixed and a moveable shear box. After a normal load (*N*) is applied to the upper/lower shear box, a steadily increasing horizontal (shear) load is applied (*T*) to the other half. When a shear load (*T*) is applied to a specimen, a moment around the axis perpendicular to both the shear and normal loads is introduced and, accordingly, the points at which the resultant normal loads act move from the center of the loading surfaces to counter the moment produced by the shear loads, which may disturb the stress distribution and deformation in the fracture. Therefore, there is a need to understand the states of both the stress and deformation in DST for a fractured specimen and to examine the validity of the DST before shear tests are performed.

1.2.3 Typical shear behavior of a single rock fracture

The shearing of a fractured rock occur *in situ* under two boundary conditions. First, as for a rock slope where the free dilatancy of the fracture causes a lifting of the sliding block, the gravity causes a constant normal stress on the sliding surfaces. This condition is simulated in the laboratory by keeping the normal force constant under the shearing process, defined as Constant Normal Load (CNL). Second, a constrained block in a rock mass, joints in a pillar between two caverns or a joint in a reservoir exposed for high water pressure cannot slide freely. This shearing will be hindered by activation of additional normal force due to the stiffness of the surrounding rock. The condition can be simulated in the laboratory by using spring stiffness across the joint plane, defined as Constant Normal Stiffness (CNS). Fig. 1.8(a & b) shows the basic concepts of the constant normal loading (CNL) and constant normal stiffness (CNS) conditions for rock fracture testing, respectively.

In the simplest case, the shear strength (τ_p) of a single rock fracture can be described by the following equation:

$$\tau_p = \sigma_n \times \tan \phi_f \qquad (1.3)$$

where ϕ_f is the friction angle and σ_n is the normal stress.

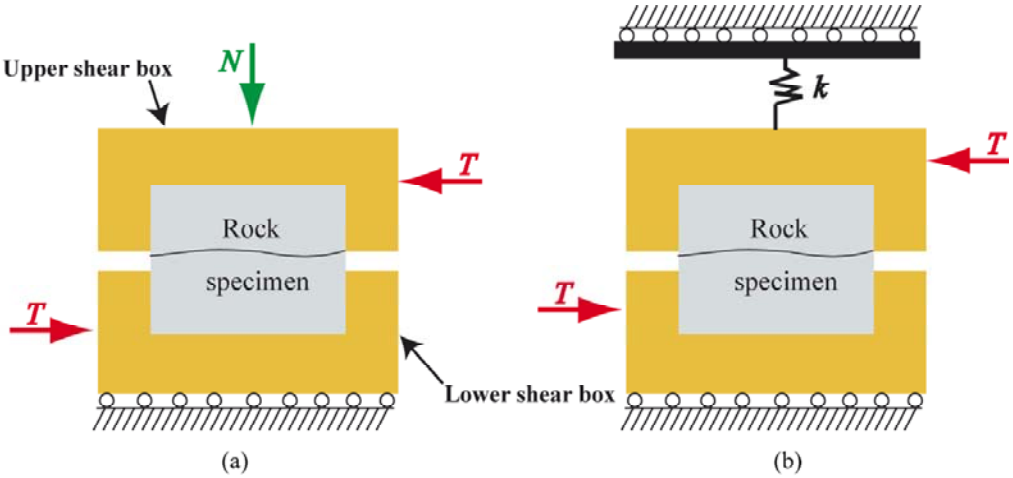

Fig. 1.8. Direct shear tests concept under (a) CNL condition and (b) CNS condition.

A typical shear stress development at a CNL condition is a quick rise to a maximum values (τ_p), followed by a gradual decline to a residual value (τ_r), as shown in Fig 1.9. The corresponding normal displacement versus shear displacement is also shown in the figure. During a short initial shearing the normal displacement is in a state of slight contraction, which is followed by dilation. The maximum normal displacement does not occur at the maximum shear stress, but instead when the shear stress attains a residual value. A parameter for a quantitative description of the volume change is the dilation angle (ϕ_d) proposed by Barton [52]:

$$\phi_d = \arctan\left(d\delta_n / d\delta_s\right) \tag{1.4}$$

where δ_n and δ_s are the normal and shear displacements, respectively. Thus, the dilation angle decreases with shear displacement, which was considered to be caused by the damage evaluation in asperities during shear.

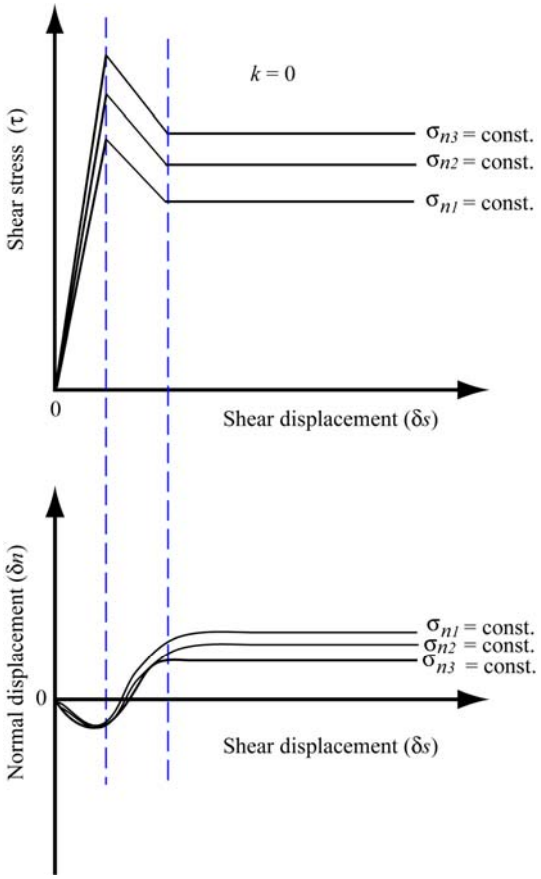

Fig. 1.9. Conceptual behavior of rock joints during shear under constant normal load (Stephansson & Jing, 1995).

Goodman [53] also proposed an idealized model to describe the characteristics of joint shear behavior under the CNL condition (Fig 1.10). For a constant level of normal stress, three modes of behavior occur.

1) A linear elastic part characterized by a rapid increase in the shear stress, until the peak strength of the joint is reached. This constant slope is called the shear stiffness (k_s).
2) A decrease from the peak to the residual shear strength.
3) A constant residual shear stress during continued displacement.

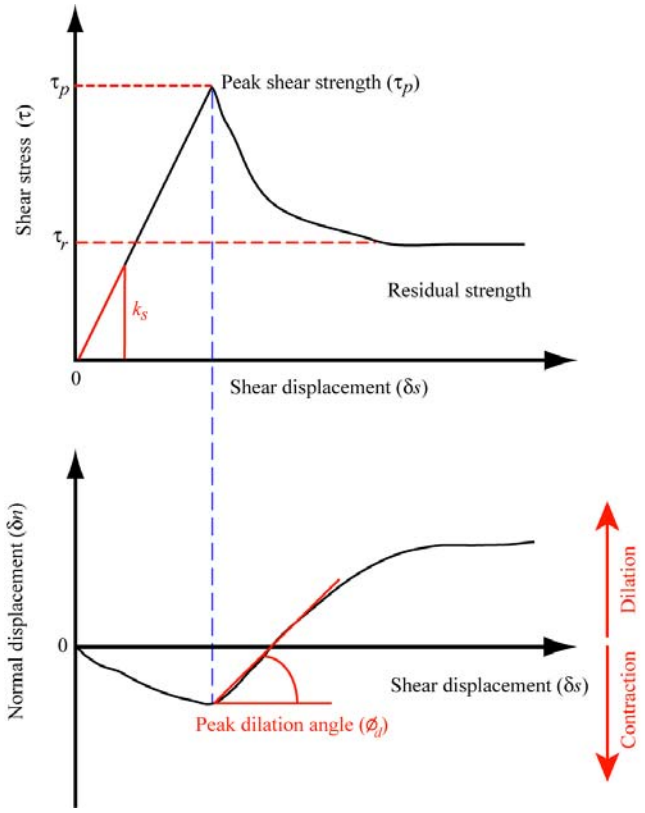

Fig. 1.10. Idealized shear stress-displacement curve at CNL (Goodman, 1980).

A typical shear behavior under CNS tests manifests a quick rise of the shear stress. This is followed by a slower decrease of the shear stress, until a constant value is obtained after a large shear displacement. Moreover, Goodman [53] showed that the non-correlated fracture shows larger non-linearity in the closure curve. It should be noted that the normal displacement during the shearing with constant normal stiffness (CNS) is smaller than under CNL, which affects fluid flow through the fracture.

1.2.4 Effect of surface roughness on shear behavior of a fracture

Since the surface roughness of a fracture has a fundamental influence on the mechanical behavior as well as fluid flow through the fracture, a large number of researcher have attempted to characterize surface roughness, to develop systems to quantify roughness, and to relate the roughness to the hydromechanical behavior of the rock fractures [6, 11, 50, 54-86]. The surfaces of a fracture may be simplified as nominally planar planes at the macroscopic level, but they may become wavy at larger scales with varying wavelengths and amplitudes. Thus, at the microscopic level, there exist numerous small-scale asperities on these surfaces. Accordingly, the presence of these asperities is the reason for the roughness of the fracture surfaces. Generally

speaking, tensile fractures have the roughest surfaces while the surfaces of the sheared fractures or planar cleavages have the smoothest ones [87].

Bandis et al. [6] investigated the effect of surface roughness on peak shear strength by performing direct shear tests on identical replicas that were cast from rubber mold of four natural joint samples with noticeable different surface roughness. Their results showed that the peak shear strength increases with surface roughness since larger shear stress was needed to break larger asperities (Fig. 1.11). In their study, the surface roughness was measured by the JRC (joint roughness coefficient) values.

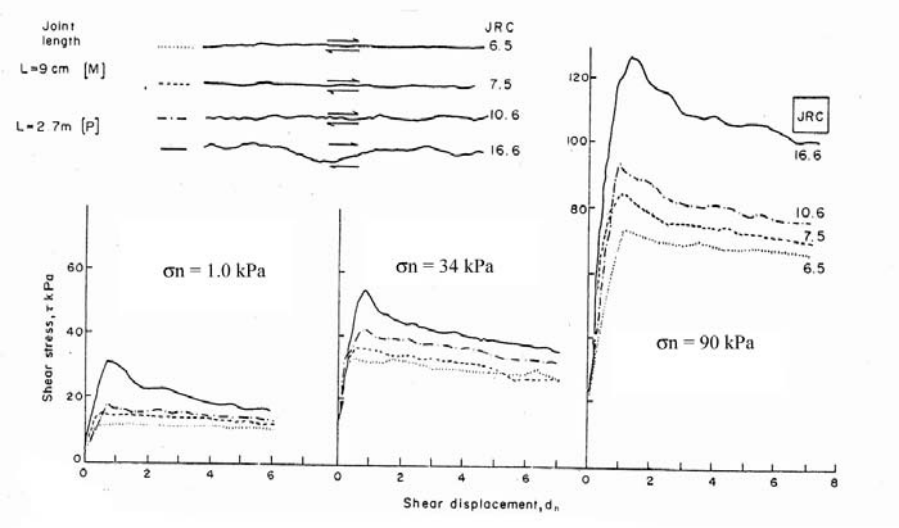

Fig. 1.11. shear stress versus shear displacement curves of replica fractures with different roughness under three levels of normal stress (Bandis et al., 1981).

Bandis et al. [6] also investigated the effect of surface roughness on dilation and dilation angle by performing direct shear tests on identical replicas that were cast from rubber mold of four natural joint samples with noticeable different surface roughness. The results showed that both dilation and dilation angle increases with surface roughness since the asperity height and accordingly the slope of the asperity increase with the surface roughness (Fig. 1.12).

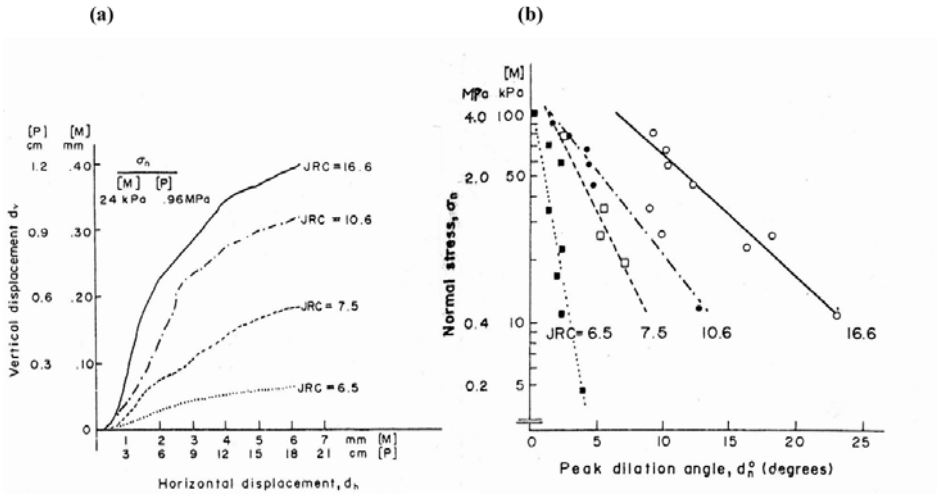

Fig. 1.12. Effect of surface roughness on (a) the dilation and (b) the peak dilation angle (Bandis et al., 1981).

Direct shear and compression tests on single fractures with different surface roughness were carried out by Yoshinaka and Yamabe [10], to investigate the effect of the roughness on the normal and initial shear stiffnesses. The results showed that both normal (k_n) and shear (k_s) stiffnesses significantly decrease with surface roughness as shown in Fig. 1.13.

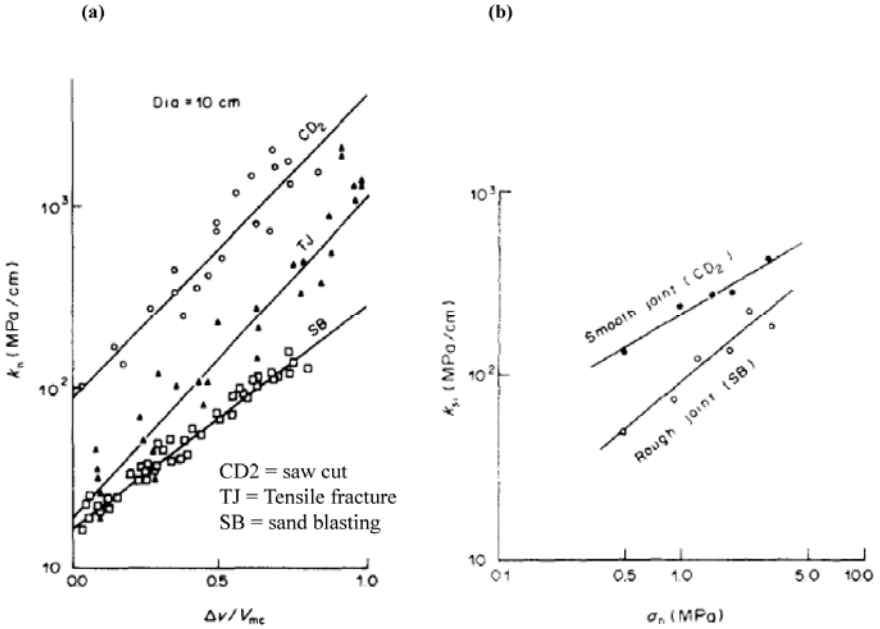

Fig. 1.13. Effect of surface roughness of three kinds of fractures: CD_2, SB and TJ on (a) normal stiffness and (b) initial shear stiffness (Yoshinaka and Yamabe, 1986).

1.2.5 Size effect on shear behavior of a fracture

Let me start this review by summarizing the previous laboratory/numerical studies of size effect on the mechanical behavior/properties of rock fractures, in [8, 11, 13, 17, 19, 20, 88-109].

Bandis et al. [6] have carefully investigated the size effect on shear behaviors of natural joint replicas as shown in Fig 1.14. The results showed that an increase in fracture size leads to:

1) a gradual increase in the peak shear displacement,
2) an apparent transition from a brittle to plastic mode of shear failure,
3) a decrease of the peak dilation angle and,
4) the size effect is smaller for smoother surfaces.

In contradiction to the above mentioned, Hencher et al. [110] concluded that there was no scale effect on shear behavior of natural joint replicas.

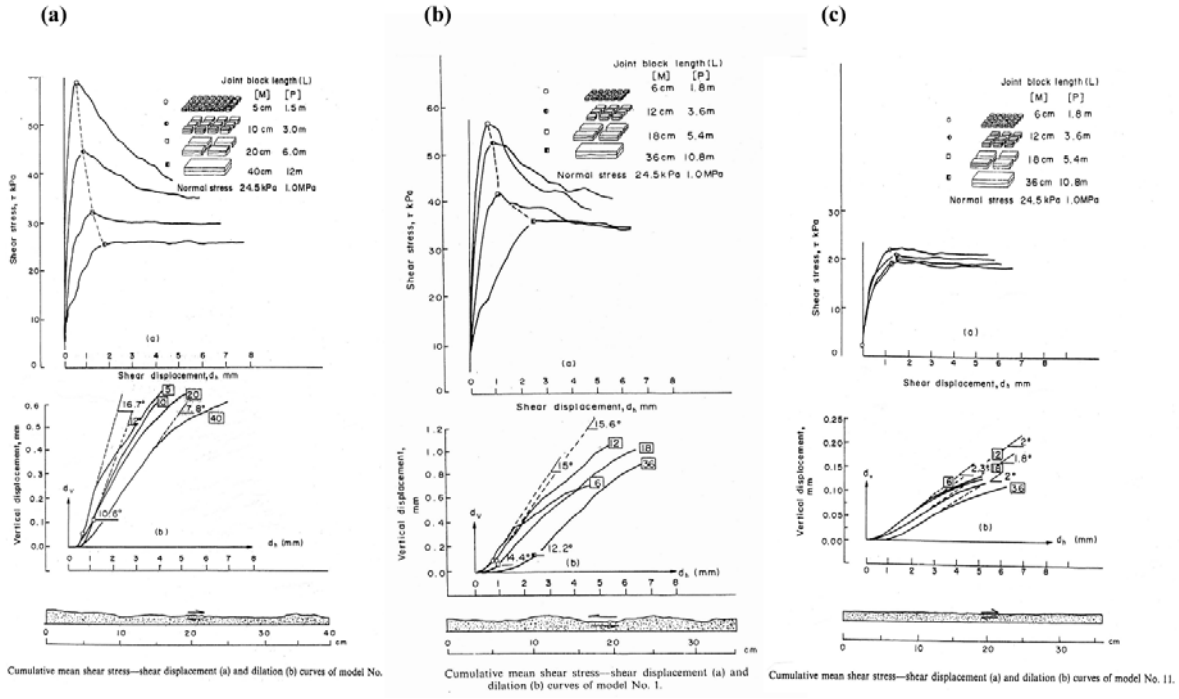

Fig. 1.14. Size effect on shear behavior and dilation angle for (a) rough surfaces, (b) moderately rough surfaces and (c) smooth surfaces (Bandis et al., 1981).

Matsuki et al. [111] showed that both the SD of the initial aperture and the mean aperture increase with shear displacement, which was obtained for the two dimensional height distributions of a hydraulic fracture that was created in granite. Sakaguchi et al. [18] studied the effect of size on the statistical characteristics of the surface heights and aperture distribution of a large-scale (about 1 m) tensile fracture. The results showed that the standard deviation of the initial aperture increases with fracture size until the fracture size is about 200 mm, beyond which the standard deviation is almost independent of the fracture size, while the mean initial aperture increases even when the fracture size exceeds 200 mm, as shown in Fig. 1.15.

Recently, Matsuki et al. showed numerically the size effect on the aperture and permeability of a large synthetic fracture of up to 12.8 m × 12.8 m [17]. They reported that the SD of the aperture of a sheared fracture increases with fracture size when shear displacement is greater than a certain percentage of the fracture size, since the matedness of the fracture decreases with fracture size. Fardin [11] showed that both the mean and SD of the aperture increase with the fracture size and shear displacement.

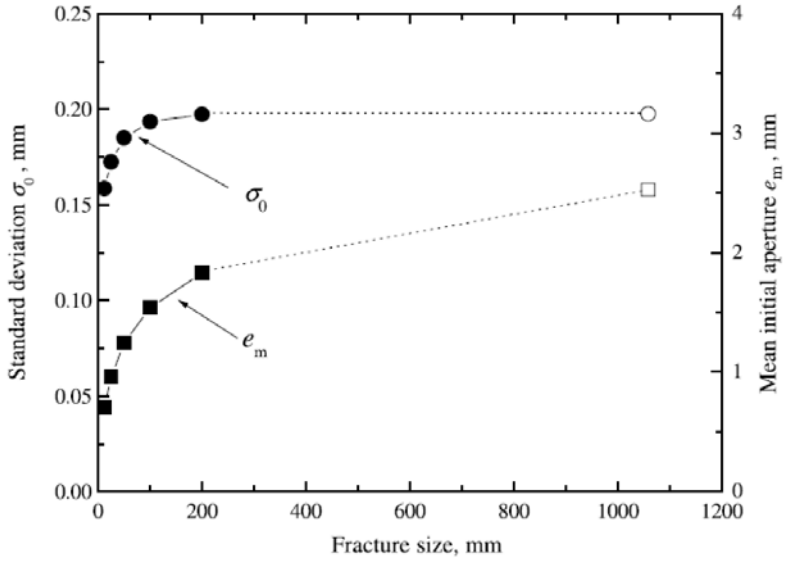

Fig. 1.15. Relation between fracture size and the standard deviation of the initial aperture and the mean initial aperture for square fractures (Sakaguchi et al., 2006).

Bandis et al. [6] showed the size effect on the peak shear strength by performing direct shear tests for natural joint replicas. The results showed that the peak shear strength decreases with fracture size to approach an asymptote (Fig. 1.16). Fardin [11] and Fardin et al. [112] also showed that the peak shear strength of concrete fracture

replicas decreases as fracture size increases for all the applied normal stresses.

The fracture size effects on both normal (k_n) and shear (k_s) stiffnesses was investigated by Yoshinaka and Yamabe [10] in the direct shear and compression tests on single fractures. The results showed that both normal (k_n) and shear (k_s) stiffnesses significantly decrease as fracture size increases, as shown in Fig. 1.17. Recently, Fardin [11] and Fardin et al. [112] studied the size effect of concrete fracture replicas on both k_n and k_s and obtained the same results as those obtained by Yoshinaka and Yamabe [10].

Xie et al. [75] experimentally clarified the size effect on the fractal characteristics of rough fracture surfaces. Their results showed that the fractal dimension (D) inverses with an increase in sample length and its follows an exponential law. Fardin [11] and Fardin et al. [113] plotted the calculated fractal dimension (D) of the fracture surface with their size. The results showed that the fractal dimension is scale-dependent and decreases with fracture size, until the size reaches a stationarity threshold which was about 500 mm.

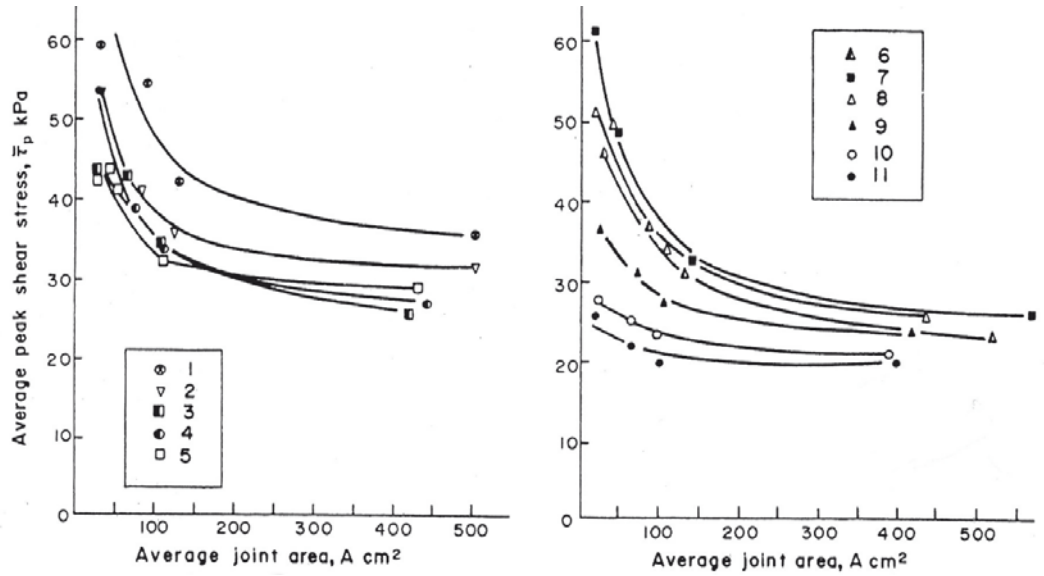

Fig. 1.16. Size effect on variation of average peak shear strength (Bandis et al., 1981).

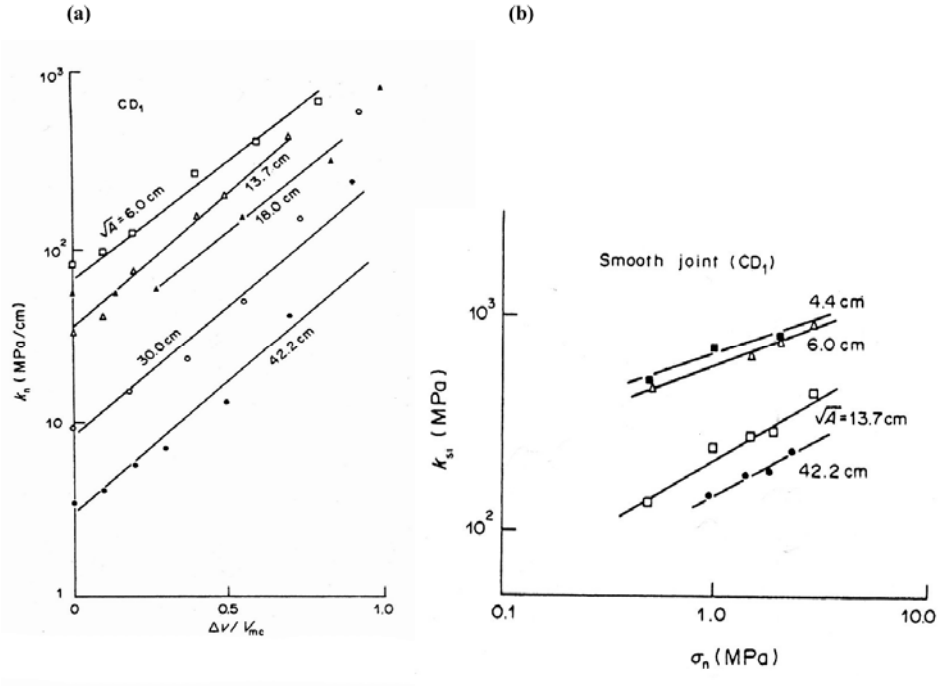

Fig. 1.17. Size effect on (a) normal stiffness and (b) initial shear stiffness (Yoshinaka and Yamabe, 1986).

Thus, size effect certainly exists in the topography, the aperture and the mechanical behavior of a fracture, and most of the experiments on the scale effect have been performed in the direct shear tests of a rock fracture under constant normal stress. However, the properties were obtained in the laboratory tests on samples of limited sizes, within 400 mm. These sizes may or may not be large enough to reach the threshold of the fracture samples. There is an acute lack of understanding of the hydromechanical behavior of large fractures (such as fault or fracture zones) with lengths from tens of meters to kilometers in scale and large widths (say, 10 mm- 50 m). This type of rock fractures has been associated with problems in many engineering projects, radioactive waste repositories, geothermal and hydrocarbon reservoirs and other large-scale facilities in rocks with potentially significant impacts on the rock structure performance and the environment.

1.3 Scope and objective

It is well known that the mechanical behavior (shear behavior) of a single rock fracture under both normal and shear stresses are scale-dependent, but only a few studies have been carried out to investigate the effect of fracture size on the mechanical

behavior, mainly due to technological limitations as well as experimental difficulties. Moreover, the surface topography of the fracture during shear has not been measured in these studies, and consequently, the mechanism for the size effect has not yet clearly well understood. Understanding of the damage evolution under shear stress may be a prerequisite to clarifying the mechanism for the size effect on the mechanical behavior of a sheared fracture.

Thus, the main objectives of this thesis are:

- to examine the validity of the DST for a rock fracture by analyzing the traction distributions on the loading surfaces and both the stress and deformation in a fracture,
- to clarify the effect of the specimen height on the stress and deformation in the fracture during shearing and then to find the optimum specimen configuration that reduces non-uniformity of the stress distribution,
- to clarify the size effect on the shear behavior and the non-linearity of the closure curve of a fracture during shear,
- to clarify the effect of shear displacement, normal stress and gouge material on the shear behavior, non-linearity of the closure curve as well as normal stiffness,
- to understand and determine the evolution of surfaces damage during shearing as a function of both fracture size and normal stress and,
- to understand the mechanism of size effect on the shear behavior of a fracture.

To reach the above goals, analytical and experimental investigations were performed in this study. First, a 3D FEM analysis with quadratic joint elements as a fracture model was performed to examine the validity of the DST for a rock fracture by analyzing both the stress and deformation in fractured specimens of various sizes for a limited case of a set of normal and shear stresses (σ_n = 10 MPa and τ = 7 MPa). According to the simulation result, the practical specimen height was determined for the standard height to be used throughout this work. Then, a direct shear test apparatus including measuring devices, reference plates and matching bars were designed and developed.

Second, in order to study the effect of size and shear displacement on the shear behavior of a single facture, a tensile fracture was created in a large block of granite with a size of 385× 385 × 200 mm, which was cut into three different sizes of 100 mm × 100 mm, 150 mm × 150 mm and 200 mm × 200 mm, and direct shear tests were performed with a normal stress of 10 MPa. In this experiment, normal and shear stresses

were unloaded at designated shear displacements and the change in the surface topography was measured by using a non-contact surface profile measurement system with a laser profilometer, to determine the evolution of surface damage and aperture during shear.

Finally, to clarify the effect of normal stress and gouge material on the shear behavior of a fracture, a tensile fracture in granite were reproduced by using mortar replicas of different sizes, and the fracture replicas were tested in the direct shear test under two different values of normal stress (0.3 and 1 MPa) and shear displacements of 2 and 20 mm with and without cleaning the gouge materials that were produced during shear.

1.4 Thesis structure

Following this chapter, the method and the results of the numerical simulation on the effects of non-uniform traction and specimen height in the direct shear test on the stress and deformation in a fracture are described in chapter 2. In chapter 3, described the development of the DST apparatus including a data acquisition system using laser profilometer devices, shear deformation and closure measurement devices. The methodology in the experimental work of this study is also described in this chapter. In chapter 4, after physical and mechanical properties of the specimen are described, the experimental results of the effects of size and shear displacement on the shear deformation of the fracture samples are presented and discussed. The effect of normal stress and gouge materials on the shear behavior of the mortar replicas is presented and discussed in Chapter 5. These Chapters are followed by conclusions Chapter 6.

2. FINITE ELEMENT ANALYSIS OF STRESS AND DEFORMATION IN A FRACTURE IN THE DIRECT SHEAR TEST

2.1 Statement of the problem

Many experimental/numerical studies have focused on the behavior of soil and sand in a shear box [114-118]. These studies have shown that the stress distribution in the specimen is strongly non-uniform and that the shape of the specimen affects the stress distribution. However, the boundary conditions given by the shear box used for granular materials differ from those for rock, and accordingly the stress and deformation in a rock specimen are different from those in soil/sand.

Fig. 2.1 shows a schematic of a typical DST apparatus for a rock fracture. In the DST, a rock specimen is installed in a rigid shear box consisting of upper and lower parts. Under the condition of constant normal stress, after a constant normal load (N) is applied to the top surface of the upper shear box, a steadily increasing horizontal (shear) displacement is applied to the lower shear box, while the shear force (T) required for horizontal displacement is measured. When tilting or rotating of the upper shear box does not occur, a uniform vertical displacement (w_0) is applied to the upper surface of the specimen and a uniform horizontal displacement (u_0) is applied to the lower half of the specimen, since the upper and lower shear boxes are sufficiently rigid compared to the rock specimen. Boulon [40] pointed out that even a slight rotation (e.g. 0.1^o) of the upper half of the specimen in a shear box had a significant effect, and therefore tried to avoid any rotation of the shear box by introducing a new shear machine. Esaki et al. [43] also improved the direct shear test to diminish the effect of rotation of the shear box by aligning both the shear load (T) and the horizontal reaction from the upper shear box ($R_T = T$) exactly at the middle height of the specimen (Fig. 2.1). In this improved shear test apparatus, both the normal load (N) and its reaction ($R_N = N$) can be applied at the middle length of the upper and lower shear boxes. Thus, the shear boxes do not rotate, and uniform vertical and horizontal displacements are applied to the upper and lower halves of the specimen, respectively.

However, even for these shear boxes, the conditions for a specimen within the shear boxes are different than those for the shear boxes themselves, as schematically shown in Fig. 2.2, where the x and z axes are taken in the horizontal and vertical directions, respectively. When the shear load (T) is applied in the form of a uniform horizontal displacement (u_0) to the lower half of the specimen and a reaction ($R_T = T$) is produced

in the upper half of the specimen, a moment ($M_T = 2z_0T$) is inevitably introduced around the axis perpendicular to the vertical cross-section [119], since the shear load and the reaction are not co-axial and are separated by $2z_0$, where z_0 is the vertical distance from the middle height of the specimen at the point at which the (resultant) shear load and the (resultant) reaction act to have moments equivalent to those produced by the distributions of the traction. Note that the reaction is symmetric to the shear load with respect to the origin in the x-z plane since the problem is symmetric with respect to the origin. Furthermore, the tractions on these planes are never uniform, as will be shown later. Accordingly, the points at which the normal load (N) and its reaction ($R_N = N$) act is shifted by x_0 in the horizontal direction from the center of the upper and lower surfaces of the specimen, so that the following condition may be satisfied, to balance the moment produced by the shear load (M_T):

$$M_N = 2x_0N = 2z_0T = M_T, \tag{2.1}$$

where M_N is the moment produced by the normal load (N) and the reaction (N).

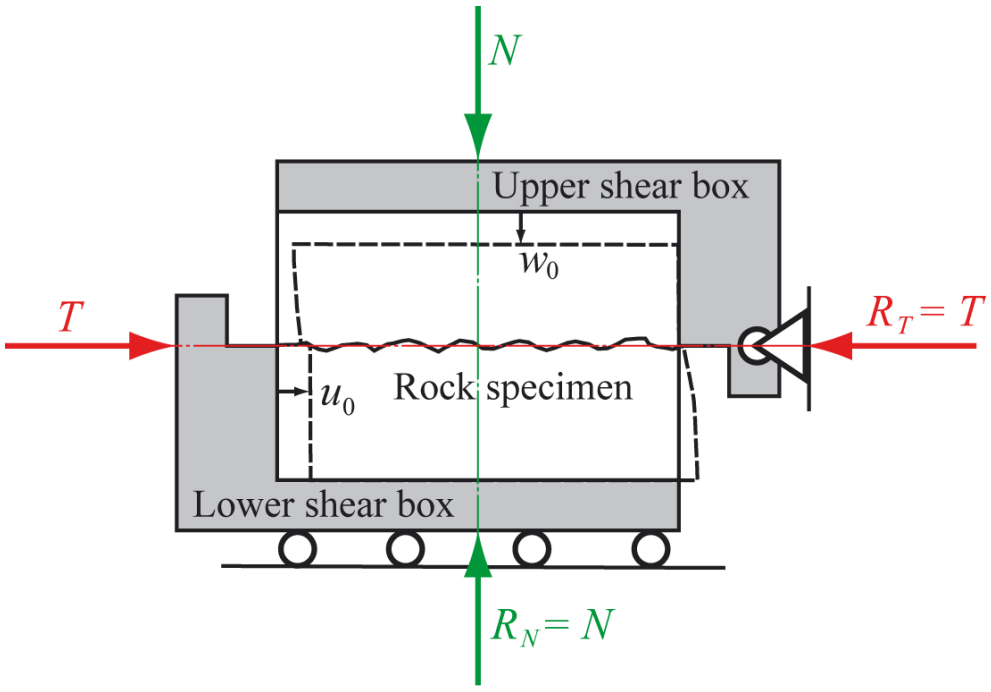

Fig. 2.1. Schematic of the direct shear test apparatus for a rock specimen with normal (N) and shear (T) loads applied to a shear box.

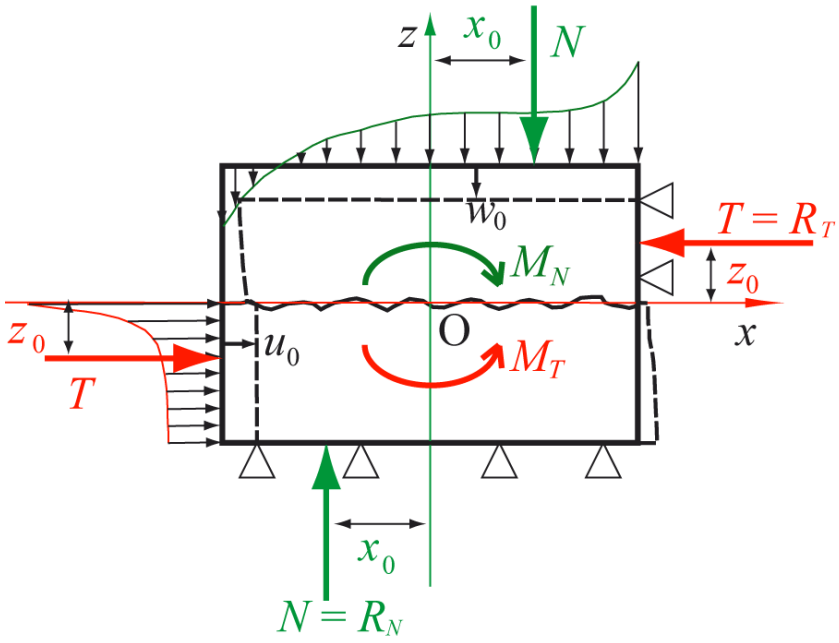

Fig. 2.2. Schematic of the distributions of traction in the direct shear test of a rock specimen with moments M_T and M_N produced by the shear (T) and normal (N) loads, respectively.

For simplicity, it was assumed throughout this chapter that the friction between the surfaces of the specimen and the shear box is negligible [43]. Thus, the tractions on the upper and lower surfaces of the specimen are never uniform unless $T = 0$ and are biased so that the traction on the upper surface increases in compression in the direction of the side surface where the horizontal reaction acts. Since the shear load (T) increases while the normal load (N) remains constant, the value of x_0 increases according to Eq. (2.1), and the tractions on the upper and lower surfaces of the specimen are more biased. This suggests that the tractions on the upper and lower surfaces of the specimen can be tensile near the other ends of the surfaces for large shear loads relative to the normal load, if the vertical displacements of the upper and lower surfaces of the specimen are uniform, as is the case in which the upper and lower surfaces of the specimen are fixed to each shear box. However, a rock specimen is usually installed in a shear box without glue. Accordingly, partial separation between the upper and lower surfaces of the specimen and the loading plates of the shear box may occur at large shear loads when the upper and lower surfaces of the specimen are not glued to the shear box.

As described above, the tractions on the loading planes of a rock specimen for both shear and normal loads are never uniform in the DST, and, furthermore, an internal moment is distributed within the specimen, due to the non-coaxial loading of the shear

force. Accordingly, these boundary conditions may disturb the stress in the fracture to produce non-uniform distributions of stress and deformation in the fracture. Thus, the limitations of the DST include non-uniform distributions of the stress and deformation in the fracture, which may affect the estimation of the hydraulic properties of the fracture, since non-uniform normal stress may cause non-uniform closure.

However, the effect of such non-uniform tractions in the DST on the stress and deformation in a rock fracture is not yet well understood, while many experimental studies have been carried out by using the DST to understand the shear behavior of a fracture and to explain the fundamental behavior of fractured rock [6, 19, 26, 33, 38, 46, 50, 59, 120]. This could be attributed to the complex behavior of a fracture and the difficulty of modeling this behavior. Schneider [119] and Kutter [121] used a 2D FEM with joint elements to analyze the stress distribution in a rock joint in the DST. Their result showed that a large concentration of stress occurs near the end edges of the joint, whereas the stresses are relatively uniform in the middle portion. However, they did not give a constitutive law for the joint.

Recently, the discrete element method (DEM) has been used in numerical simulations of the mechanical behaviors of a rock fracture in the DST [122-124]. In this method, the surface roughness of a fracture can be expressed explicitly, which makes it possible to evaluate both the local stress concentrations on the surfaces of a fracture and therefore the evolution of asperity damage in the fracture. However, the effect of non-uniform boundary conditions produced in the DST on the stress in the fracture is confused with that of the fracture topography, and thus is accordingly hidden by the heterogeneous stress distributions caused by the roughness of the fracture. Furthermore, the boundary conditions in the DEM simulation may be similar to those for granular materials and different from those for a rock specimen, since particles must be placed in the shear box. Thus, the DEM is not necessarily appropriate for examining the validity of the DST for rock.

In this work, I first sought to show the non-uniform distributions of the tractions on the loading surfaces of a rock specimen with a fracture in the DST when uniform vertical and horizontal displacements are applied to the upper and lower halves of the specimen, respectively (Fig. 2.2), and then sought to clarify the effects of both such non-uniform boundary conditions and the specimen size on the stress and deformation in the fracture. For these purposes, a 3D finite element method (FEM) with joint elements was used, in which the constitutive law of a fracture is implemented in the simulation code without explicitly giving the surface roughness of the fracture. Thus, using joint elements, I adopted a conceptional fracture with uniform mechanical

properties to extract only the effect of the non-uniform tractions at the boundary of a rock specimen on the stress and deformation of the fracture. Therefore, the real stress distribution in a fracture can be obtained by superposing the effect of the surface roughness of the fracture on the results obtained for the conceptional fracture.

In this chapter, a simulation was performed using in-house code for specimens with four different sizes in both the initial stage with a small shear displacement and the residual stage with a large shear displacement, as well as for non-fractured specimens that were used as a reference. The simulation code considers the dependence of the non-linear behavior of the closure on shear displacement, that of shear stiffness on normal stress, and partial separation caused by large shear loads between the loading plates and the upper and lower surfaces of the specimen. Since shear dilation may only give a relatively uniform offset upon the closure/opening of a fracture, depending on the topography of fracture surfaces, and since I focus only on the non-uniformity in the deformation in the fracture, I did not directly introduce the mechanism of shear dilation in this simulation, and only consider the effect of shear dilation after the results are obtained. For comparison, I performed an additional analysis for the case in which the loading plates and specimen surfaces are glued to each other and are not separated.

Since the constitutive law of a fracture depends on stress and is highly non-linear with respect to stress, both the boundary conditions of the traction in the DST and the state of stress in the fracture cannot be given by a linear combination of the effects of the applied normal and shear stresses. Furthermore, it is obvious that the parameters in the constitutive law for the fracture affect the boundary conditions of traction and the stress and deformation in the fracture. Thus, there are too many factors that affect the results to draw comprehensive conclusions. Therefore, I limited the cases for investigation to adopt only the values obtained for tensile fractures in Inada granite for the parameters in the constitutive law, and furthermore performed the simulation only for a set of normal (σ_n) and shear (τ) stresses (σ_n = 10 MPa and τ = 7 MPa) to show both the validity of the DST and the effect of the specimen height and shape for these limited cases.

2.2 Finite element method (FEM)

In recent years, numerical modeling techniques to simulate fracture process have been widely used in rock engineering with development of computational techniques and computer technology. A large number of numerical methods such as finite element method (FEM), boundary element method (BEM), discrete element method (DEM) and

displacement discontinuity method (DDM) have been used to study the mechanical behavior of fractures in rock mass. In fact, the FEM is perhaps the most widely used numerical method in science and engineering. Since its origin in the early 1960s, much of the work on FEM development has been specifically oriented toward problems in rock mechanics, as illustrated in [125-128] , since it was the first numerical method with enough flexibility to treat material heterogeneity, non-linear deformability, complex boundary conditions, in-situ stresses and gravity.

As a matter of fact, the most notable contributions were from [14, 125, 129]. Thus, the well-known 'Goodman joint element' in rock mechanics literature has been widely implemented in FEM codes and applied to many practical rock engineering problems. Also, it has been extended to consider peak and post-peak behavior in the shear direction.

2.3 Mechanical model of a specimen and fracture

2.3.1 Specimen and rock

Based on the experimental work done by Esaki et al. [43], specimens in the shape of a rectangular prism with four different sizes were used (Table 2.1). To investigate the effect of specimen height on the stress and deformation in a fractured specimen, the heights (h) in Models 1, 2 and 3 were different (0.08 m, 0.06 m and 0.04 m, respectively), while the length (l) and width (b) for these models were the same (0.1 m × 0.08 m). Model 4 (0.2 × 0.16 × 0.08), which was twice as large as Model 3 in all dimensions, was used to investigate the effect of the specimen shape. Moreover, boundary conditions in which the loading plates and the upper and lower surfaces of the specimen are fixed to each other were applied to the same dimensions in Model 3 to investigate the effect of the boundary conditions, and this was called Model 3FX. An intact specimen with no fracture was also analyzed for the same dimensions in all Models, and these were called Model 1I, Model 2I and Model 3I.

A set of normal and shear stresses was designated for both the initial and residual stages according to the experiment performed by Mitani et al. [130] for tensile fractures in Inada granite, as indicated by circles in Fig. 2.3. A normal stress of 10 MPa and a shear stress of 7 MPa were chosen for both the initial and residual stages. The shear displacement in the initial stage is small while that in the residual stage is about 7 mm. Table 2.2 shows the designated values of the normal (σ_n^*) and shear (τ^*) stresses, Young's modulus (E) and Poisson's ratio (ν) of rock, determined in uniaxial compression for Inada granite [131], and the coefficient of friction (μ) used in the

simulation for the residual stage. The coefficient of friction is 0.7 for the designated values of the normal and shear stresses, since $\tau^*/\sigma_n^* = 0.7$.

Table 2.1. Selected model dimensions.

conditions	Model no.	Dimension
		l (m) × b (m) × h (m)
Intact	Model 1I	0.1 × 0.08 × 0.08
	Model 2I	0.1 × 0.08 × 0.06
	Model 3I	0.1 × 0.08 × 0.04
Fractured	Model 1	0.1 × 0.08 × 0.08
	Model 2	0.1 × 0.08 × 0.06
	Model 3	0.1 × 0.08 × 0.04
	Model 4	0.2 × 0.16 × 0.08
Fixed	Model 3FX	0.1 × 0.08 × 0.04

Table 2.2. Designated values of normal and shear stresses, mechanical properties of rock and coefficient of friction.

σ^*_{n} (MPa)	τ^* (MPa)	E (GPa)	ν	μ
10	7	71.3	0.2	0.7

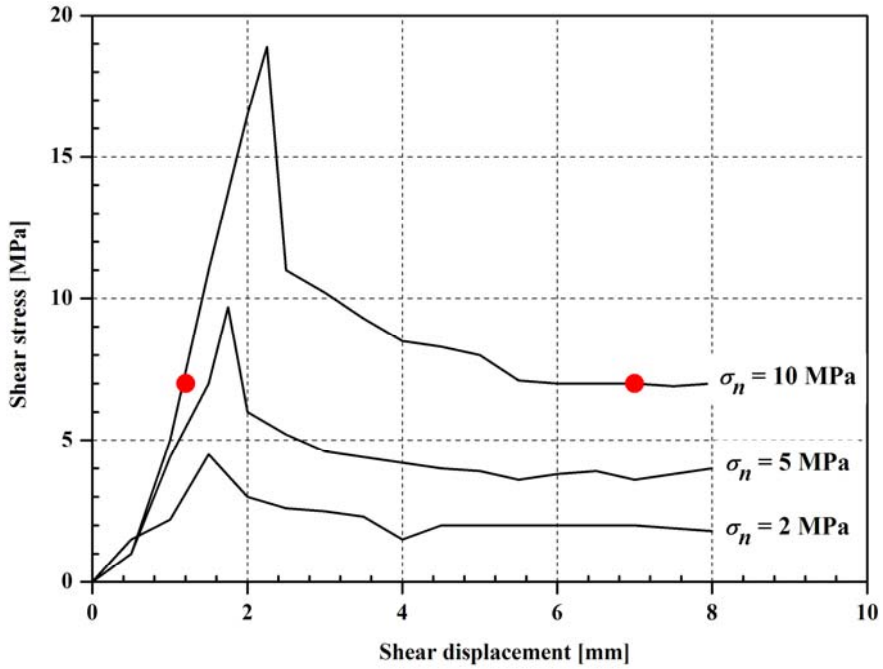

Fig. 2.3. Shear stress versus shear displacement curves for joints in Inada granite (Mitani et al., 2002).

2.3.2 Fracture

The mechanical properties of a fracture are characterized by springs with stiffnesses (k_s) and (k_n) as shown in Fig. 2.4, parallel and perpendicular to the fracture planes, respectively. These stiffnesses give the relations between normal stress (σ_n) and closure (Δu_z), and between shear stresses (τ_x) and (τ_y) in the x and y directions parallel to the fracture plane, respectively, and the relative shear displacement (Δu_x) and (Δu_y) as

$$\begin{aligned} \sigma_n &= k_n \Delta u_z, \\ \tau_x &= k_s \Delta u_x, \\ \tau_y &= k_s \Delta u_y. \end{aligned} \tag{2.2}$$

When sliding at all points of a fracture is considered in the residual stage, the following Coulomb's (Amontons') condition was used

$$\tau = \mu |\sigma_n| . \tag{2.3}$$

Thus, the shear stiffness changes in the residual stage to satisfy the above equation.

When shear displacement is small (initial stage), the following exponential formula was assumed for the normal stress (σ_n) versus closure (Δu_z) curve [132]:

$$\sigma_n = Ae^{B\Delta u_z}, \tag{2.4}$$

where A and B are constants that depend on the fracture and the rock. Accordingly, the normal stiffness (k_n) is given by

$$k_n = \frac{B\sigma_n}{\ln(\sigma_n / A)}. \tag{2.5}$$

I also assumed a linear relation between shear stiffness and the normal stress for the initial stage [130]

$$k_s = C + D\sigma_n, \tag{2.6}$$

where C and D are constants that depend on the rock and the fracture.

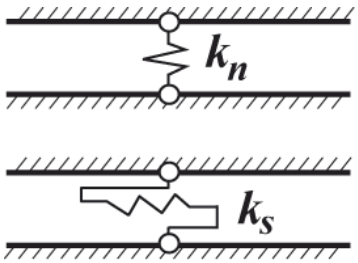

Fig. 2.4. Normal (k_n) and shear (k_s) stiffnesses of a joint element.

It is well known that the non-linear closure behavior of a fracture depends on the matedness of the fracture [14]. Recently, it was shown that the non-linearity in the closure of a fracture is governed by the SD of the aperture [13, 133], which provides a measure for the matedness of the fracture. Accordingly, when shear displacement is large (residual stage), the relation between normal stress (σ_n) and closure (Δu_z) may change according to the shear displacement, since the matedness of the fracture decreases with the shear displacement [17], resulting in an increase in non-linearity. It

was assumed that the normal stress (σ_n) depends on the closure that is normalized by the SD of the initial aperture (s_a), according to Matsuki et al. [133] and Giwelli et al. [13]. Thus, the following relation between the normal stress and closure was assumed for the residual stage:

$$\sigma_n = A\exp(B'\frac{\Delta u_z}{s_a}), \tag{2.7}$$

where B' is given by

$$B' = s_{a0}B, \tag{2.8}$$

where s_{a0} is the SD of the initial aperture when the shear displacement is zero (Eq. 2.4).

For synthetic fractures that are created based on data for a tensile fracture of 1 m in Inada granite [18], the value of s_a is given as a function of the shear displacement (δ) [17]:

$$s_a = C_0 + C_1\delta + C_2\delta^2, \tag{2.9}$$

where C_0, C_1 and C_2 are constants that depend on the fracture and the rock. Thus, the normal stiffness in the residual stage is given by

$$k_n = \frac{B'\sigma_n}{s_a \ln(\sigma_n / A)}. \tag{2.10}$$

The constants in Eqs. (2.4) to (2.10) used in this chapter were all determined from data for tensile fractures in Inada granite and are summarized in Table 2.3. The values of A and B were determined according to Matsuki et al. [17]. The values of C and D were determined according to Mitani et al. [130], and the values of B', C_0, C_1 and C_2 were determined for a synthetic fracture with a size of 0.1 m [17]. The SD of the surface height in tensile fractures in Inada granite is about 1.2 mm for a length of 0.1 m [18].

Table 2.3. Values of the parameters used in this study.

Initial stage				Residual stage			
A (MPa)	B (m^{-1})	C (MPa/m)	D (m^{-1})	B' (-)	C_0 (m)	C_1 (-)	C_2 (m^{-2})
0.0192	57.0×10^{3}	2004	595	9.7584	0.2011×10^{-3}	0.10352	-0.79878

2.4 Method of FEM

2.4.1 FEM model

Since sliding of the fracture was introduced for the residual stage, the Goodman joint element as a mechanical model of a fracture was used [14], as described previously. The joint element was originally proposed as a constant strain element. However, since a quadratic element with 20 nodes (rectangular prism) was used for a normal solid element (Fig. 2.5a), I used quadratic joint elements to be consistent with solid elements [134]. The thickness of the joint element is zero, and this element has 16 nodes overall (Fig. 2.5b). Interpolation functions were used both to transform global coordinates to the local coordinates of an element and to interpolate physical quantities such as displacement, traction and stiffnesses at an arbitrary point on the plane of the element from those at the nodes (isoparametric transformation) [125]. Note that the use of the joint element does not mean that the fracture has flat surfaces since the effect of the rough surfaces is reflected by the parameters in the constitutive law, although only the macroscopic (mean) behavior of the fracture is considered.

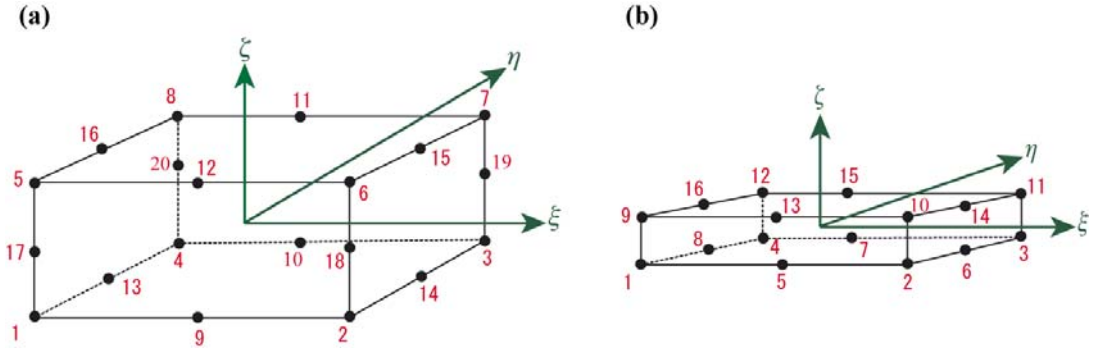

Fig. 2.5. Quadratic joint element with (a) 20 nodes for a solid, and (b) 16 nodes for a fracture.

Fig. 2.6 shows a mesh diagram for Models 1, 2, 3 and 3FX, with the coordinates (x, y, z) used in this study. Since all specimens are symmetrical with respect to the xz plane, half of the specimen was modeled and there are joint elements (a fracture) at the middle of the height. For the intact specimen (Table 2.1), the model was divided into finer meshes than shown in Fig. 2.6, since the stress concentration was much greater than that in the specimen with a fracture, although the mesh diagram was not shown.

When a large shear displacement occurs in the residual stage, the nominal fracture area that is in contact decreases due to the offset, as shown in Fig. 2.7. However, the parts that are free from stress (A in Fig. 2.7) may not significantly contribute to the deformation and stress in the fracture . Therefore, I ignored these parts in the simulation for the residual stage, and used the same specimen as with a small shear displacement (Fig. 2.6).

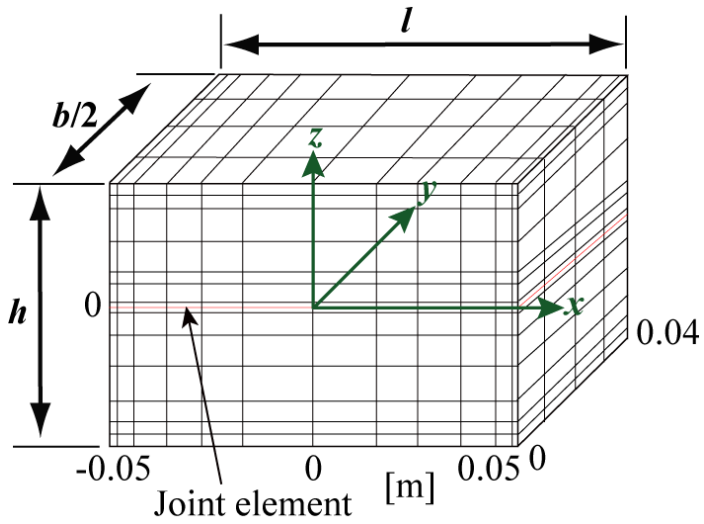

Fig. 2.6. Mesh diagram of the half-specimen used in the FEM calculation.

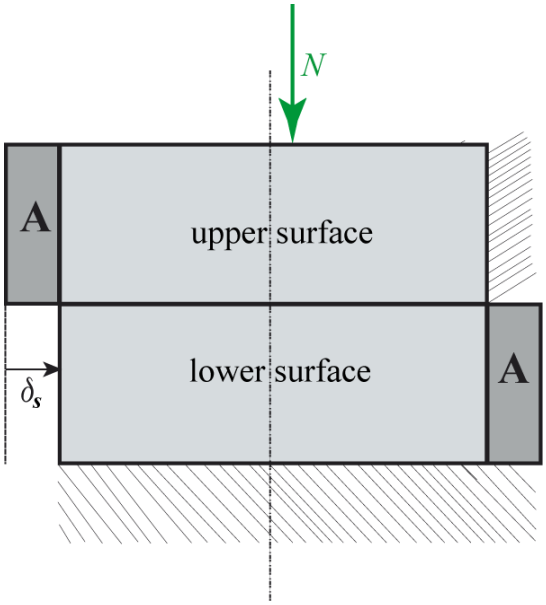

Fig. 2.7. Offset produced by shear displacement.

2.4.2 Boundary conditions

Fig. 2.8 shows a schematic illustration to explain the boundary condition used in this study. The symbols ZU, YC, etc. indicate each plane and those in parentheses [(ZL), (YU), etc.] indicate the planes behind the specimen. In the *z* direction, a uniform displacement (w_0) was applied to the upper surface (ZU), while the lower surface (ZL) was fixed except for the nodes at which separation occurs. In the *x* direction, a uniform displacement (u_0) was applied to the lower half of the left end surface (XLL), while there was zero displacement for the upper half of the right end surface (XUU). The central plane in the *y* direction (YC) was fixed in the *y* direction because of symmetry. No constraints were applied to the surfaces XLU, XUL and YU, which were free from traction.

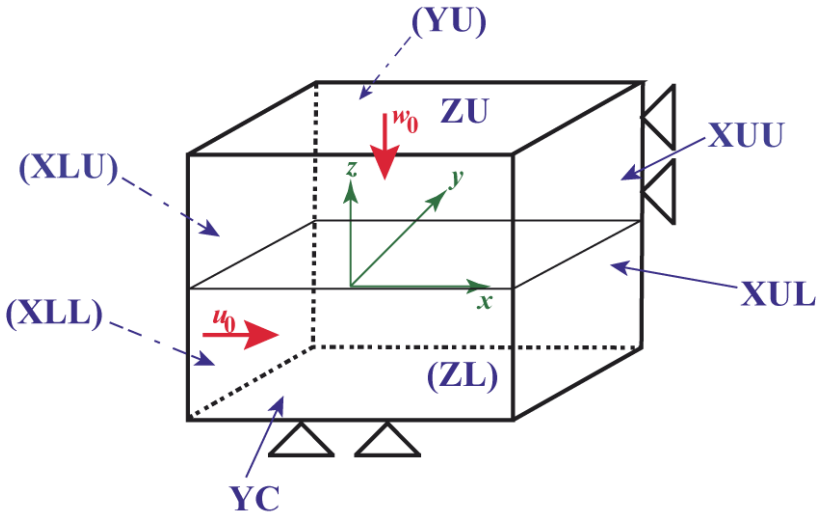

Fig. 2.8. Boundary conditions used in the FEM analysis for the direct shear test.

The uniform displacements (w_0) and (u_0) at the surfaces (ZU and XLL, respectively) represent the application of normal and shear loads with rigid plates and include two contributions; one for the displacements of intact rock (w_{0i} and u_{0i}) and one for those of the fracture (w_{0f} and u_{0f}). The values of these displacements were determined for the designated values of the normal (σ_n^*) and shear (τ^*) stresses under the assumption that the normal and shear stresses are uniform in the fracture, which, however, is not technically correct. For the intact specimen, only the former (w_{0i} and u_{0i}) were applied, as given by

$$w_{0i} = \frac{h}{E}\sigma_n^*, \qquad (2.11)$$

$$u_{0i} = \frac{2l^2}{hE}\tau^*,$$

where E is Young's modulus, l and h are the specimen length and height, respectively, and σ_n^* and τ^* are the designated values of the normal and shear stresses on the fracture (Table 2.2). The above equations are derived from the relation between the stress and strain in uniaxial compression of an intact rock in the z and x directions.

In the initial stage, the displacement applied to the upper surface (ZU) in the z direction for the fracture (w_{0f}) is given according to Eq. (2.5) by

$$w_{0f} = \frac{\ln(\sigma_n^*/A)}{B}, \tag{2.12}$$

while the uniform displacement applied to the surface (XLL) in the x direction for the fracture (u_{0f}) is given according to Eq. (2.6) by

$$u_{0f} = \frac{\tau^*}{C + D\sigma^*}. \tag{2.13}$$

In the residual stage, I only applied a small shear displacement to the surface (XLL) (u_{0f} = 0.1 mm) in addition to that of the intact specimen (u_{0i}, Eq. (2.11)), by assuming that a large shear displacement (δ = 7 mm) had already occurred. However, this large shear displacement (δ) was considered to estimate the SD of the initial aperture (s_a) according to Eq. (2.9), since the actual shear displacement is u_{0f} (0.1 mm) + u_{0i} + δ.
The displacement in the z direction at the surface (ZU) is given according to Eq. (2.10) by

$$w_{0f} = \frac{\ln(\sigma_n^*/A)}{B'} s_a. \tag{2.14}$$

Thus, the total displacements in the z and x directions (w_0 and u_0, respectively) for both the initial and residual stages are given by

$$\begin{aligned} w_0 &= w_{0i} + w_{0f}, \\ u_0 &= u_{0i} + u_{of}. \end{aligned} \tag{2.15}$$

For Model 3FX, for which the upper and lower surfaces of the specimen are fixed to the loading plates of each shear box, a uniform vertical displacement (w_0) given by Eq. (2.15) was applied to the whole upper and lower surfaces of the specimen, while for other models, for which the specimen is installed in the shear box without glue, partial separation between the upper and lower surfaces of the specimen and the loading plates was considered, as described in the next section.

From the solution of the nodal displacements, both the stress in solid rock and the normal and shear stresses on the fracture as well as the nodal forces (reactions) at the boundaries were determined. The mean values of the normal ($\bar{\sigma}_n$) and shear ($\bar{\tau}$)

stresses were determined from the sum of the normal load (N) on the upper/lower surface and that of the shear load (T) on the lower half of the left/upper half of the right end surface of the half specimen, as given by

$$\bar{\sigma}_n = \frac{2N}{bl}, \qquad \bar{\tau} = \frac{2T}{bl}. \tag{2.16}$$

Note that these mean normal and shear stresses are slightly different from the designated values used in the simulation, since the problem is not linear and the normal and shear stresses are not uniform in the fracture. The distributions of the tractions on the boundaries were determined from the normal stress at the nodes on the boundaries, since the stress can be defined at nodes for the quadratic elements. Furthermore, I determined from the distributions of the tractions the values of x_0 and z_0 where the resultant normal (N) and shear (T) loads act, respectively (Fig. 2.2).

2.4.3 Method of iterative calculation

Since Eqs. (2.4) and (2.7) are non-linear, and the shear stiffness depends on the normal stress (Eq. (2.6) in the initial stage), iteration was needed to satisfy these equations. Hence, the values for the normal and shear stiffness (k_n and k_s) were modified at all nodes according to the normal stress until these equations were satisfied. Furthermore, to satisfy Eq. (2.3) for the sliding condition in the residual stage, an iterative calculation was performed by changing the shear stiffness at nodes where τ is greater than $\mu|\sigma_n|$, so that Eq. (2.3) may be satisfied in the next iteration. Thus, to confirm that both the normal and shear stresses satisfy Eqs. (2.4) and (2.6) for the initial stage and Eqs. (2.3) and (2.7) for the residual stage, the calculation was repeated until the errors in these equations were less than 10^{-2} MPa. Since neither the normal nor shear stiffness are the same for all nodes of a joint element due to the non-uniform distributions of the normal and shear stresses, these stiffnesses at an arbitrary point in the joint element were interpolated from those at the nodes, as described previously.

To simulate partial separation between the upper and lower surfaces of the specimen and the loading plates, when the traction in the z direction (t_z) is tensile at a node on the upper and lower surfaces, the constraint of the displacement in the z direction ($w = w_0$ or 0) is released at that node, and when the displacement in the z direction at a free node is smaller than w_0 at the upper surface and smaller than zero at the lower surface, the

constraint of the displacement in the z direction is recovered at that node. These judgments were made based on a threshold value: tractions smaller than a certain value (10^{-2} MPa) were ignored and excluded from the analysis. The iteration continued until no changes were observed from constraint to release and vice versa.

2.5 Simulation results

2.5.1 Traction distributions on the loading planes

To illustrate the effects of both the specimen height, shape and the boundary conditions on the traction distributions on the loading surfaces of the specimen, Fig. 2.9 (a) and (b) shows the normalized traction distributions on the upper (ZU) surface along $y = 0$ (YC plane) for all models, including the intact specimen (e.g. Model 3I) and fixed boundary conditions (Model 3FX) in the initial stage (Fig. 2.9a) and in the residual stage (Fig. 2.9b). Since the mean normal stress ($\bar{\sigma}_n$) is slightly different between the models, the normal tractions (t_z) are normalized by the mean normal stress on the fracture ($\bar{\sigma}_n$), and the x coordinate is normalized by the length of the specimen (l). The tractions on the surfaces opposite the surface are symmetric with respect to the center of the specimen.

The traction on the upper surface is greatest at the right end and smallest at the left end, to balance the moment induced by the non-coaxial shear loads, as described previously. Note that moment equilibrium cannot be attained in the DST by boundary conditions with uniform normal tractions on the upper and lower surfaces of the specimen. The non-uniformity in traction on the upper surface decreases as the specimen height decreases and there is a long stable traction for the smallest specimen height (Model 3). The normal tractions on the upper surface are approximately zero in the vicinity of the left end for Models 1, 2 and 3, which indicates that the surface is partially separated from the loading plate. Fig. 2.9 also shows that the difference in the boundary conditions between the fixed (Model 3FX) and non-fixed (Model 3) interfaces does not significantly affect the traction distributions except in the vicinity of the left end, since the separated area occupies a very small portion for the mean normal and shear stresses (about 10 and 7 MPa, respectively). When the specimen does not have a fracture (Model 3I), the separation near the left end extends slightly, the maximum traction at the right end increases, and the distributions have a distinct local minimum and maximum. Moreover, when the result obtained for Model 3 (0.1 m × 0.08 m × 0.04 m) is compared to that obtained for Model 4 (0.2 m × 0.16 m × 0.08 m), the normalized traction distribution is almost the same for the normalized length, although they are

slightly different near both ends.

Fig. 2.9 (c) shows the difference in the normal tractions on the upper surface for both the initial and residual stages in Models 1 and 3. The tractions in the residual stage are slightly smaller than those in the initial stage since the fracture is softer in the residual stage.

A typical example of the separated area on the upper and lower surfaces is shown in Fig. 2.10 (a and b), respectively, for the initial stage of Model 3 (0.1 m × 0.08 m × 0.04 m). Open and solid circles indicate the nodes that are in contact with and are separated from the loading plate, respectively. Only the one half of the surfaces is shown in the figure since all nodes on the right/left half are in contact with the loading plate. A 3D effect is observed as the separated area slightly narrows in the *y* direction. Within the current designated stress values, separation between the loading plates and the upper and lower surfaces of the specimen occurs only in a small area near the left/right of the upper/lower surfaces. These separated areas ranged from 2.38 to 5.84 % of the whole area in all models. However, this separation should increase with an increase in the shear stress, when the normal stress is kept constant. Thus, the effect of partial separation may be significant when the shear stress is much greater than the normal stress.

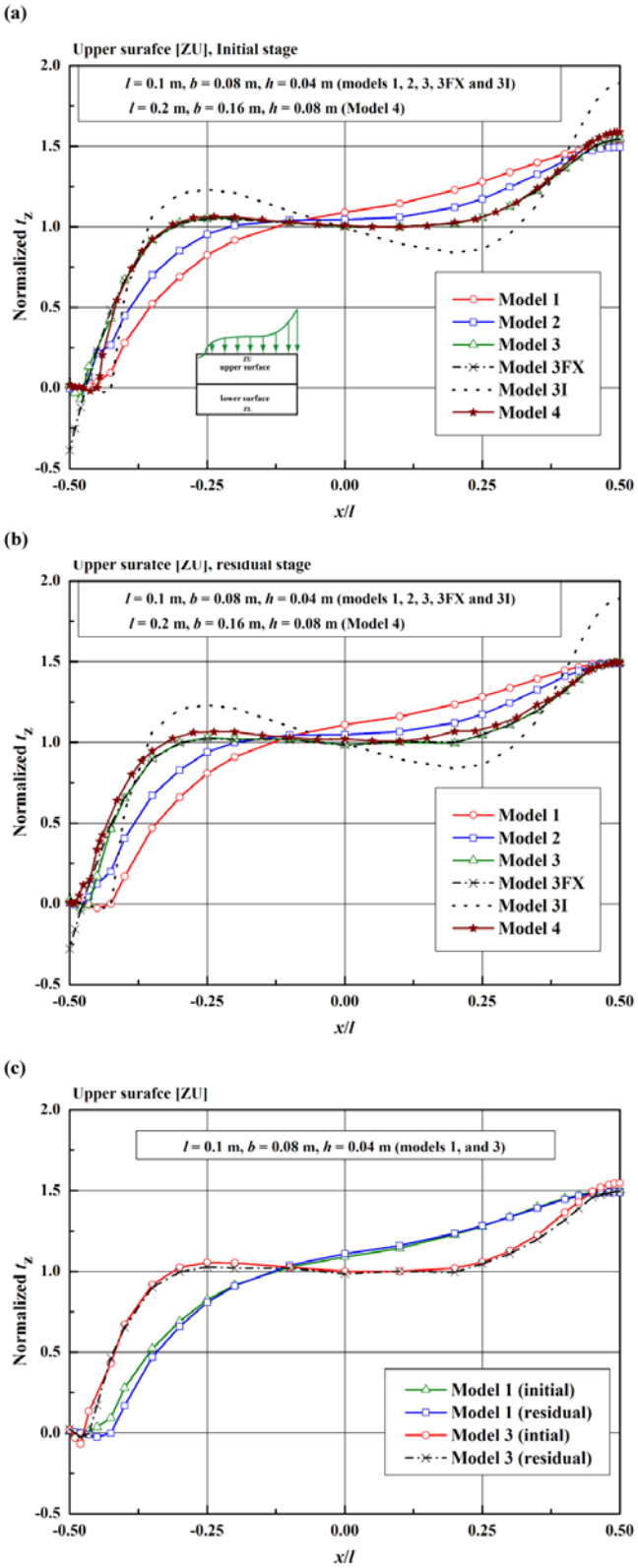

Fig. 2.9. Traction distributions on the upper surface of the specimen for all models in the (a) initial stage and (b) residual stage, and (c) for Models 1 and 3 in both the initial and residual stages.

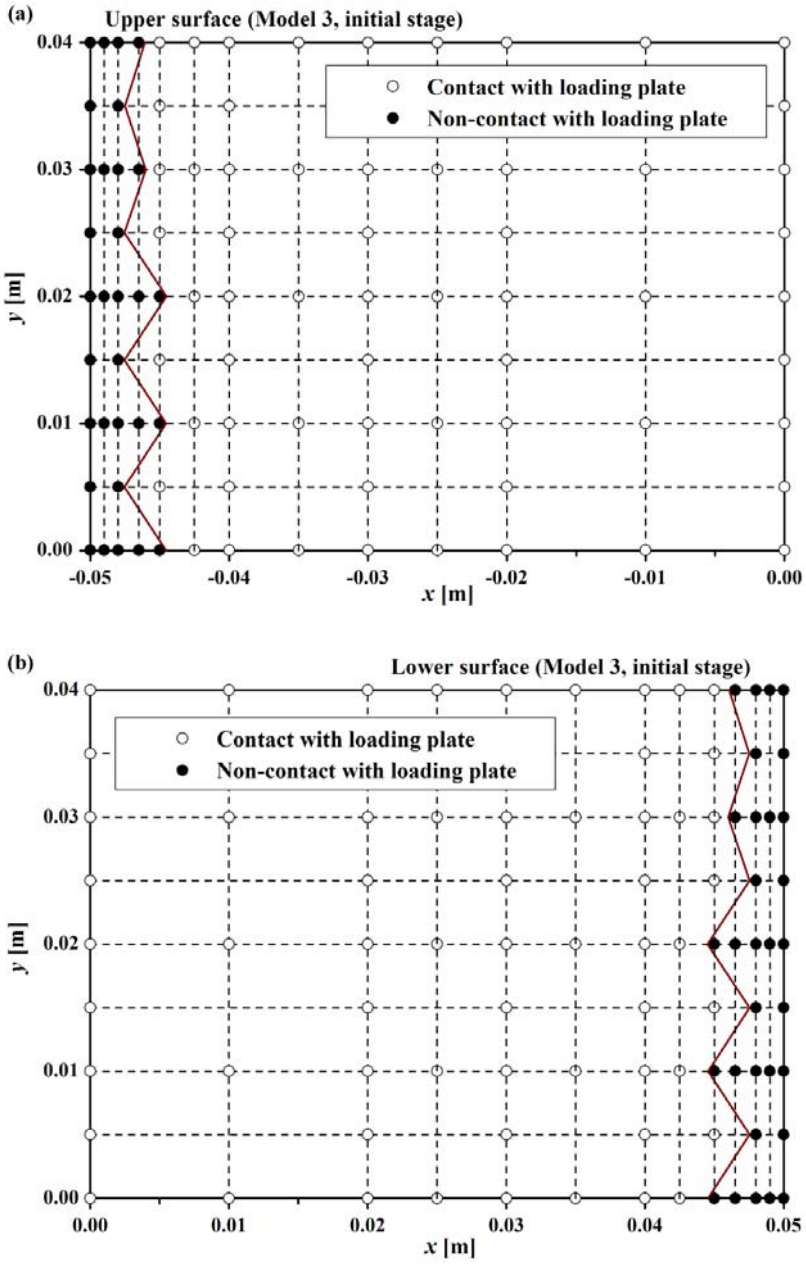

Fig. 2.10. An example of the separated area on the (a) upper and (b) lower surfaces of Model 3 in the initial stage.

Fig. 2.11 shows the normalized traction distributions on the lower half of the left end (XLL) surfaces along $y = 0$ (YC plane) for all models, including the intact specimen and fixed boundary conditions in the initial stage. The normal traction in the x direction (t_x) is normalized by the mean traction on the surface ($\bar{t}_x$), and the z coordinate is normalized by the specimen height (h). The traction on the lower half of the left end surface rapidly increases as the position approaches the middle height of the specimen. The non-uniformity in the traction distribution decreases as the specimen height decreases, similar to that on the upper surface. When the results obtained for Model 4 (0.2 m × 0.16 m × 0.08 m) are compared to those obtained for Model 3 (0.1 m × 0.08 m × 0.04 m), the normalized tractions are almost the same for the normalized length, although the maximum tractions are slightly different. Regarding the influence of different boundary conditions, the results again showed that there is no significant effect on the traction on the lower half of the left end surface. When the specimen does not have a fracture (Model 3I), the normal traction is very large at the middle height of the specimen, similar to the stress produced in an elastic half-space by the action of a rigid punch, which is infinite at the edge of the punch [135].

Thus, the normal tractions on both the upper and the lower half of the left end surfaces are never uniform, and the non-uniformity in the traction distributions on these surfaces decreases with a decrease in the specimen height. Furthermore, the effect of partial separation on the upper and lower surfaces of the specimen is small for the mean normal and shear stresses used in this study. Similar results were obtained for the fractured specimens in the residual stage.

2.5.2 Normal and shear stresses in the central plane

Fig. 2.12 and Fig. 2.13 show a comparison of the contour maps of σ_z and τ_{zx} in the central (YC) plane ($y = 0$, Fig. 2.8) between (a & b) the intact specimen, (c & d) the fractured specimen in the initial stage and (e & f) the fractured specimen in the residual stage for Models 1 & 3, respectively. As the position approaches the middle specimen height, the highly non-uniform normal tractions ($t_z = \sigma_z$) on the upper and lower surfaces change to be relatively uniform in the middle of the specimen height, but leave concentrations near the end edges for both the intact and fractured specimens. The distribution of σ_z at the middle specimen height is more uniform for the fractured specimen than for the intact specimen. In contrast, the value of τ_{zx}, which is zero on the upper and lower surfaces, increases as the position approaches the middle specimen height, and concentration occurs near the end edges for both the intact and fractured specimens, similar to the distribution of σ_z. The distribution of τ_{zx} at the middle

specimen height of the fractured specimen is fairly uniform in the middle of the specimen length, while it is not uniform for the intact specimen. Thus, a fracture produces a much more uniform distribution of σ_z and τ_{zx} in the fracture than a specimen without a fracture.

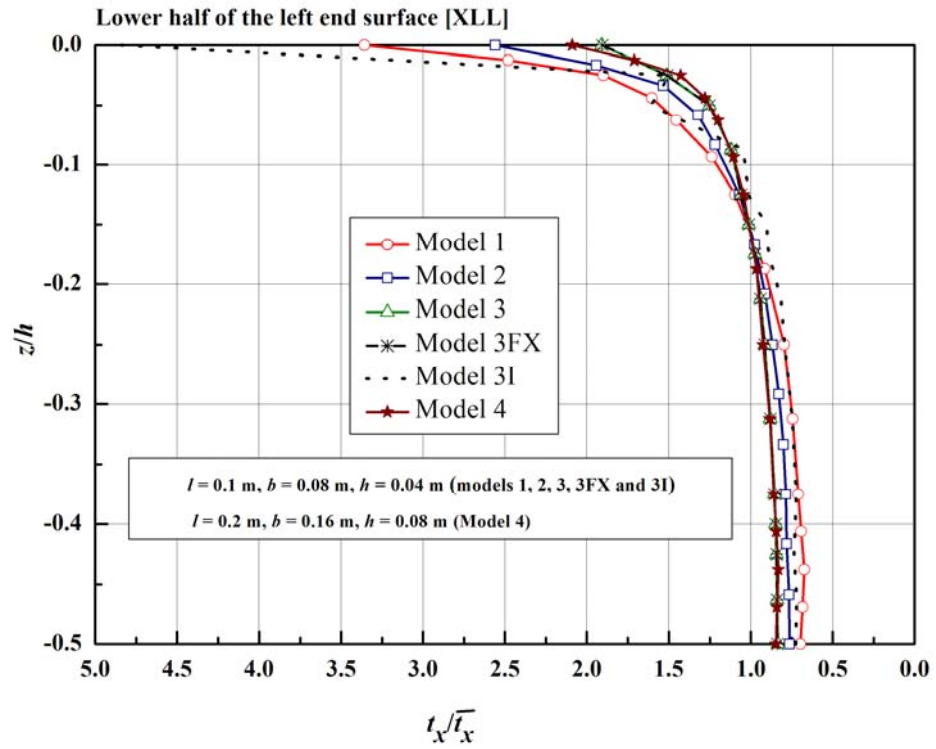

Fig. 2.11. Traction distributions for all models on the lower half of the left end surface of the specimen.

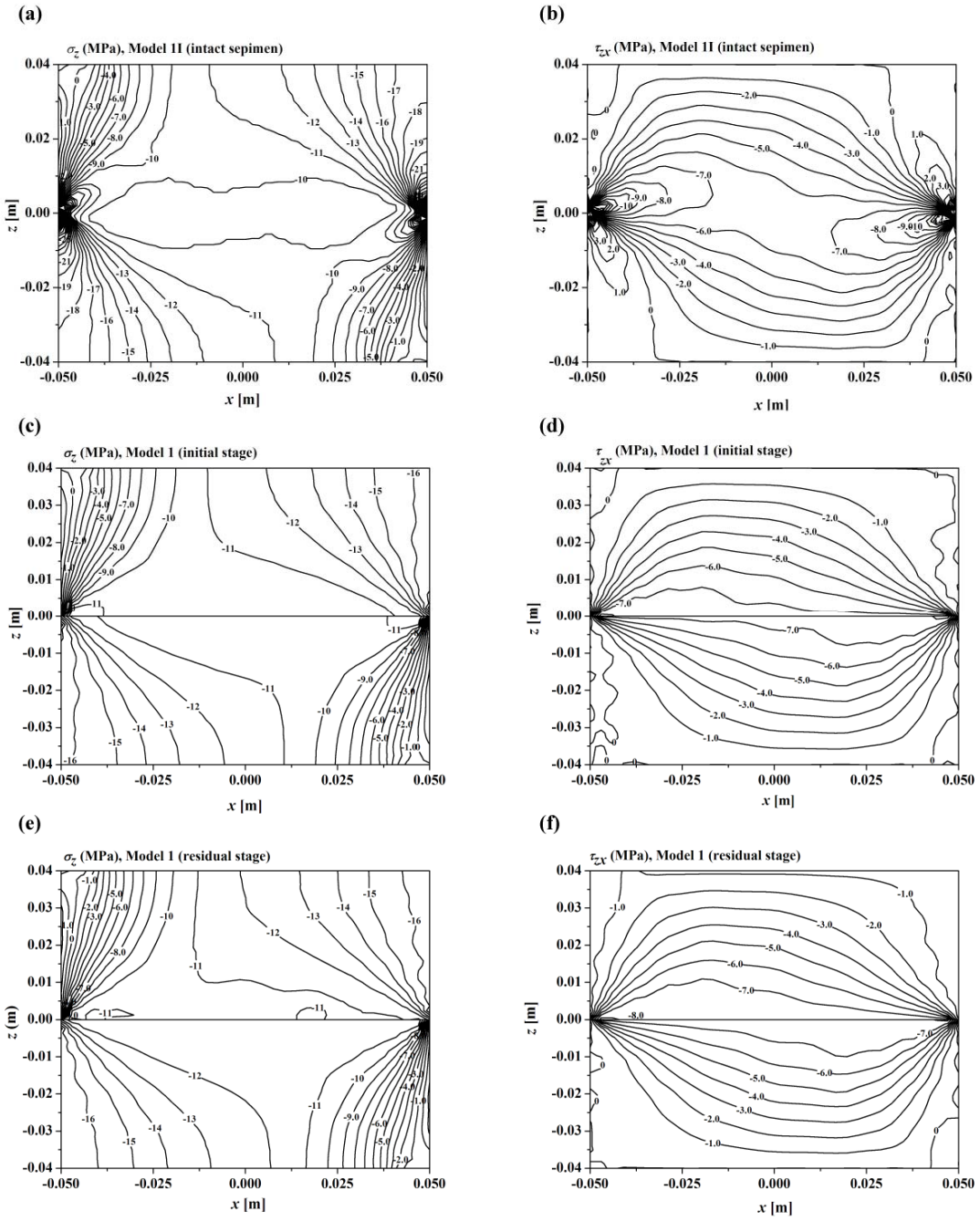

Fig. 2.12. Comparison of the contour maps of (a & b) σ_z and τ_{zx} in the YC plane for the intact specimen (Model 1I) with (c & d) those for the fractured specimen (Model 1) in the initial stage and (e & f) those for the fractured specimen (Model 1) in the residual stage.

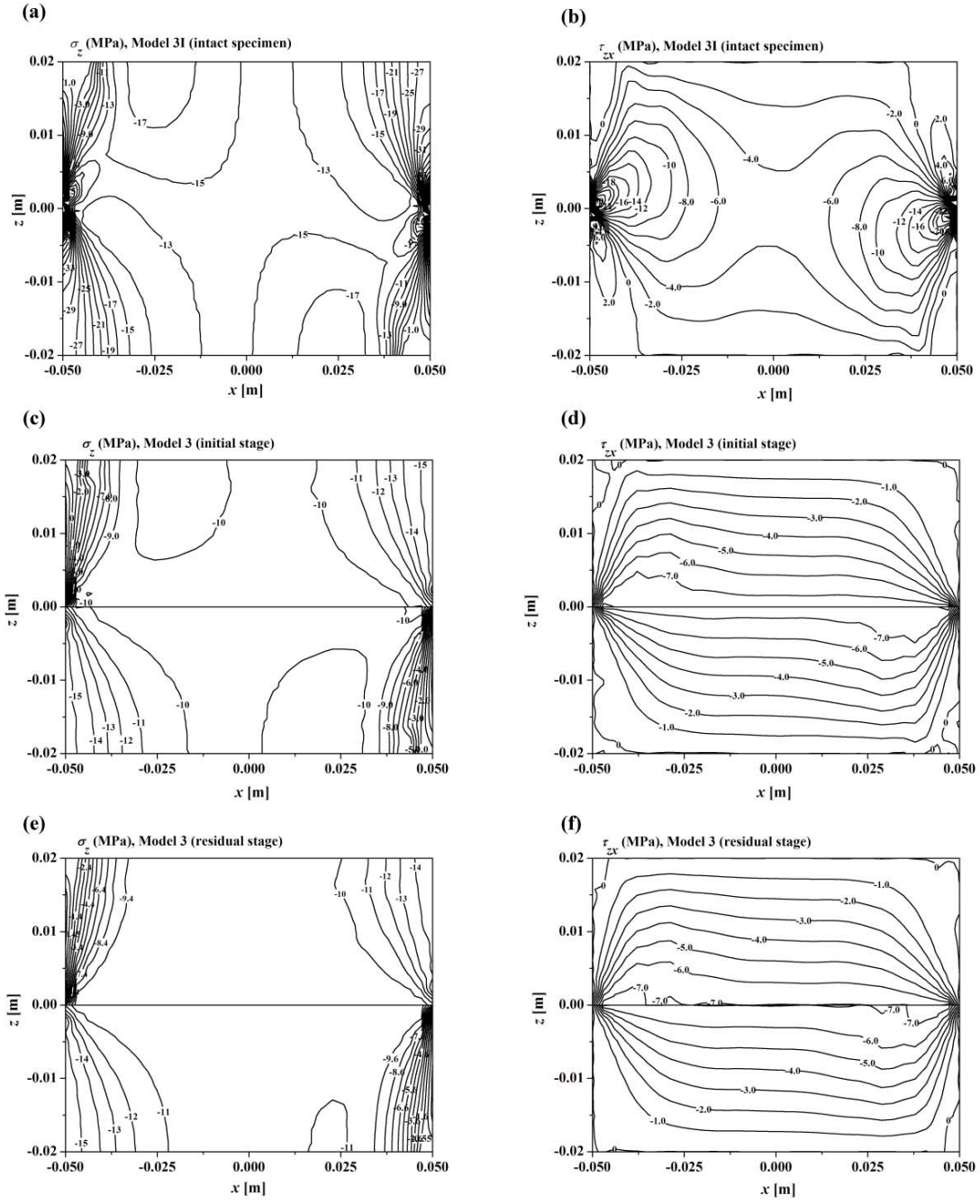

Fig. 2.13. Comparison of the contour maps of (a & b) σ_z and τ_{zx} in the YC plane for the intact specimen (Model 3I) with (c & d) those for the fractured specimen (Model 3) in the initial stage and (e & f) those for the fractured specimen (Model 3) in the residual stage.

2.5.3 Distributions of the normal and shear stresses in the fracture/shear plane

Since the mean values of the normal ($\bar{\sigma}_n$) and shear ($\bar{\tau}$) stresses obtained in the analyses (Eq. 2.16) were slightly different among the cases, ranging from 9.9 to 11.0 MPa and 7.0 to 7.7 MPa, respectively, both the normal and shear stresses in the shear/fracture plane were normalized by the mean values of the normal and shear stresses. Fig. 2.14 shows the distributions of the normalized normal and shear stresses along the *x*-axis at the middle height and the middle width ($y = z = 0$) in the shear/fracture plane for Models 1, 2, 3, intact specimen (Models 1I, 2I, 3I) and 3FX (fixed boundary condition). Figs. 2.14 (a) and (b) show the results for the intact specimen, Figs. 2.14 (c) and (d) show those for the fractured specimen in the initial stage and Figs. 2.14 (e) and (f) show those for the fractured specimen in the residual stage. Note that the scales on the vertical axis are different among the cases to clearly show the effect of specimen height. Since there is a 3D effect in the *y* direction on the normal and shear stresses, as described later, the mean values determined for the whole plane ($\bar{\sigma}_n$ and $\bar{\tau}$) are slightly different from those determined for the line $y = z = 0$.

The effect of the fixed boundary condition is again negligibly small, since the area of separation is very small (Fig. 2.10). In the shear plane/fracture, the normal and shear stresses are more or less concentrated near the end edges of the specimens while they are relatively uniform in the central part for all cases, except for the shear stress in the intact specimen (Fig. 2.14b), for which there are no regions of uniform stress. The concentrations of the normal and shear stresses in the fracture are much smaller than those in the shear plane of the intact specimen. This is because the fracture acts as a soft layer and the stresses are relaxed in the fractured specimen due to large deformation. Accordingly, the stress concentrations in the residual stage are smaller than those in the initial stage (Figs. 2.14c to 2.14f). As the specimen height (*h*) decreases for the fractured specimens, the concentration of stress at the edges of the fracture decreases and the lengths of uniform normal and shear stresses increase. Thus, these results suggest that the stress concentration is mainly governed by the specimen height, similar to the traction distributions on the loading surfaces. Hence, careful attention should be paid to the specimen height when the DST is performed. In contrast, the stress concentration in the intact rock (Figs. 2.14a and 2.14b) increases with a decrease in the specimen height. The cause for this tendency is still under investigation.

While the shear stress is maximum at the edges of the fracture for the fractured specimen, it is maximum near the side surfaces and zero at the side surfaces of the intact specimen (Figs. 2.14b, d and f). I assumed that the shear stress (friction) is zero in all

outer surfaces for both the intact and fractured specimens, as described previously. Accordingly, the shear stress on the plane perpendicular to the outer surfaces, such as the shear plane, should be zero at the edges since the conjugate shear stress on the outer surfaces is zero. However, this does not hold for a fractured specimen, since non-zero shear stress is produced even at the edges of the fracture by non-zero shear displacement, whereas there is no shear stress on the outer surfaces. Thus, the condition of shear stress is singular at the edges of a fracture for a fractured specimen.

Fig. 2.15 shows the influence of the specimen height/shape (Models 1, 3 and 4) on the distribution of the normalized normal and shear stresses along the line $y = z = 0$ in both the initial and residual stages. The x coordinate is normalized by the length of the specimen (l). For the initial stage, the concentrations of these stresses at the edges of the fracture for Model 4 are similar to those for Model 1 with the same height rather than those for Model 3 with the same area, although this tendency was not clearly observed for the residual stage since the concentration is not so large. Thus, these results suggest that the stress concentration is mainly governed by the specimen height rather than the specimen shape.

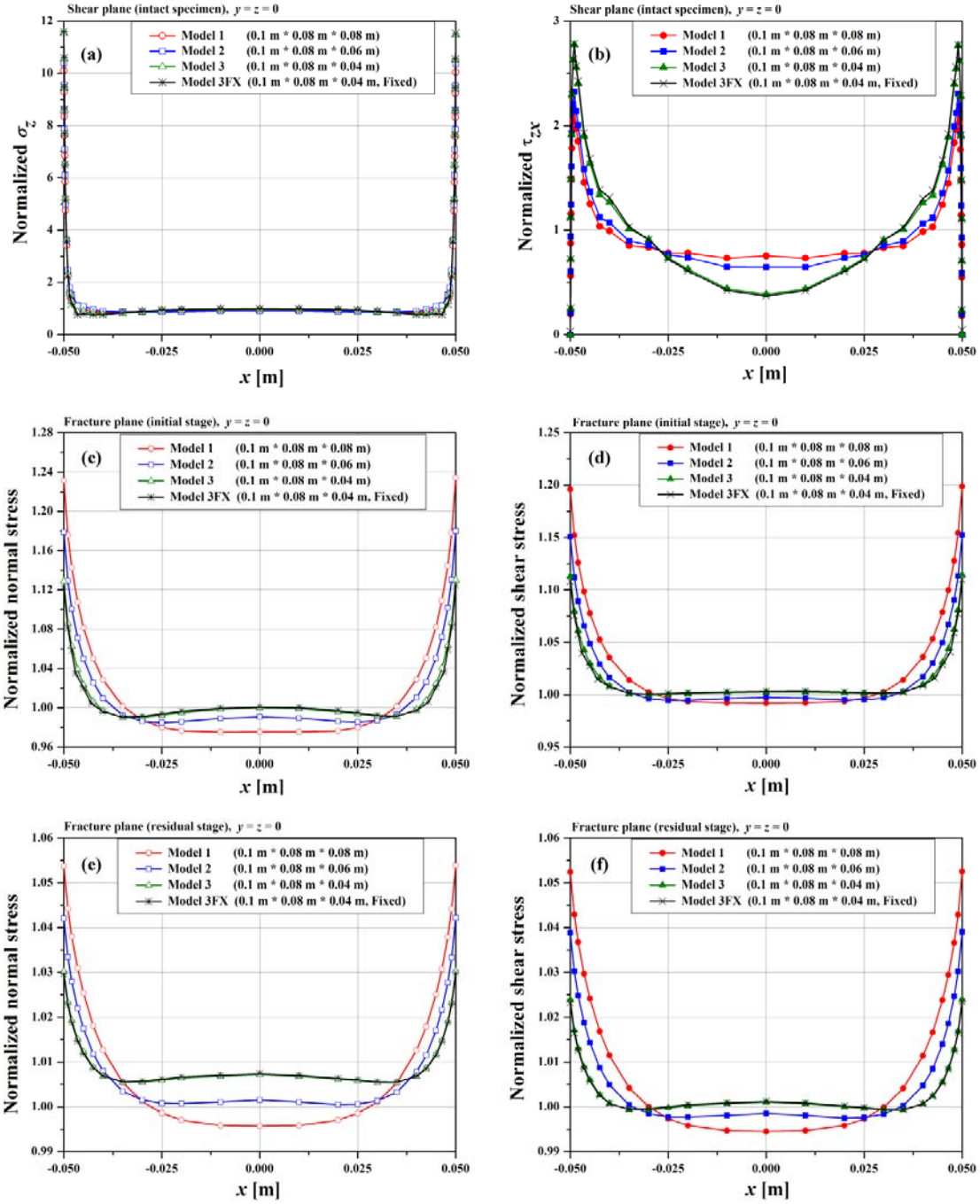

Fig. 2.14. Distributions of the normalized normal and shear stresses along the line $y = z = 0$ for the intact specimen (a and b), the fractured specimen in the initial stage (c and d), and the fractured specimen in the residual stage (e and f) (Models 1, 2, 3, 1I, 2I and 3I).

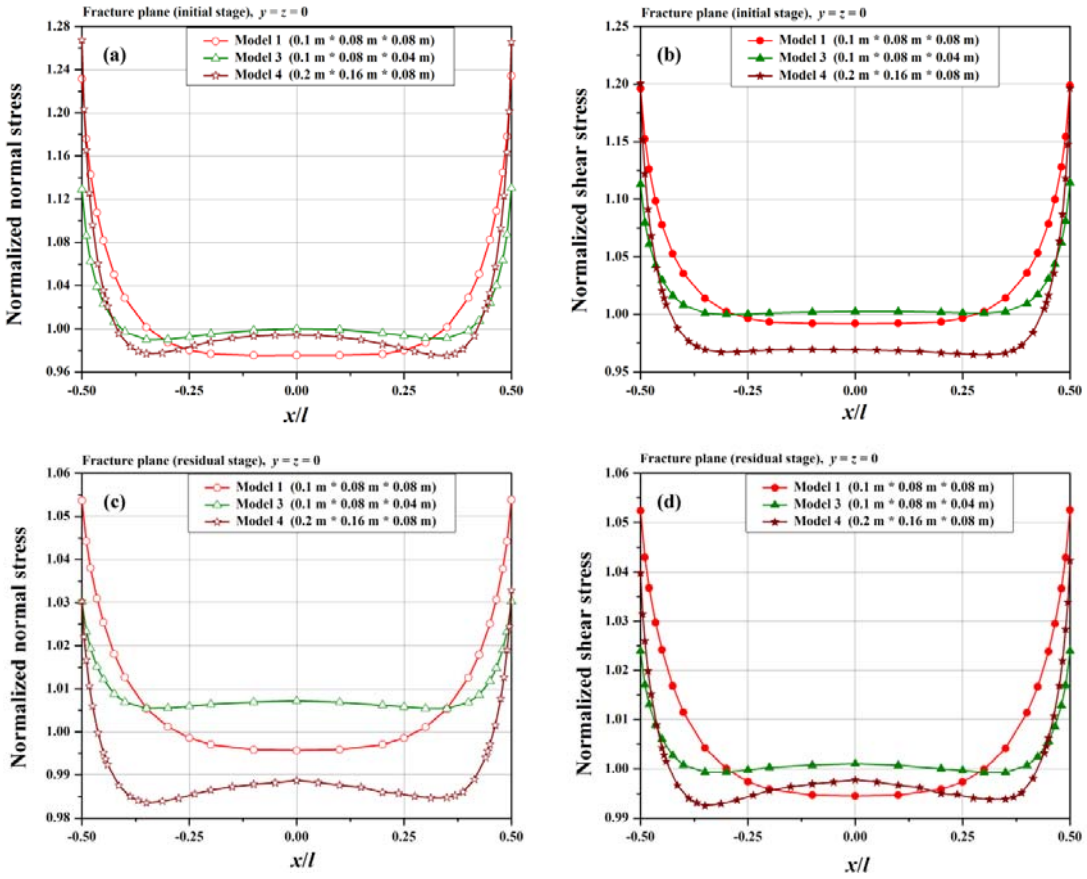

Fig. 2.15. Effects of specimen shape on the distributions of the normalized normal and shear stresses in the fracture plane in the initial (a and b) and residual (c and d) stages for Models 1, 3 and 4.

2.5.4 Distributions of closure and shear displacement

To quantitatively evaluate the effect of the specimen height on closure and shear displacement, the closure and shear displacement were normalized by the mean values, determined in each stage for the whole plane of the fracture. The mean closure was about 0.1 mm and 0.6 mm and the mean shear displacement was about 1 mm and 7.1 mm in the initial and residual stages, respectively. The distributions of the normalized closure and shear displacement along the x-axis at the middle height and the middle width ($y = z = 0$) in the fracture are shown in Fig. 2.16 for Models 1, 2 and 3. The difference in boundary conditions between Model 3 and Model 3FX has no significant effect on the deformations, and I do not show the results. Furthermore, the concentrations of the deformations were mainly governed by the specimen height rather than the specimen shape, similar to those of the stresses. Figs. 2.16 (a) and (b) show the closure in the initial and residual stages, respectively, and Figs. 2.16 (c) and (d) show the shear displacement in the initial and residual stages, respectively.

As a result of the concentration of the normal and shear stresses near the end edges of the fracture (Fig. 2.14), the normalized closure and shear displacement are also concentrated near the end edges of the fracture, while there is no region where the shear displacement is uniform. The concentration of the closure decreases with a decrease in the specimen height, similar to that of the normal stress. In contrast, the concentration of the shear displacement increases with a decrease in the specimen height, opposite that of the shear stress. This result regarding shear displacement is due to the dependence of the shear stiffness on the normal stress, i.e., since the concentration of the normal stress increases with the specimen height, the shear stiffness near the edges of the fracture increases with the specimen height (Eq. (2.6)) and, as a result, the shear displacement decreases with the specimen height.

However, these concentrations of deformation are not so significant for both the closure and shear displacement, and that of shear displacement is smaller than that of closure by about one order of magnitude. This small value for the concentration of closure compared to the normal stress is due to the non-linear behavior of closure: i.e., closure does not significantly increase with normal stress at large normal stresses (Fig. 2.17). The concentration of shear displacement in the initial stage is very small since the shear stiffness increases as the concentration of normal stress increases (Eq. (2.6)), and the further smaller value of that in the residual stage is due to the large mean value of the shear displacement by which the result was normalized.

Shear dilation may occur with the shear displacement, depending on the fracture geometry, when the normal stress is small. As a result, closure of the fracture changes to open the fracture due to shear dilation. Therefore, dilation of the fracture should be added to the closure value obtained in this work, and the non-uniformity in the closure depends on that in shear displacement. However, as shown in Figs. 2.16 (c) and (d), since the non-uniformity in the shear displacement is negligible, the effect of shear dilation on the non-uniformity in the closure of the fracture may also be negligible within the range of this study.

Fig. 2.18 shows a comparison of the closure results obtained at all nodes of the fracture in the initial and residual stages with the values estimated by Eqs. (2.4) and (2.7). Clearly, the simulated results are in agreement with the equations.

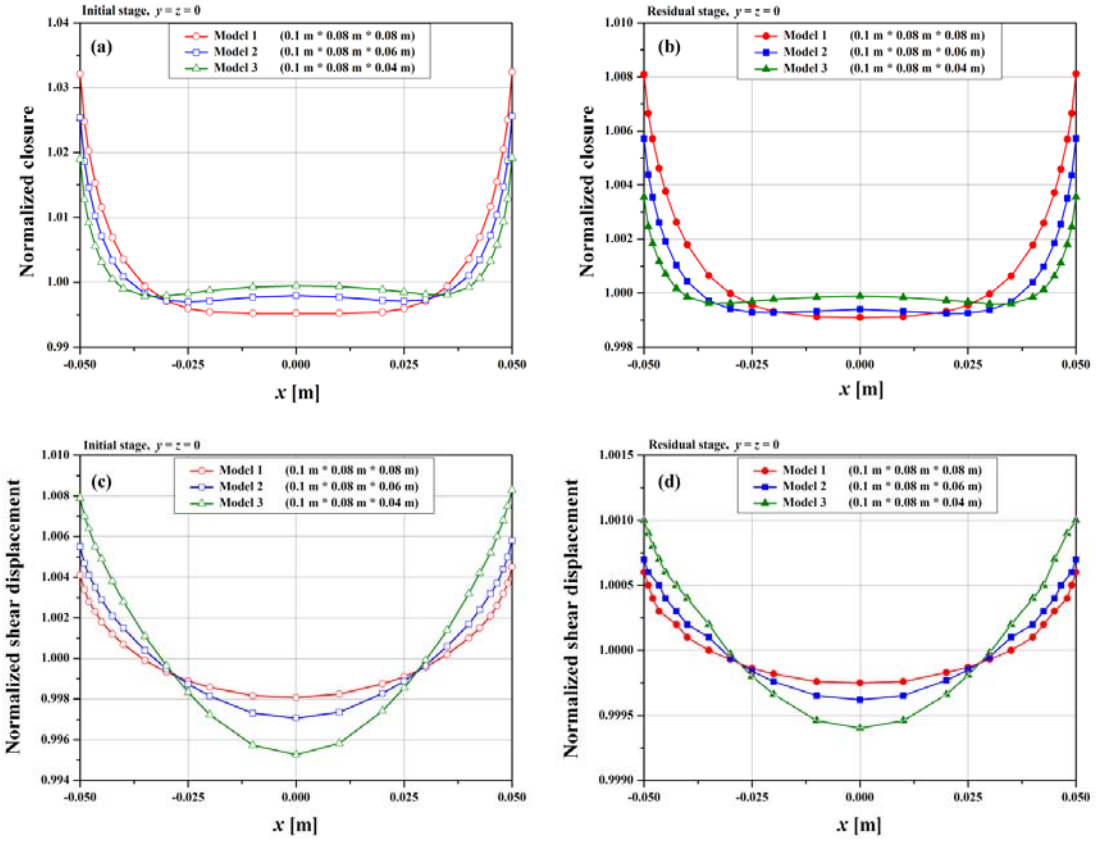

Fig. 2.16. Concentrations of closure in (a) the initial and (b) residual stages, and those of shear displacement in (c) the initial and (d) residual stages for Models 1, 2 and 3.

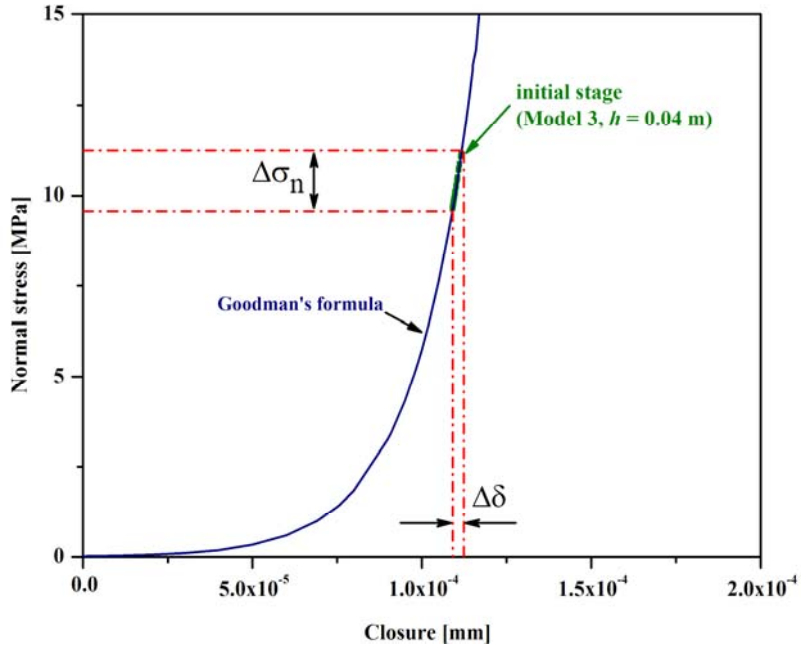

Fig. 2.17. Effect of the non linearity of closure curve on its concentration.

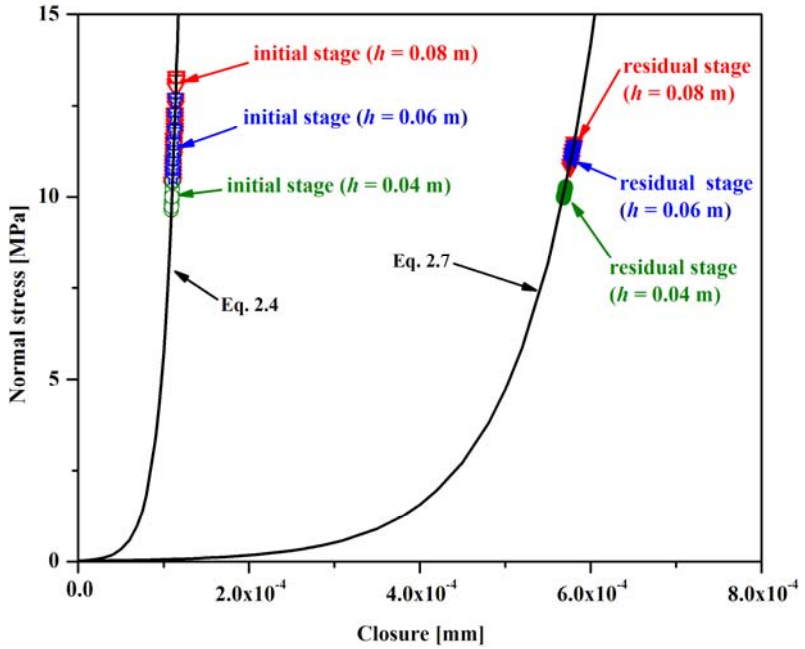

Fig. 2.18. Relation between normal stress and closure for fractured models.

2.5.5 Concentrations of the stress and deformation at the edges of the fracture

Fig. 2.19 shows the variation in the concentrations of the stresses and deformations at the edges of the fracture ($x = \pm 0.05$ m) along the y-axis. These values were obtained by normalizing the stress and deformation by their mean values (Eq. (2.16) for the normal and shear stresses). Figs. 2.19 (a) and (b) illustrate the concentrations of the normal and shear stresses and Figs. 2.19 (c) and (11) show those of the deformations, in both the initial and residual stages. As stated earlier, there is a 3D effect on the stresses and deformations, since the back surface with $y = b/2$ (YU in Fig. 2.8) is in a plane stress condition and the stress condition deviates further from plane stress as the position approaches the central plane with $y = 0$ (YC). The concentrations of the normal and shear stresses and closure decrease as the y position approaches the back/front surface, while the shear displacement is approximately constant. Clearly, as the specimen height decreases, the concentrations of the normal and shear stresses and the closure decrease for both the initial and residual stages, while those of the shear displacement are not significantly affected by the specimen height, due to the dependence of the shear stiffness on the normal stress, as described previously.

The mean values of these concentrations at the edges are summarized in Table 2.4 for the fractured specimen (Models 1, 2 and 3), together with the value of z_0 (Fig. 2.2). Similar to the concentrations of the stresses, the value of z_0 decreases with specimen height in both the initial and residual stages. Fig. 2.20 shows the relation between the value of z_0 and the mean concentrations of the normal (σ_n) and shear (τ) stresses and closure (Δu_z) at the edges of the fracture in both the initial and residual stages. The lines in the figure indicate the regression lines that were determined by the least squares method under the assumption that the concentrations are one when $z_0 = 0$. These concentrations increase approximately linearly with the value of z_0. Thus, the effect of specimen height on the concentrations of the normal and shear stresses and closure in the fracture can be attributed to that of the moment produced by the shear loads since the moment increases in proportion to the vertical distance ($2z_0$) between the two shear loads for the same shear load (Eq. (2.1)).

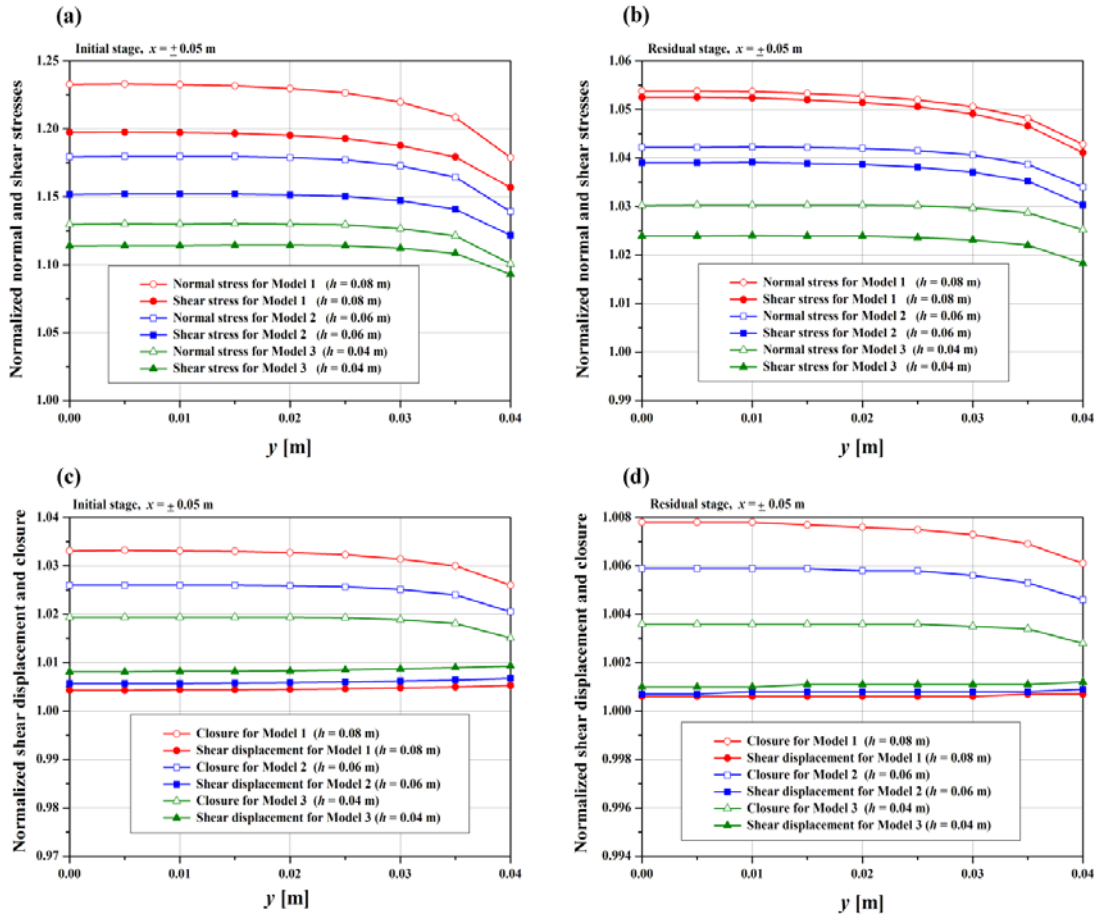

Fig. 2.19. Concentrations of both the normal and shear stresses along the edges of the fracture in (a) the initial and (b) residual stages, and those of both closure and shear displacement in (c) the initial and (d) residual stages for Models 1, 2 and 3.

As shown in Table 2.4, an increase in closure at the edges is at most 3.2% of the mean value in the initial stage and at most 0.7% of the mean value in the residual stage. Thus, the concentration of closure may not significantly affect the estimation of the hydraulic conductivity of the fracture within the range of this study. However, the closure concentration may increase with an increase in the shear stress, since the moment produced by the shear loads increases with an increase in shear stress. Therefore, further investigation of the effect of the magnitudes of the applied normal and shear stresses on the stress and deformation in the fracture is needed before more comprehensive conclusions can be drawn.

Table 2.4. Mean values of the concentration of the stress and deformation at the edges of the fracture and the value of z_0.

Stage	Model	Height (m)	z_0 (m)	Mean concentration			
				Normal stress	Shear stress	Closure	Shear displacement
Initial	Model 1	0.08	0.0159	1.223	1.190	1.032	1.005
	Model 2	0.06	0.0127	1.174	1.148	1.025	1.006
	Model 3	0.04	0.0090	1.127	1.112	1.019	1.008
Residual	Model 1	0.08	0.0161	1.052	1.050	1.007	1.0006
	Model 2	0.06	0.0128	1.041	1.038	1.006	1.0007
	Model 3	0.04	0.0090	1.030	1.023	1.004	1.001

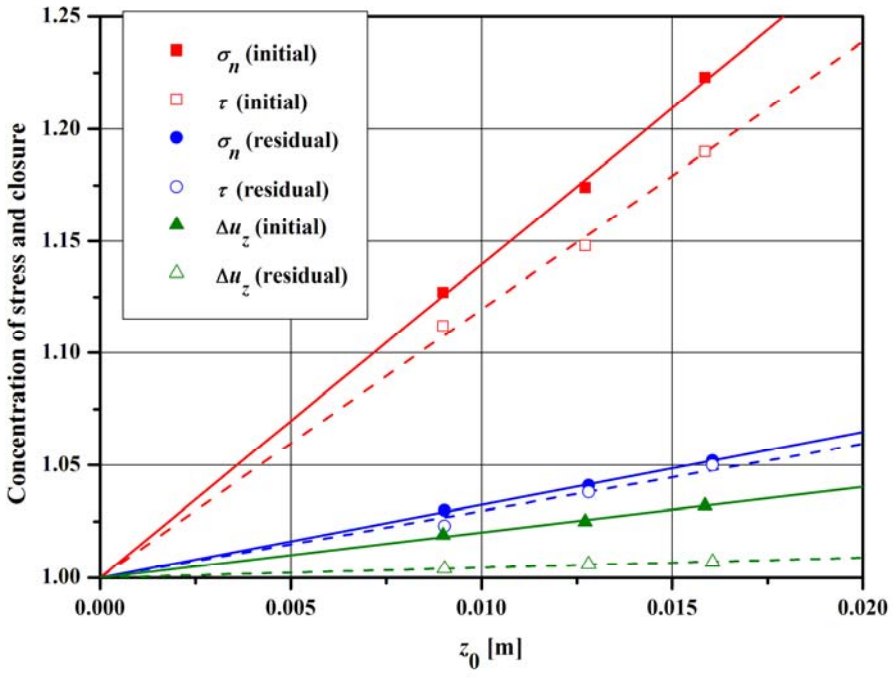

Fig. 2.20. Relation between the value of z_0 and the mean concentrations of the normal and shear stresses and closure at the edges of the fracture in the initial and residual stages.

2.6 Summary

To examine the validity of the DST for a rock fracture and to clarify the effect of specimen height and shape, I analyzed both the stress and deformation in fractured specimens with four different sizes in the DST for a limited case of a set of normal and shear stresses (σ_n = 10 MPa and τ = 7 MPa) by using 3D FEM with quadratic joint elements. By considering partial separation that could occur between the loading plates and the upper and lower surfaces of the specimen, the simulation was performed for both the initial stage with a small shear displacement and the residual stage with a large shear displacement, as well as for non-fractured specimens that were used as a reference. The constitutive law of the fracture, which considers the dependence of the non-linear behavior of the closure on the shear displacement and the dependence of the shear stiffness on the normal stress, was determined based on the experimental results obtained for tensile fractures in Inada granite and implemented in the simulation code to express a conceptional fracture with uniform properties to extract only the effect of the non-uniform tractions on the stress and deformation in the fracture, excluding the effect of the surface roughness on the local concentration of stress.

The non-uniformity of the traction distribution on the loading surfaces decreases as

the specimen height decreases. Partial separation occupies only a small area in the loading surfaces and does not significantly affect the traction distributions or the mechanical behaviors of the fracture, for the values of the normal and shear stresses used in this study. The normal and shear stresses are significantly concentrated near the edges of the fracture, and are relatively uniform in the central part of the fracture. The concentrations of the normal and shear stresses in the fracture are much smaller than those in the intact specimen, since the fracture acts as a soft layer. Thus, the stress concentrations in the residual stage are smaller than those in the initial stage. Furthermore, the stress concentrations decrease with a decrease in the specimen height, which can be attributed to the fact that the moment produced by the shear loads decreases with a decrease in the specimen height. The closure value is greater near the edges of the fracture where the normal stress is concentrated, and the concentration of closure increases with specimen height. However, this concentration of closure is not so significant due to the non-linear behavior of closure, i.e., closure does not significantly increase with normal stress at large normal stresses. Although the shear displacement is also greater near the edges of the fracture, the concentration of the shear displacement is much smaller than that of the closure since the shear stiffness increases with the normal stress.

Finally, based on this numerical investigation, a decision was made to use the smallest practical specimen height (h = 80 mm) throughout the experimental work since the height of 40 mm is too thin to avoid fracturing in the specimen when a normal stress is applied to the upper and lower surfaces.

3. TESTING APPARATUS AND EXPERIMENTAL METHOD

3.1 Development of direct shear test apparatus

One of the primary objectives of this work is to better understand the mechanism for the size effect on the mechanical behavior of a sheared fracture, including damage evolution under different normal stresses. Therefore, after discussing the importance of utilizing a direct shear apparatus under a constant normal load (CNL) condition, the decision was made to develop a compact direct shear test apparatus.

Thus, in order to investigate the effect of both size and normal stress on the shear behavior, a compact direct shear apparatus was designed, which consists of a shear box, a hydraulic-servo actuator unit for shear load and measuring devices for shear and normal displacements. The normal load is applied by a servo-controlled testing machine (Instron 8803).

3.1.1 Mechanical part

Fig. 3.1 and Fig. 3.2 present a general view of the direct shear apparatus. This test apparatus consists of the following units:

1) The shear box which measures 222 × 202 × 80 mm, and consists of the lower and upper parts (Fig. 3.2(a)).
2) Shear loading unit: Load cell (tension/contraction types, capacity 500 kN) for measuring shear load is set in the two rods which are connected to both the shear box and a reaction plate, as shown in Figs. 3.1 and Fig. 3.2 (a) to (c). The horizontal jack for the shear load, the fracture surface and the load cells are arranged at the same height so that no moment may be produced in the shear box. The shear loads measured by the two load cells are averaged. The friction between the lower and upper parts of shear boxes is not generated since they are fully separated (Fig. 3.2 (a)).
3) Normal loading apparatus (8803 system, Instron, Fig. 3.2 (d)) with a capacity of 500 kN: Normal load is applied by a servo-controlled hydraulic ram through a hydraulic pump. This normal loading apparatus is set on the upper part of the shear box at the center of a specimen. It should be emphasized that the center of the upper shear box is always in the same position and does not shift during shearing. The friction between the upper shear box and the normal load cell is negligible because of the small deformation of the load cell.

Fracture is sheared by moving the lower part of the shear box with the horizontal jack. The upper part of the shear box is connected by a pair of tie rods which allows the upper box to move vertically, but the horizontal movement is restricted (Fig. 3.2 (a) and (c)).

3.1.2 Control and data acquisition unit

Normal and shear loads, which are controlled independently by two servo systems, can be arbitrarily applied on the sample within the maximum shear and normal loads of 500 kN. Normal displacements are measured by four displacement transducers (DT) (strain-gauge-type with resolution of 0.5×10^{-4} mm/10^{-6} strain) that are attached on top of the upper shear box (Fig. 3.2(a) and Fig. 3.3 (a)) and averaged. Shear displacement is measured by one displacement transducer that is attached between the horizontal jack and the upper shear box, as shown in Fig. 3.3(b). The maximum shear displacement is 20 mm. The loads and displacements in the normal and shear directions, measured with the load cells or the displacement transducers, were digitally recorded every 5 sec with a PC.

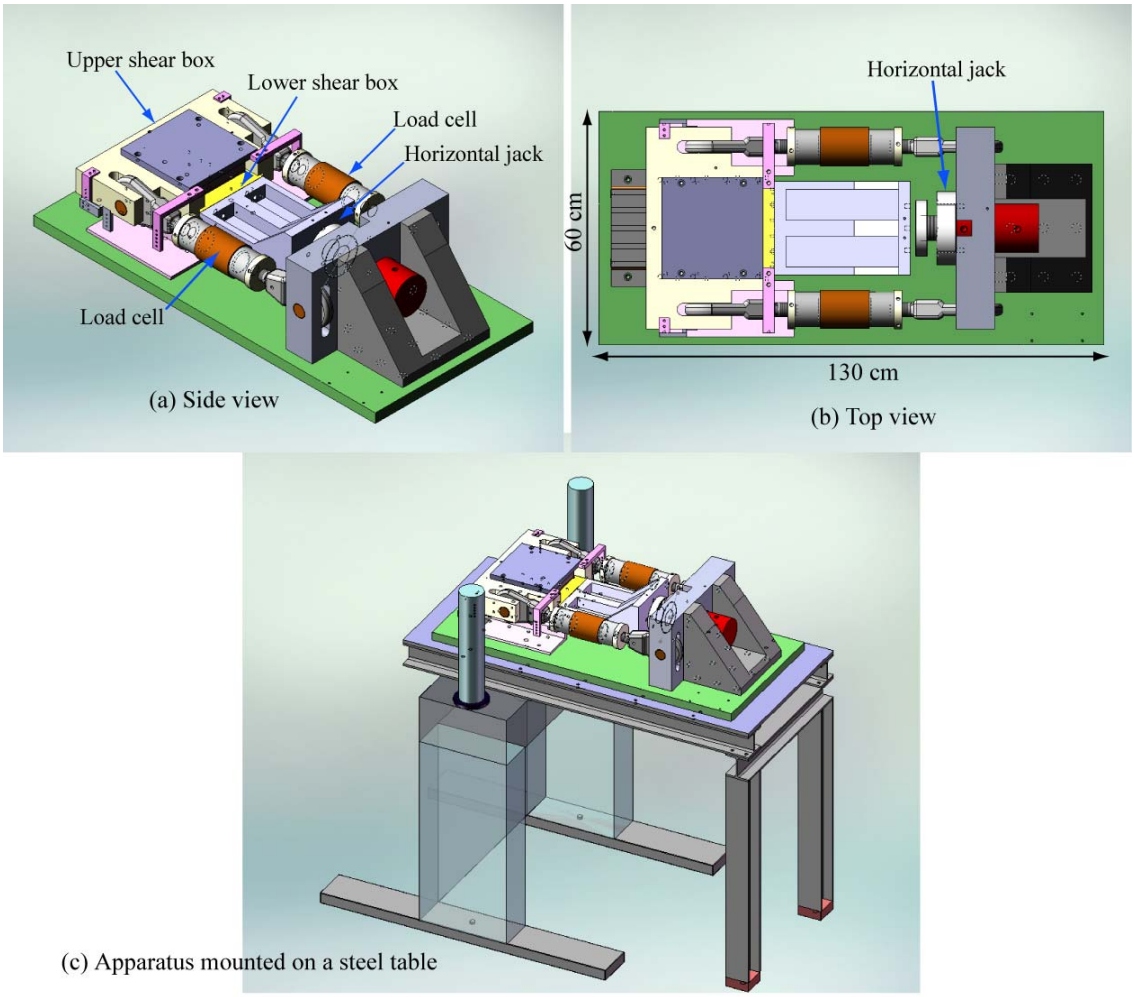

Fig. 3.1. The direct shear teat apparatus ((a) side view, (b) top view, (c) the apparatus mounted on a steel table to be connected to Instron 8803 and (d) the apparatus dimensions).

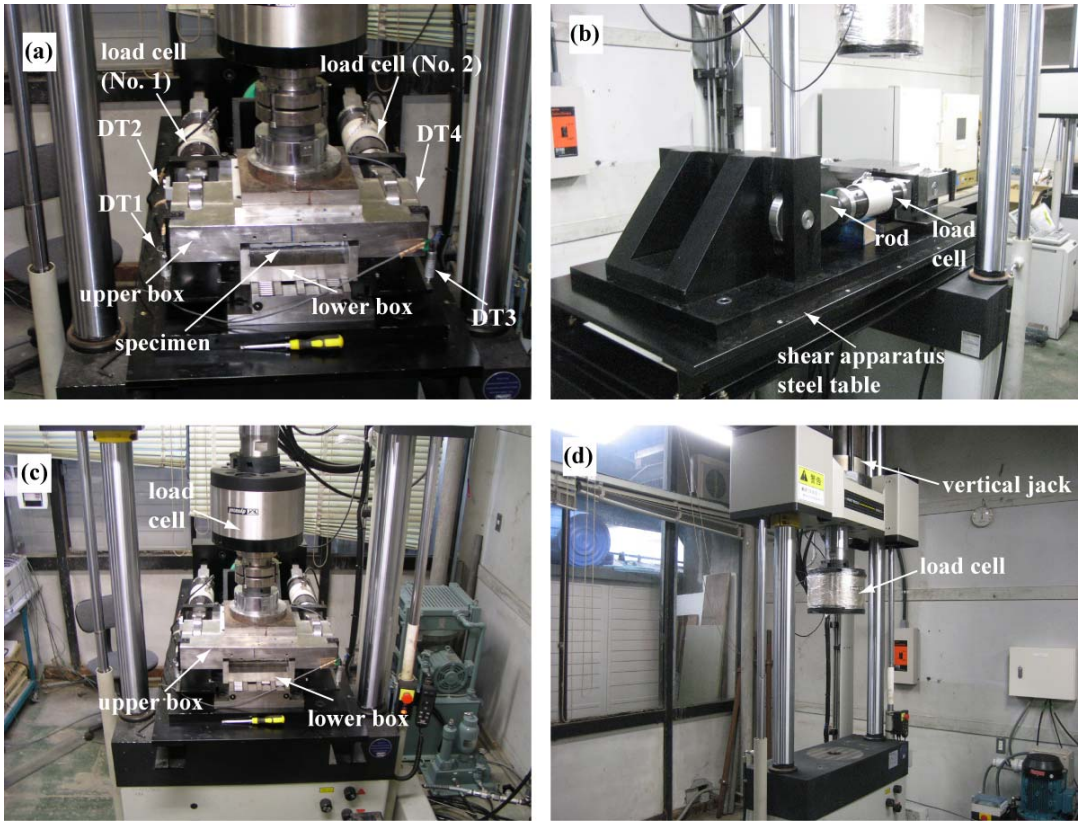

Fig. 3.2. Photographs of the direct shear teat apparatus for (a) shear box, (b) side view, (c) front view and (d) normal load apparatus.

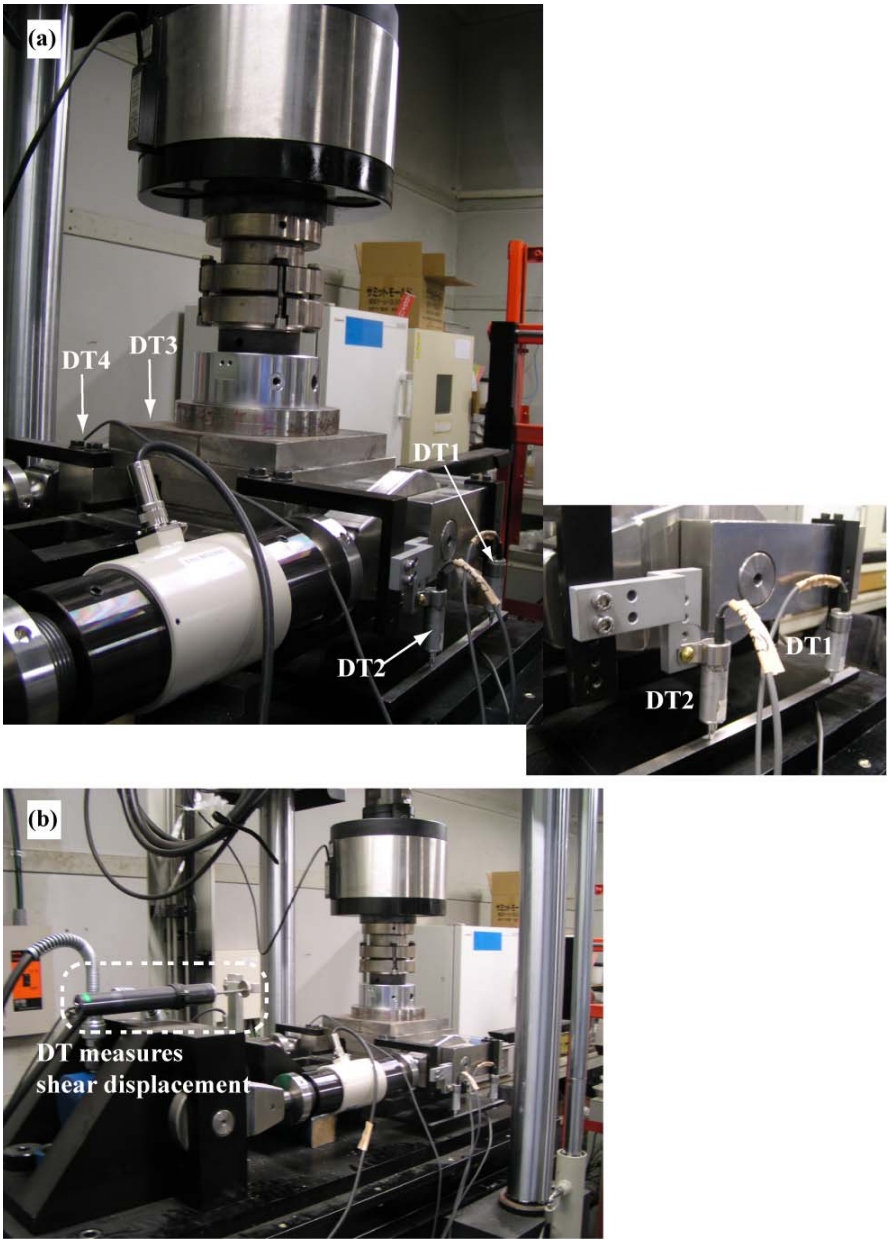

Fig. 3.3. Photographs of the displacement transducers for measuring (a) normal deformation and (b) shear displacement during shearing process.

3.2 Experimental methodology

3.2.1 Specimens

Two types of fractured specimens were used in the experiment. One is a tensile fracture in granite and the other is a mortar replica that reproduces the tensile fractures created in granite. The advantage of using replica is that it makes it possible to independently study the effects of two parameters that most strongly influence the shear behavior; normal stress and the fracture surface topography. Using replicas of the same fracture, the influence of only normal stress on damage evolution can be investigated without having the effect of individual difference among real fractures. Thus, to investigate the effect of normal stress, mortar replicas were used in chapter 5, while a tensile fracture created in granite was used for only normal stress of 10 MPa in chapter 4. For both granite specimens and mortar replicas specimens, three different fracture sizes ranging from 100 × 100 mm to 200 × 200 mm were used. The method for creating fractures for both granite and replica is described below.

3.2.1.1 Preparation of granite specimens

A large block of Inada granite (quarried in Ibaraki Prefecture, Japan) with a size of 385 mm × 385 mm × 200 mm ($L \times W \times H$) was used. Within this size, a short tensile fracture, which did not penetrate the whole block, was created by indenting number of steel wedges along the center height of the side planes of the block (Fig. 3.4(a)). For the sake of determining the aperture distribution by measuring the heights of each fracture surfaces, the following method was utilized to prepare the specimens:

1) First of all, the block height was cut to 80 mm to have a size of L (385 mm) × W (385 mm) × H (80 mm) as shown in Fig. 3. 4 (b). After that, the rail guides and bars (Fig. 3.11 (a)-(b)) were glued to the side plane of the block as a set (Fig. 3. 4 (b)).
2) Then, the reference plates with sizes of 100 mm × 100 mm, 150 mm × 150 mm, and 200 mm × 200 mm were bonded to the top/bottom specimen surfaces with adhesive. Simultaneously, the reference plates with a size of 425 mm × 400 mm were fixed to the reference plates with smaller sizes from 100 mm up to 200 mm (Fig. 3. 4 (c)).
3) In order to ensure that both reference plates (425 mm × 400 mm) are parallel to each other, the height gages were fixed to the lower and upper parts of the reference plates with screws (Fig. 3.4 (c)). After the reference plates (100 × 100,

150 × 150 and 200 × 200) were completely fixed to the sample, the height gages and the largest reference plates were removed, and the wedges were indented again to extend the fracture to split the sample into halves. Finally, the block was cut into the desire sizes of 100 mm × 100 mm, 150 mm × 150 mm and 200 mm × 200 mm with their reference plates (Fig. 3.9 (f)).

4) The centralizers were used just before installing the cap holders to ensure that both caps holders of the upper and lower surfaces are in the same line (Fig. 3.4 (g)). During each surface heights measurement, two caps with their reference points were inserted to the cap holders to obtain the same points for measuring the height of the two surfaces.

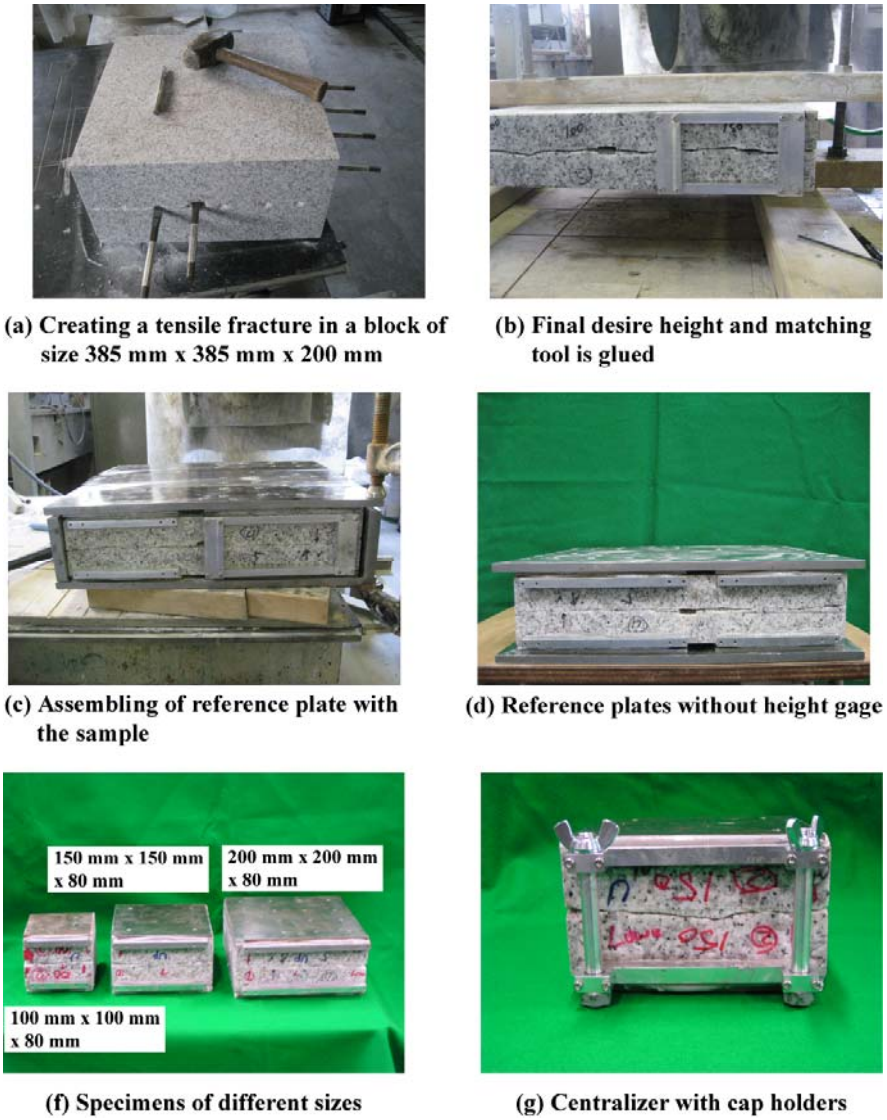

(a) Creating a tensile fracture in a block of size 385 mm x 385 mm x 200 mm

(b) Final desire height and matching tool is glued

(c) Assembling of reference plate with the sample

(d) Reference plates without height gage

(f) Specimens of different sizes

(g) Centralizer with cap holders

Fig. 3.4. Photos of reference plates with different sizes.

3.2.1.2 Preparation of mortar replicas

To study the effect of normal stress on the shear behavior in the direct shear tests, it is necessary to perform several tests on fractured specimens having the same geometrical features. However, it is impossible to find different rock with the same geometrical features in nature. Therefore, epoxy resin replicas of tensile fracture created in granite was used as the parent sample to reproduce several mortar fracture replicas.

For this propose, a large block of Inada granite with a size of 530 mm × 300 mm × 200 mm ($L \times W \times H$) was used. The method of creating the fracture and preparation procedure were the same as the one used for the previous subsection, expect No. 3 since the large fracture was not cut into smaller one (Fig. 3.5 (a) and (b)).

3.2.1.3 Epoxy resin casting

A large number of different materials for moulds have been used in the past such as two components silicon rubber [136], sand-epoxy silicon [11] and high fidelity polymer model (HFPM) [137]. In this study, based on past test-experience at Matsuki laboratory, epoxy resin (crystal resin II super-clear) has been used as shown in Fig. 3.5 (c). The epoxy resin has been chosen for its satisfactory reproduction of rough surfaces and its negligible shrinkage. Firstly, each fracture surface was cleaned with compressed air and placed in wooden box (Fig. 3.5 (d)), with the fracture surface upwards. Since there were some spaces between the wooden boxes and the specimen side planes, silicone rubber (silicone (R) RTV 8600) was used to fill out these spaces (Fig. 3.5 (d)). A few minutes before molding, a resin bonding prevention agent was applied on the surface of the fracture (Fig. 3.5 (f)). The epoxy resin (A) and its hardening agent (B) (Fig. 3.5 (c)) were mixed together for about 5 minutes before pouring into the wooden box. It should be noted that since appearance of bubbles on the surface of the replica was observed, although they were not too much, hair dryer was used to overcome this problem. In order to prevent the epoxy resin from being distorted by non-uniform temperature, pouring procedure of epoxy resin was divided into 10 steps, i.e., each step had a height of about 3 mm, and hence the total thickness of each epoxy replica was about 30 mm. After a month, the wooden boxes were removed. Before the epoxy replica was detached from the fracture surface, rail guides were glued on the side plane of the replica (Fig. 3.5(g)). Finally, the epoxy replica of size 530 mm × 300 mm × 60 mm ($L \times W \times H$) was cut into the desire sizes of 100 mm × 100 mm, 150 mm × 150 mm and 200 mm × 200 mm (Fig. 3.5 (h)).

3.2.1.4 Preparation of mortar fracture replica

Before making the mortar replicas, the surfaces of both the fractured rock and the obtained epoxy replicas were measured by using a laser profilometer. The obtained results showed that both the fractured rocks and the replicas have almost the same surface topography, which verified the chosen replication technique.

The material used to produce the mortar replicas is a mixture of ordinary Portland cement with silica sand No. 7. The water/cement ratio of 0.45 has been chosen among three ratios of 0.45, 0.55 and 0.50, according to the strength values. The cement and sand were mixed with water in a rotating drum mixer for 5 minutes, as shown in Fig. 3.6. The mortar was poured into the wooden box where the epoxy replicas had previously formed, as illustrated in Fig. 3.7(a) and (b). The mortar was vibrated carefully and thereafter put in the room condition. After at least 24 hours, the surrounding wooden plates were removed and the mortar replicas could easily be detached from the epoxy replica. The mortar replicas have a thickness of 80 mm, equal to granite specimens (Fig. 3.7(c)). All mortar replicas were cured in water at 40^{o}C for four days. In total, 16 mortar facture replicas were reproduced. Finally, the reference plates with sizes of 100 mm × 100 mm, 150 mm × 150 mm, and 200 mm × 200 mm were bonded to the top/bottom surfaces of the specimen with adhesive (Fig. 3.7 (d)), and height gages.

(a) Assembling of reference plates

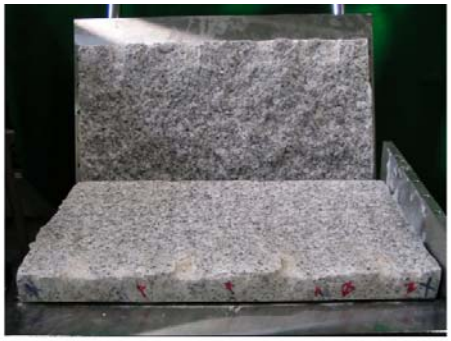

(b) Creating a tensile fracture in a block of size 530 mm x 300 mm x 200 mm

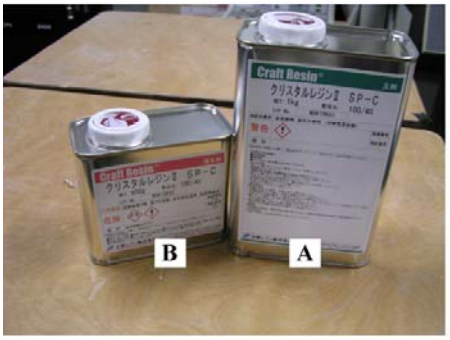

(c) Crystal resin II, super-clear

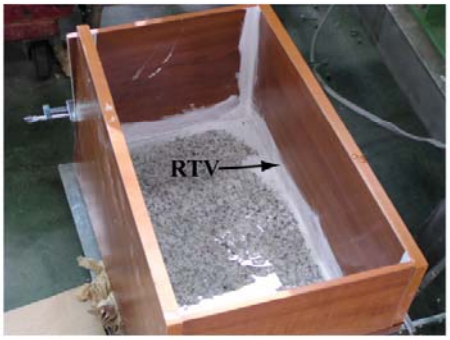

(d) Installing the wooden frame

(f) Resin bonding prevention

(g) Final desire height and matching tool is glued

(h) Epoxy replicas of different sizes

Fig. 3.5. Different stages of making the epoxy replica and its material.

Fig. 3.6. Rotating drum mixer.

(a) Epoxy replicas with wooden boxes

(b) Pouring the mortar

(c) Mortar replicas

(d) Final shape of the mortar replica

Fig. 3.7 Method for producing the mortar fracture replicas.

3.2.2 Testing method in the direct shear test

For experiments to clarify the effect of size and normal stress on the shear behavior of a fracture, fractures of sizes of 100 mm × 100 mm, 150 mm × 150 mm and 200 mm × 200 mm were utilized for the direct shear test.

In the previous studies, shear behavior of a fracture was investigated by applying monotonically increasing shear loads, and accordingly, the change in surface topography and the initial aperture as a function of shear displacement have not been addressed. Furthermore, the aperture during shear was not measured in the previous studies, and consequently the mechanism for the size effect has not yet been clear.

The size effect on the shear behavior of a tensile fracture created in granite was determined by the direct shear tests with only a normal stress of 10 MPa. Normal and shear stresses were loaded/unloaded (cyclic loading) at designated values of shear displacements, as shown in Fig. 3.8. Thus, the change in the surface topography was measured by using a profile measurement system with a laser profilometer, to determine the evolution of surface damage and aperture during shear.

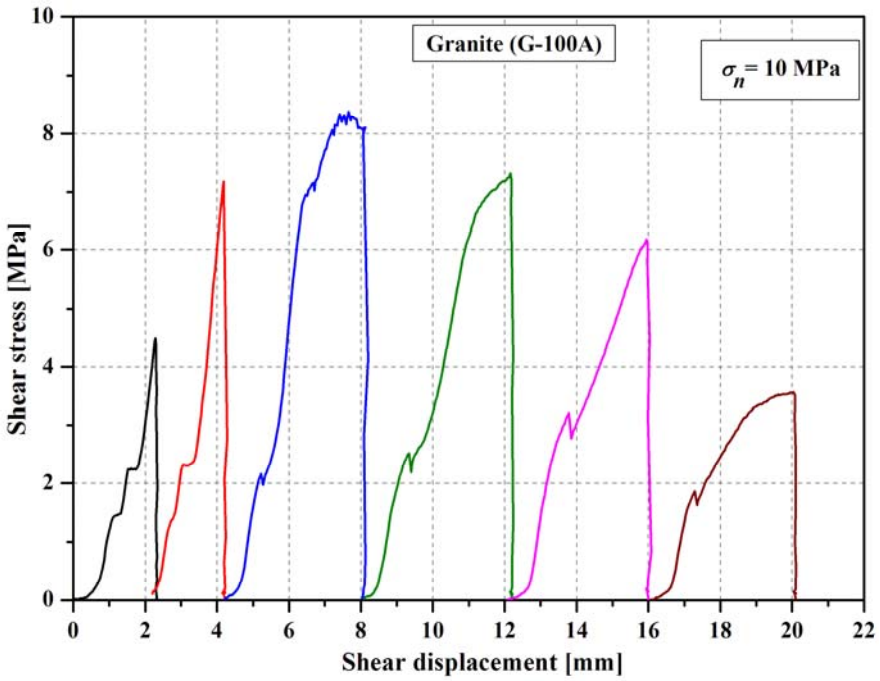

Fig. 3.8. Shear stress versus shear displacement curve for granite samples under cyclic loading condition.

For mortar replicas experiments, the effect of normal stress on the shear behavior was investigated in the direct shear tests. Measurement was done for normal stress of 0.3 and 1 MPa and shear displacements of 2 and 20 mm (monotonic loading) (Fig. 3.9). The change in the surface topography under different normal stresses was measured by using a profile measurement system with a laser profilometer to determine the evolution of surface damage and aperture during shear. Moreover, within these experiments, the effect of gouge materials on closure was investigated. After the sheared specimen was removed from the shear box, firstly, closure was measured with the presence of the gouge. Then the surfaces were cleaned from the gouge material, and the specimen was put back into the shear box and the closure was measured again for the surfaces without the gouge materials.

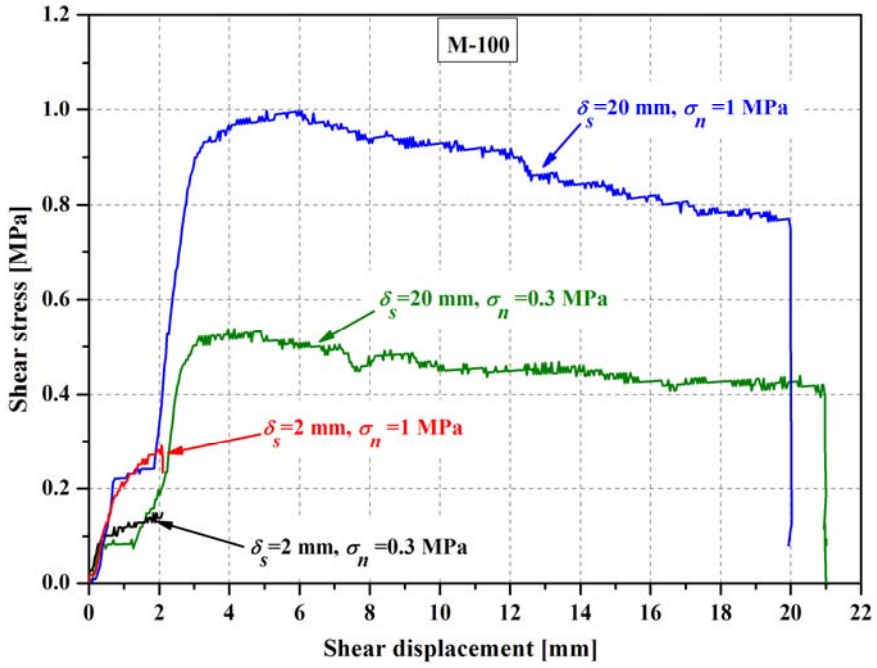

Fig. 3.9. Shear stress versus shear displacement condition applied for mortar replica.

3.3 Measurement of surface topography and determination of aperture

3.3.1 Measurement system

As mentioned previously, first, a tensile fracture with varied sizes was created in a block of granite by indenting wedges and mortar replicas were produced from the tensile fractures. Then the topographical measurements of the fracture surfaces were

carried out by using a non-contact surface measurement system to determine the aperture distribution of the fracture [18]. The laser profilometer was driven in a horizontal (*X*-*Y*) plane by a two-dimensional (2D) positioning system with two linear motor actuators, as shown in Fig. 3.10.

The system is composed of the following elements:

1) Two linear motor actuators (stroke: 1250 mm; total length: 150 mm; positional resolution: 1μm) to control *X*- and *Y*-tables.
2) Two drivers for (1).
3) A laser profilometer (measurement range: 30 mm; resolution: 3 μm).
4) An amp unit for (3).
5) A small moving table (stroke: 91.5mm) for adjusting the vertical position of (3).
6) A data measurement 16-bit A/D conversion board.
7) A pulse transmission 16-bit A/D conversion board.
8) A 24-bit pulse counters board.
9) A personal computer for controlling table motion and conducting measurements.
10) A personal computer for monitoring the position of the *Y*-table.

The main frame of the measurement system is composed of H-steel beams which measured 1720 mm × 1570 mm × 1500 mm (Width × Depth × Height). The two linear motor actuators (1) drive the *X*- and *Y*-tables along each rail. As the linear motor actuators are made from a soft aluminums alloy, they are fixed on an H-steel beam to increase their flexural rigidity. A laser profilometer (3) was screwed into the *Y*-table through a small moving table (5) which was used to adjust the initial vertical position of the laser profilometer to ensure that it would not exceed its measurement range (30 mm) during measurement of the fracture surfaces. Hence, while the *X*- and *Y*-tables are moved by the respective drivers (2), the laser profilometer moves in a nominally horizontal plane. The linear motor rails for the *X*- and *Y*-tables are equipped with the absolute origin and a linear encoder gage so that the position of the laser profilometer from the absolute origin can be specified in 1 μm increments by the encoder attached to each table.

The personal computer (9) controls the movement of the two axial tables, and reads measurement data from laser profilometer (3) through the A/D conversion board (6). Moreover, the personal computer (10) reads the position information from the encoder mounted on the *Y*-table through the pulse counter board (8) and monitors the position of the table (Fig. 3.10) [18].

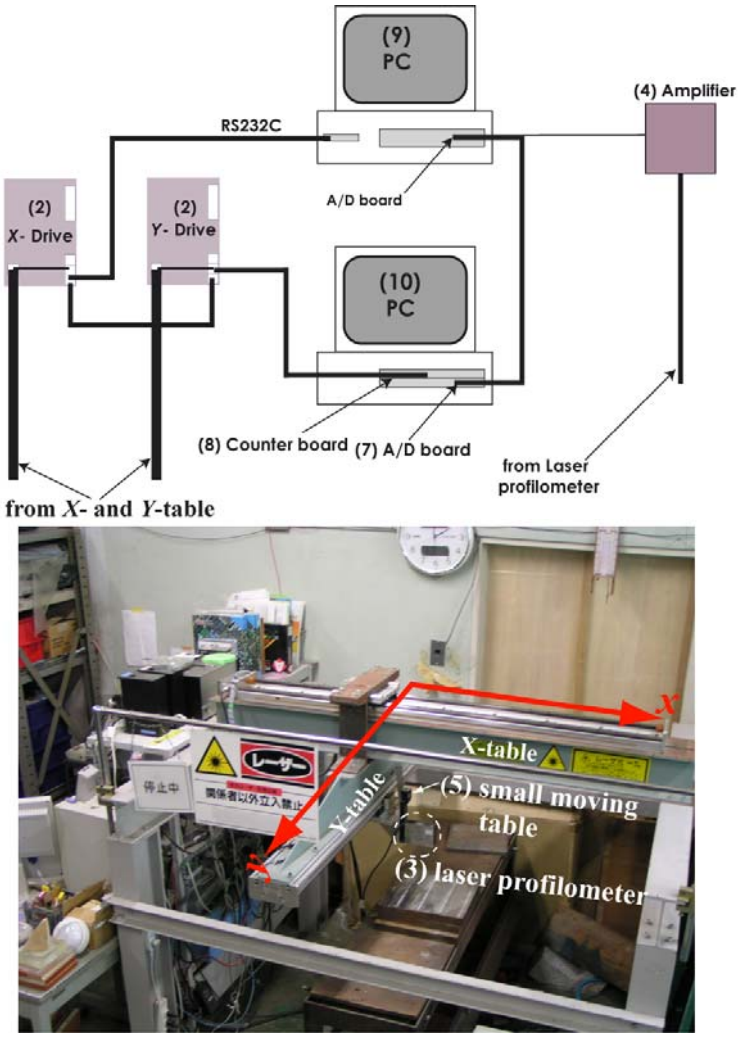

Fig. 310. System used to measure surface heights of a fracture using a laser profilometer.

3.3.2 Measurement method of surface height

In order to determine the aperture distribution of the granite/replica (before and after the shearing), it is needed to measure the heights of each fracture surfaces at the same positions along matching path for all measurement lines. To accomplish this, specific tools were developed and fixed into the top/bottom surfaces of the specimen to avoid any error in the measurement. These tools are shown in Fig. 3.11 and Fig. 3.12 and are as follows:

1) Matching tools consist of two bars (Fig. 3.11(a)), rail guides (Fig. 3.11(b)), centralizers (Fig. 3.11(c)), cap holders and caps with a reference point (Fig. 3.11(d)). These tools were prepared for each size of the fracture.
2) Reference steel plates with different sizes ranging from 100 mm × 100 mm up to 425 mm × 400 mm were utilized (Fig 3.12(a)).
3) Finally, height gages were fixed to the upper and lower parts of the reference plates of size 425 mm × 400 mm with screws (Fig 3.12(b)).

(a) Bars

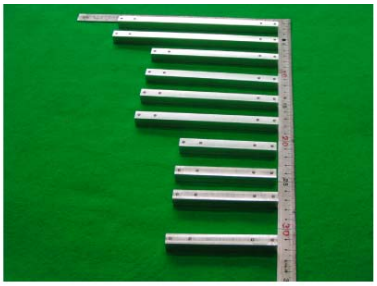

(b) Rail guide

(c) Centralizer

(d) Cap holders with caps

Fig. 3.11. Photos of matching tools.

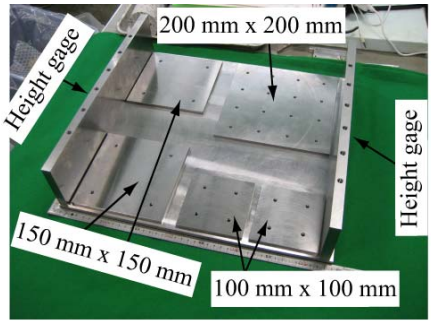

(a) Reference plates with all small portions

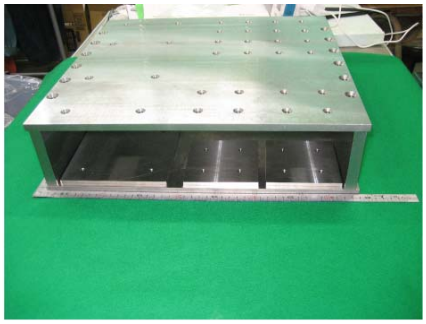

(b) Assembling of reference plates

Fig. 3.12. Photos of reference plates with different sizes.

Before the measurement starts, the sample was placed on a steel table and the position of the surface was adjusted so that the straight line connecting the two reference points and the axis of the *Y*-table were parallel to each other (Fig. 3.13 (a)), and the spot location where the laser hit one of the reference points was recorded. Accordingly, by choosing the same position of the first measurement point in the first measurement line for the two fracture surfaces, matching of the measurement points into measurement lines was ensured since the reference points are common to the two surfaces. In addition, since we had the effects of wedge indentation on the fracture surfaces near the side planes of the sample, the aperture distributions have been determined excluding areas subjecting to these effects (Fig. 3.13 (b)). For each sample, the time required to measure the whole area was about 10 hours.

Before performing the automatic scanning of a fracture surface, a target area on the fracture surface as well as the interval must be defined. The scanning program allows the users to input some parameters to select a scanning region on the fracture surfaces and define an interval (mesh interval), and then the laser profilometer will automatically measure the target points within the selected area at a constant interval. In this study, the scanning program JAVA was used. To select a scanning area, four parameters (points); *Y*-start point, *Y*-length, *X*-start point, and *X*-length of an area were measured to use them as input data. The mesh interval used throughout this study was 0.1 mm for all fracture sizes.

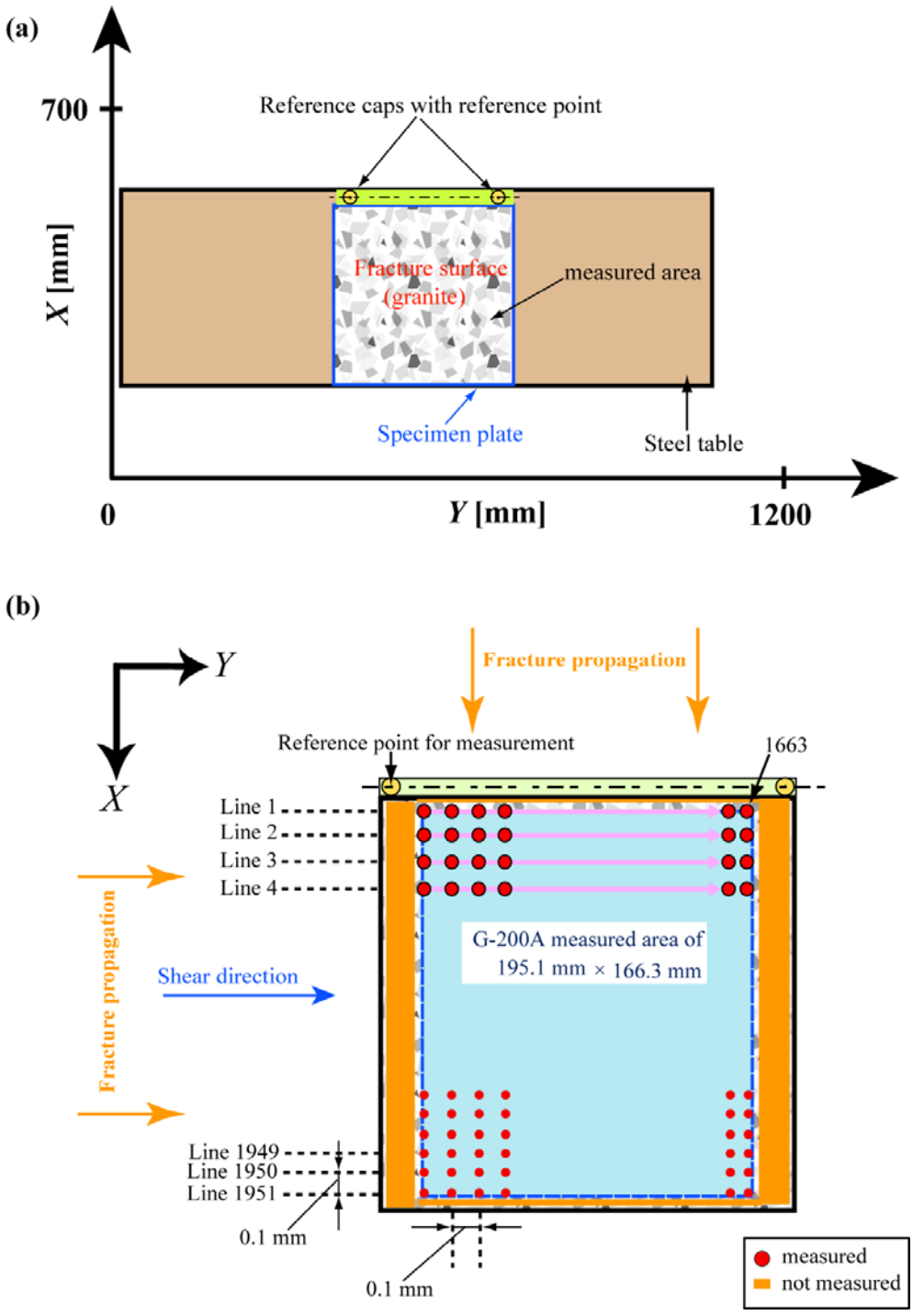

Fig. 3.13. Schematic of the measurement method for (a) adjusting the position of the specimen on the steel table, and (b) measurement lines/points and the excluded area.

3.3.3 Correction of the measurement data

3.3.3.1 Distortion correction by means of level surface measurements

The measurement data contained a complex set of distortion components that represented a combination of the following factors: the main frame of the measurement system was not mounted on a completely level surface and the rail of the *Y*-axis tilted to some extent as the *Y*-table moved. To remove these distortion components, I measured the water surface as a perfectly level surface, and determined the amount of correction needed to obtain a level surface. A level surface was prepared by placing a tub filled with water and uniformly spraying lacquer paint onto the water surface to create a film of lacquer, since the surface of clear water, which permits laser transmission, cannot be measured with a laser. Lacquer-surface measurements were conducted over an area that sufficiently covered the measurement area of the fracture surface, as shown in Fig. 3.14. Thus, the quantity obtained by subtracting the correction amount from the measured data on a fracture surface provides data on the height from the level surface. A functional approximation using a third-order curved surface equation in terms of x and y was performed on the measured correction data as illustrated in Fig. 3.15. The height data were corrected at each position based on this curved surface.

3.3.3.2 Correcting for inclination of the specimen

The bottom surfaces of the specimens were bonded to the reference steel plates which were parallel to each other. However, the steel table on which the specimens were mounted (Fig. 3.6 and Fig. 3.13 (a)) was more or less inclined from the level surface and therefore the inclination of the reference steel plate differed between the two specimens. To correct the effect of the different inclinations, an aluminium rod was placed at four points in the corners of the reference steel plate for each fracture surface, and the inclination of the reference steel plate was determined by measuring the heights of the rods for a 90 × 90 mm area in the center of the end surface (Fig. 3.14 (b)). After the average height determined at the four points was corrected by using the correction amount that was determined in the previous step, the 3D inclination of each reference steel plate was removed from the measured data for each fracture surface.

3.3.3.3 Correcting for the orthogonality of the X- and Y-axes

After performing the corrections described above, the matching of two fracture surfaces was examined. The result indicated the presence of a slight shift due to the fact that the *X*- and *Y*-axes were not exactly orthogonal. Since measurement in the

X-direction is performed in opposite directions for the two fracture surfaces, the deviation in the orthogonality affects the matching of the measurement points. Therefore, the extent of shift was determined by shifting the measurement points by 0.1 mm increments in the *Y*-direction so that the standard deviation of the aperture in each line could be minimized.

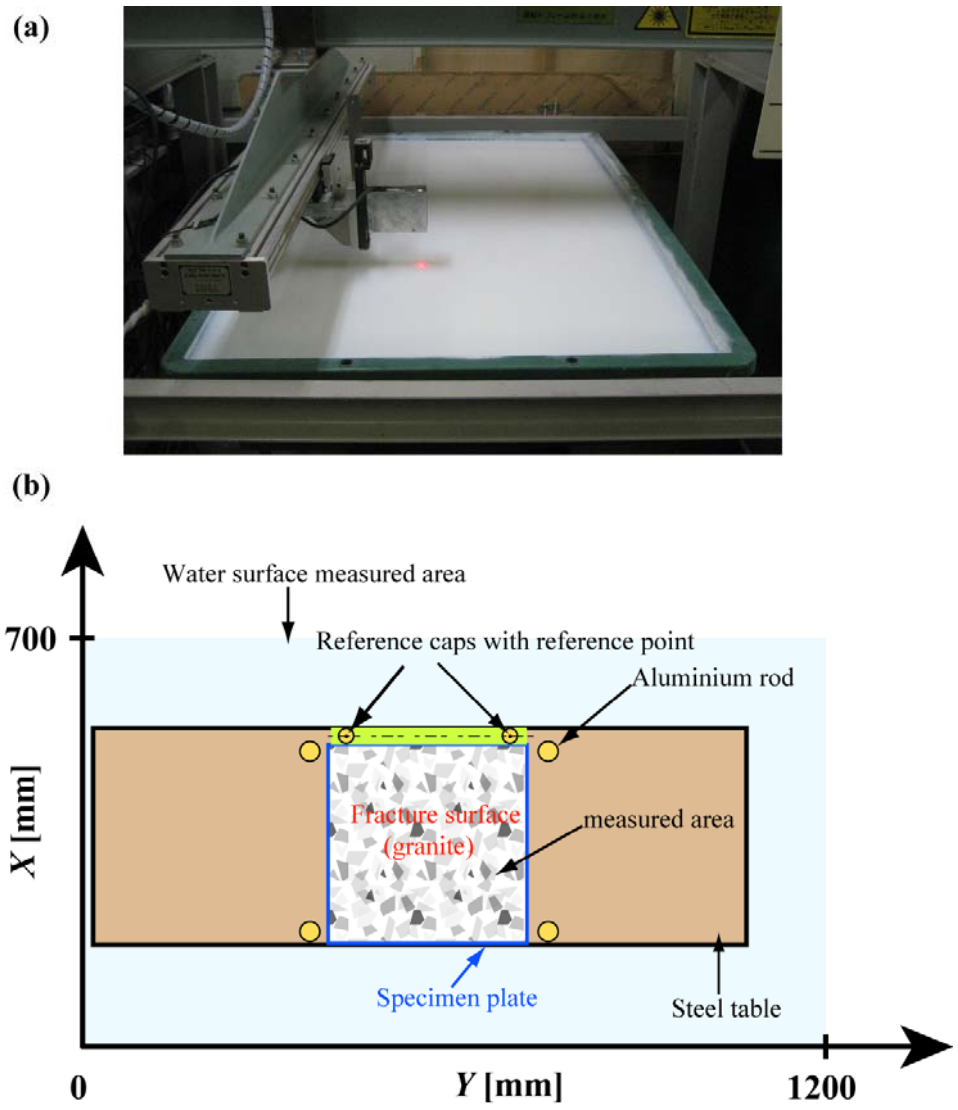

Fig. 3.14. Water surface measurement.

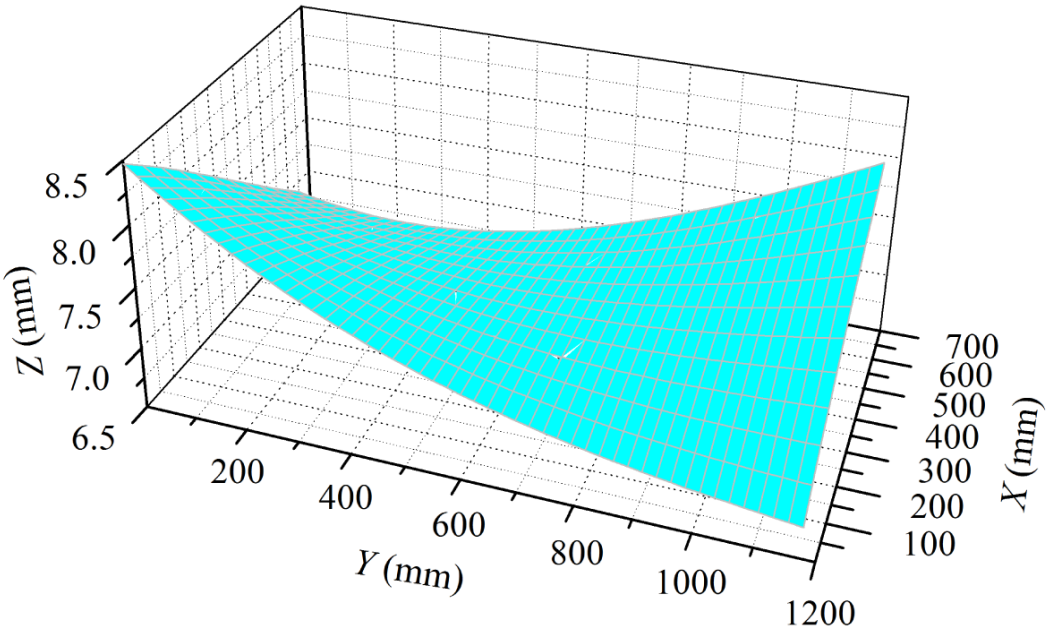

$$Z=A_0X+A_1Y+A_2X^2+A_3XY+A_4Y^2+A_5X^3+A_6X^2Y+A_7XY^2+A_8Y^3+C_0$$

A_0 =-2.154545038035748x10^{3}	A_1= -3.188000289422331*10^{-3}
A_2 =-9.770721497622363x10^{7}	A_3 = 3.828483897921957*10^{6}
A_4= 2.072413358185131x10^{6}	A_5 = 8.945771274835621*10^{10}
A_6 = -5.808966618697057x10^{10}	A_7 = 2.523480184483868*10^{10}
A_8 =-5.161746626473331x10^{-10}	C_0 = 8.47285980974059

Fig. 3.15. A 3D graph of water surface measurement and its equation for correction.

3.3.4 Determination of initial aperture distribution

The aperture distributions of both granite and mortar replicas were determined for each specimen. In this study, the aperture produced by the surfaces that are in contact at a single point is called the initial aperture, as described previously. The initial aperture value was determined by summing the height of each surface, and by shifting the value so that the minimum value was zero. The calculation formula is:

$$e(x,y) = z_2(x,y) + z_1(x,y) - h\,, \tag{3.1}$$

where $z_2(x,y)$ and $z_1(x,y)$ are two digital data for surface height at (x,y) and h is a shifting value, which gives a minimum value equal to zero.

3.4 Summary

In this chapter, the development of the DST, the measurement devices and the surface height measuring technique were mainly described. At the beginning, a compact direct shear test apparatus with a dimension of 130 cm × 60 cm and a capacity of 500 kN was designed and constructed. Then, a decision was made to use two kinds of fractured samples; i.e., granite specimens and mortar replicas specimens. The advantage of using replicas is that it makes it possible to study only the influence of normal stress on the shear behavior for the same surface topography, excluding the effect of individual difference. Thus, a method for making specimens of mortar replicas that reproduce a tensile fracture in granite has been developed. Two different experimental methods were planned to perform:

1) Cyclic loading test for granite specimens: Normal and shear loads are loaded and unloaded at designated shear displacements with normal stress of 10 MPa. Thus, in addition to the size effect on the shear behavior, the evolution of surface damage is estimated by measuring the surface topography before and after shearing.
2) Monotonic tests for mortar replicas with normal stresses of 0.3 and 1 MPa and shear displacements of 2 and 20 mm: In this experiment, the effects of both normal stress and gouge materials on shear behavior are investigated. The evolution of surface damage under two different normal stresses is estimated by measuring the surface topography before and after shearing. Moreover, the effect of gouge materials on closure may be clarified.

4. SIZE EFFECT ON SHEAR BEHAVIOR OF A FRACTURE IN GRANITE

To investigate the size effect on the shear behavior under constant normal stress in the DST under, Inada granite specimens (quarried in Ibaraki Prefecture, Japan) with sizes of 100 mm × 100 mm, 150 mm × 150 mm and 200 mm × 200 mm were used.

4.1 Set-up procedure for shear test

To set the initial position of the sample at the beginning of the test, the two halves of the fracture surfaces were matched together manually. As the tensile fractures were fresh, this procedure was easy to be precise enough for the purpose. For each shear test, the following produce was taken:

1) Fracture surface heights were measured before shearing,
2) Normal stress of 10 MPa was applied and kept constant,
3) Shear displacement was applied to about 20 mm at maximum with a rate of 0.5 mm/min and,
4) Shear and normal loads were unloaded and re-loaded at 2, 4, 8, 12, 16 and 20 mm of shear displacement, and the fracture surface heights were measured at each cycle. At each cycle, the followings are determined: 1) the evolution of surface damage, 2) the SD of the fracture surface heights, 3) the power spectral densities (PSDs) of the surface heights and aperture, and 4) the mean and SD of the initial aperture.

During these experiments, I tried to avoid failure along the edges of the sample due to the effect of stress concentrations and tensile stresses at the boundary [138].

4.2 Mechanical parameters of granite

4.2.1 Uniaxial compression test

The uniaxial compressive strength (UCS) was determined according to the ISRM recommendations [139] and tests were carried out for specimens of regular geometry. The specimens having a length to diameter ratio of 2.5 and a diameter of 37.27 mm were prepared by boring from a large block. The ends of the specimens were flat within 0.02 mm, ensuring that they were parallel to each other and perpendicular to the axis of the specimen so that the load could be applied uniformly. The stress rate was within the limits of 0.5-1.0 MPa/sec. Five specimens in total were tested and the average values

were calculated. Fig. 4.1 shows an example of the UCS test result (Sample No. 5). The final test results are summarized in Table 4.1.

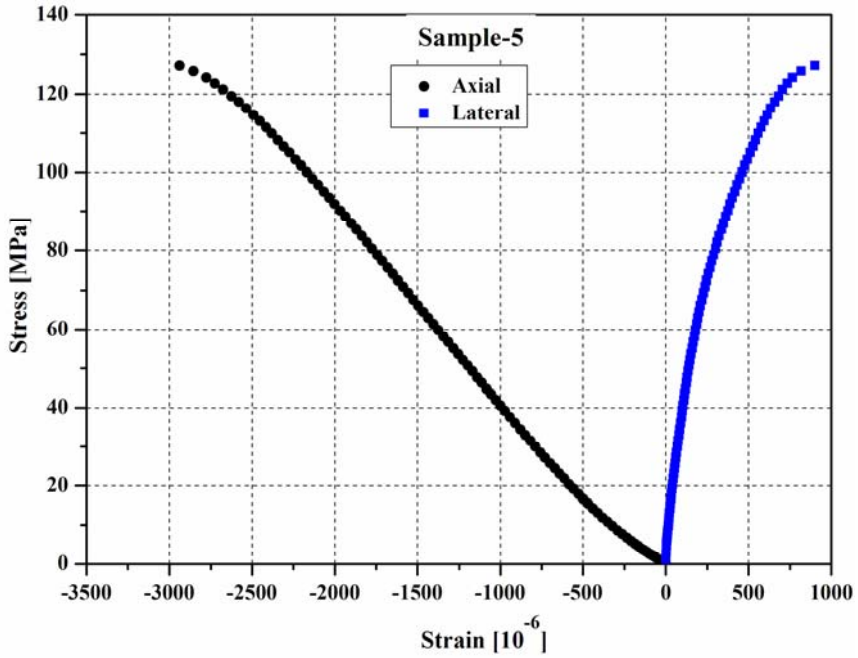

Fig. 4.1. Example of uniaxial compressive strength result.

Table 4.1. Mechanical properties of Inada granite.

Specimens	Young's modulus E_{50} (GPa)	Poisson's ratio ν	UCS σ_c (MPa)
No. 1	31.89	0.19	125.26
No. 2	43.10	0.22	94.93
No. 3	39.78	0.17	104.03
No. 4	51.38	0.16	138.36
No. 5	42.93	0.20	127.24
Average value	41.81	0.19	118

4.2.2 Tensile Strength

Tensile strength was estimated by the Brazilian test according to the ISRM suggestions [140]. The specimens were circular cylinders having a height to diameter

ratio of 0.5 and a diameter of 66 mm, prepared by boring from a large block. The ends of the specimens were smooth and flat. The diameters of the test specimens were measured in two directions and averaged. Compressive load was applied continuously to the specimens at a constant stress rate of 0.5-1.0 MPa/sec. Finally, the tensile strength of the specimens (σ_t) was calculated by the following formula:

$$\sigma_t = \frac{2P_{\max}}{\pi \times L \times D}, \tag{4.1}$$

where $P_{\max}$ is the load at failure (maximum load applied to the specimen), L is the length of the test specimen and D is the diameter of the test specimen.

Fig. 4.2 illustrates an example of the result (Sample No.4), and Table 4.2 shows the final results of five samples with the average value.

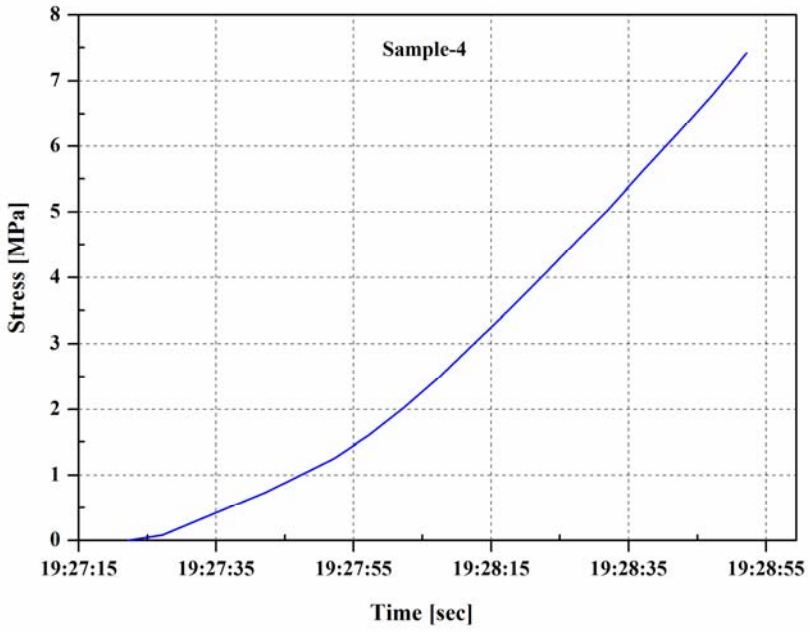

Fig. 4.2. Example of tensile strength test result.

Table 4.2. Tensile strength test results.

Specimen	Tensile strength (MPa)
No. 1	7.77
No. 2	6.59
No. 3	7.31
No. 4	7.13
No. 5	4.97
Average value	6.72

4.2.3 Effective porosity and bulk density

The effective porosity and bulk density of rock samples were determined using saturation and caliper techniques, as recommended by ISRM [141]. Samples were saturated by water immersion for a period of 48 hours with periodic agitation to remove trapped air. Later, the samples were placed in a basket in an immersion bath and their saturated-submerged weights were measured with an electronic balance. Then, the surface of the samples was dried with a moist cloth and their saturated-surface-dry weights (W) were measured in air. The bulk volume (V_B) was found from the difference between the saturated-surface-dry weight and saturated-submerged weight. The dry weight of the samples (W_d) was determined after oven drying at a temperature of 105^{o}C for a period of about 24 h. The effective pore volume (V_p) was determined from the difference between the saturated-surface-dry weight (W) and dry sample weight (W_d) by using the following formula:

$$V_p = (W - W_d)/ \rho_w, \tag{4.2}$$

where W is the saturated-surface-dry weight, W_d is dry weight of the sample, and ρ_w is weight of unit volume of water.

The bulk density of the samples (ρ) was calculated by dividing the dry mass of samples (M_d) by the bulk volume (V_B) as:

$$\rho = M_d/V_B. \tag{4.3}$$

Finally, the effective porosity (ϕ) in percent was found by determining the ratio of pore volume (V_p) to the bulk sample volume (V_B):

$$\phi = (V_p/V_B) \times 100. \quad (4.4)$$

Table 4.3 shows the porosity and density of the rock specimen.

Table 4.3. Porosity and density results.

Porosity (%)	Dry density (g/cm^3)
0.5	2.6

4.3 Effect of size and shear displacement on surfaces and aperture

The size effect on the shear behavior of a tensile fracture created in granite was determined by conducting the direct shear tests with normal stress of 10 MPa for different specimen sizes. In total, six specimens (two specimens for each size) of sizes 200 × 200 × 80 mm, 150 × 150 × 80 mm and 100 × 100 × 80 mm, which are called G200A, G200B, G150A, G150B, G100A and G100B, were used. Fig. 4.3 to Fig 4.8 show the shear stress (τ)- shear displacement (δ_n) curve and the normal displacement (δ_n)- shear displacement (δ_s) curve that were obtained at each cyclic loading for all specimens. It should be noted that some of the samples were broken during shearing at shear displacement of about 16 mm, and accordingly their surface topography measurement was not performed. The breaking of the sample was due to the effect of stress concentrations and tensile stresses at the boundary [138].

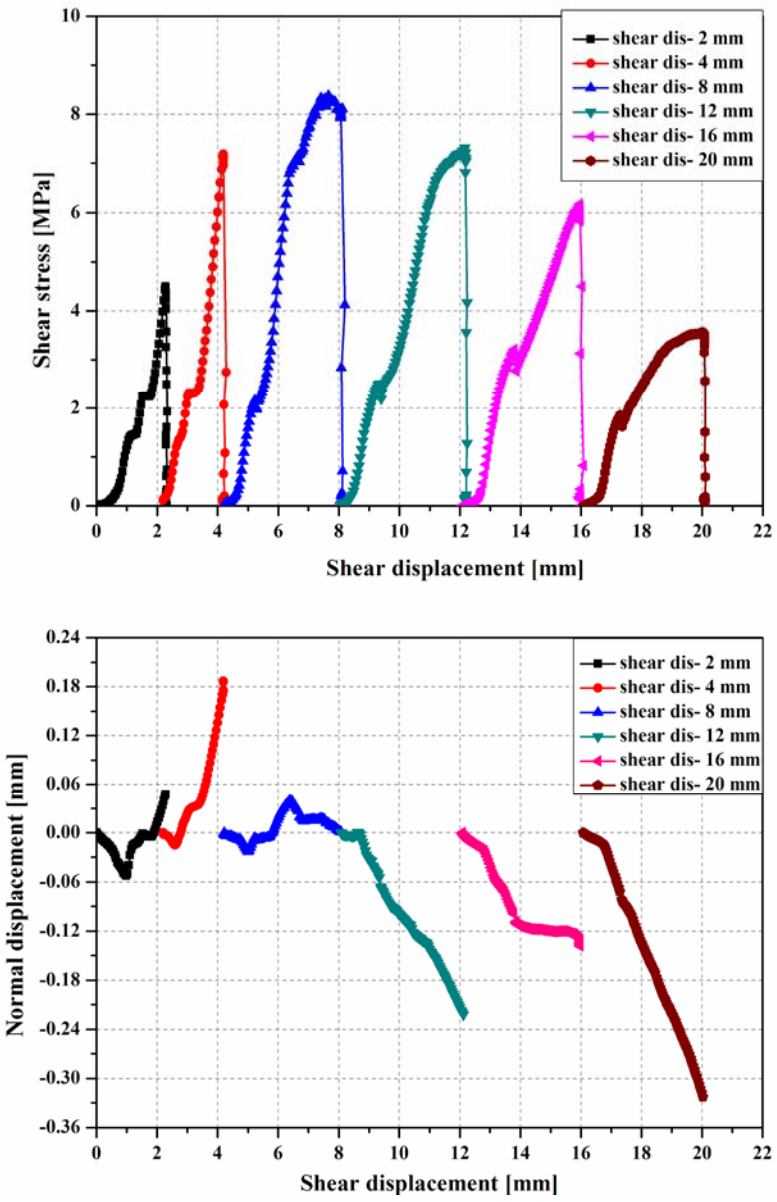

Fig. 4.3. Shear stress- shear displacement and normal displacement-shear displacement curve for G100A

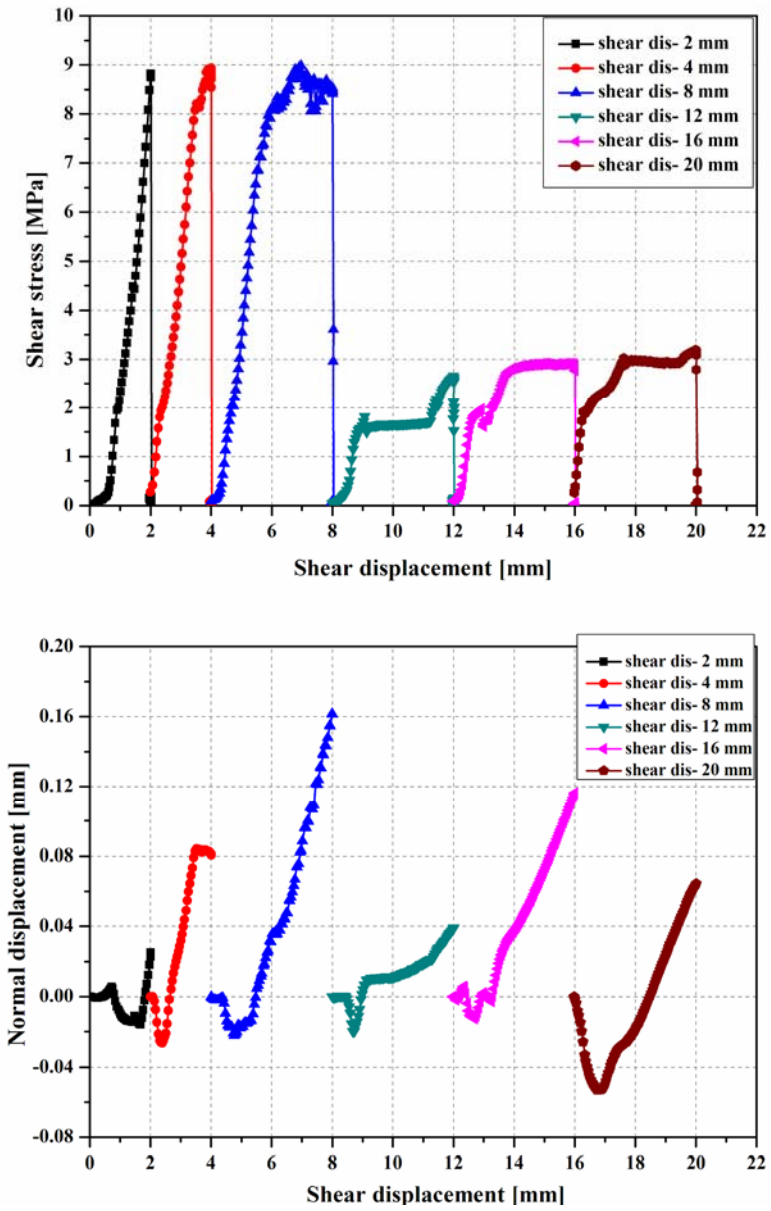

Fig. 4.4. Shear stress- shear displacement and normal displacement-shear displacement curve for G100B

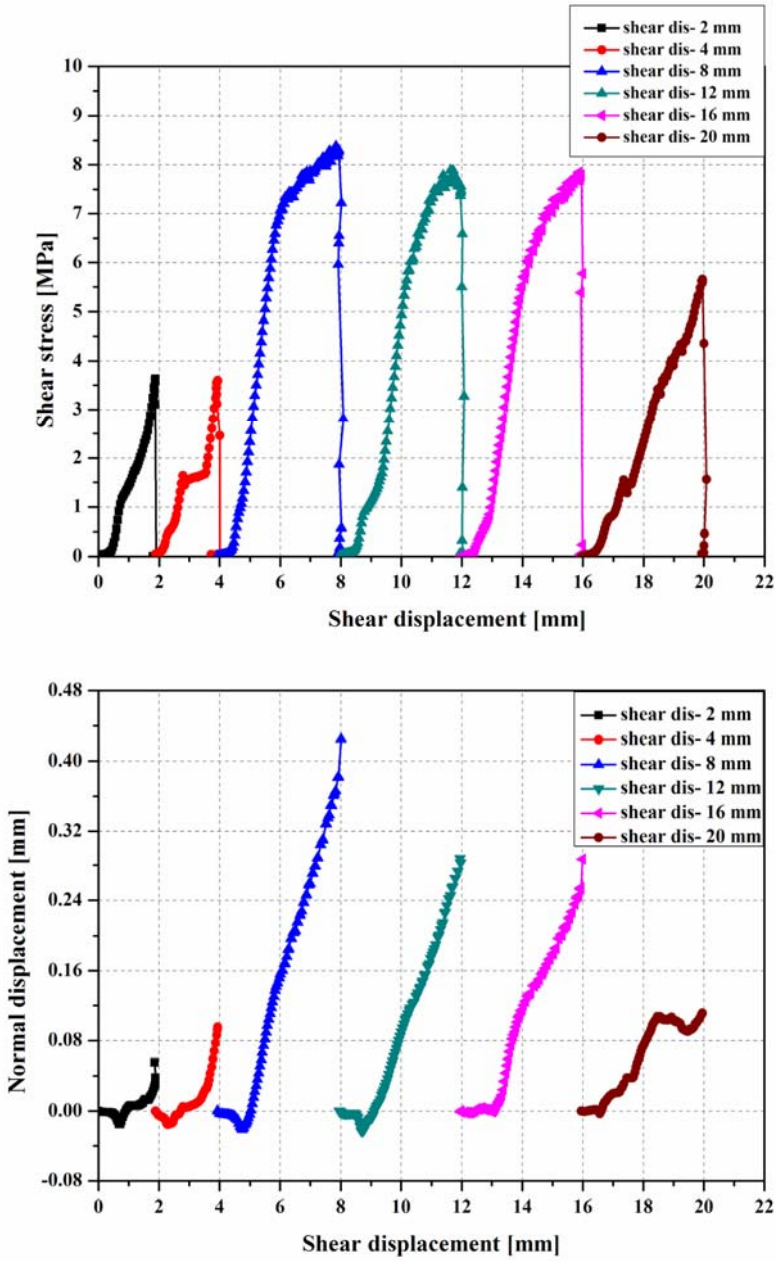

Fig. 4.5. Shear stress- shear displacement and normal displacement-shear displacement curve for G150A

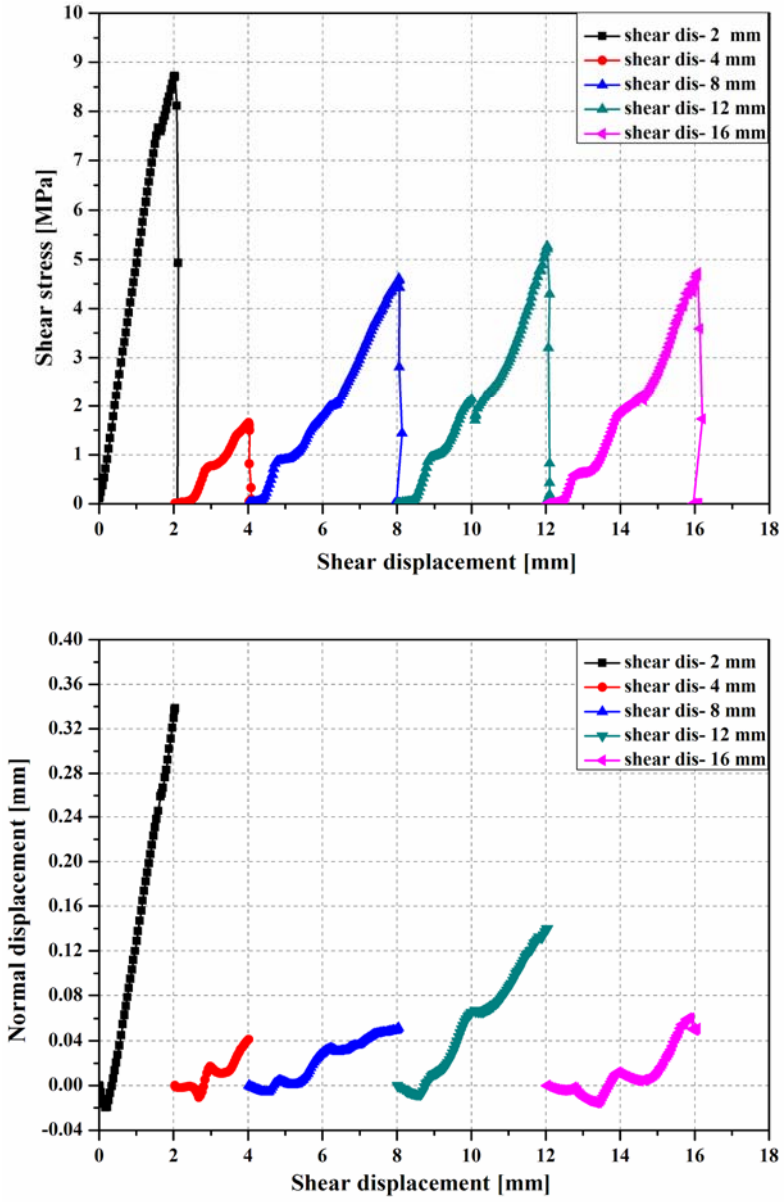

Fig. 4.6. Shear stress- shear displacement and normal displacement-shear displacement curve for G150B

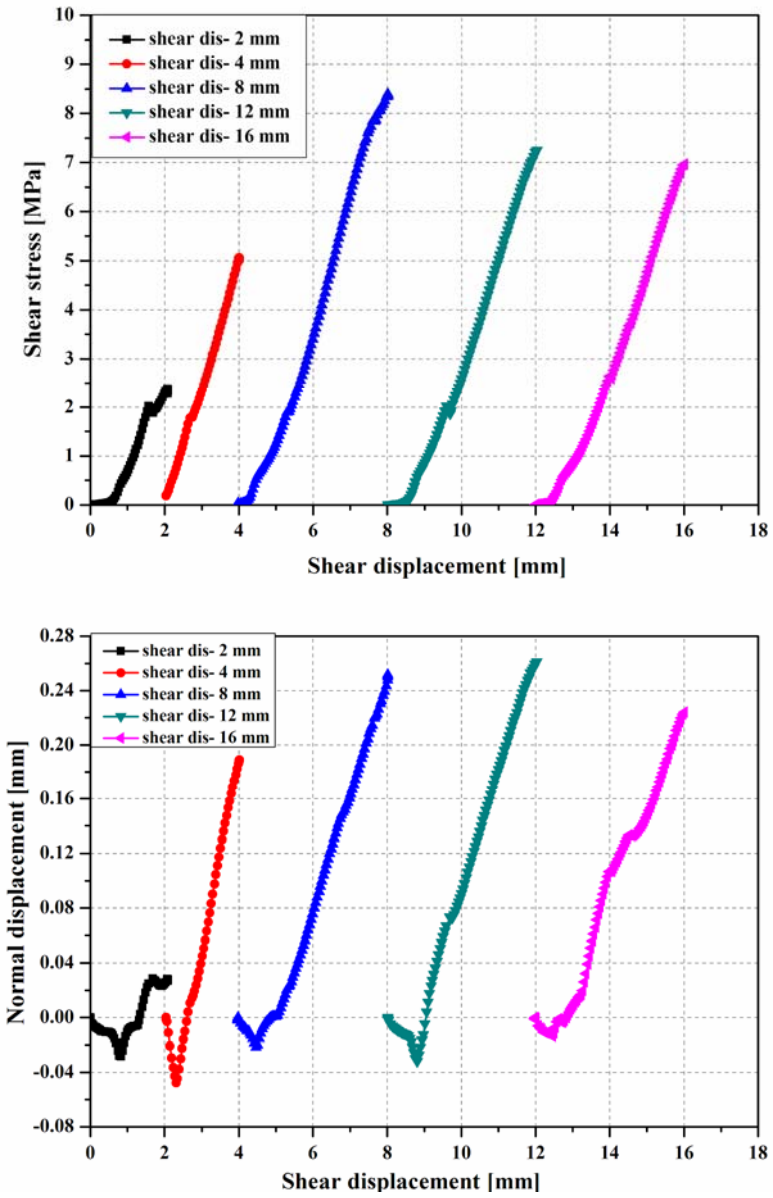

Fig. 4.7. Shear stress- shear displacement and normal displacement-shear displacement curve for G200A

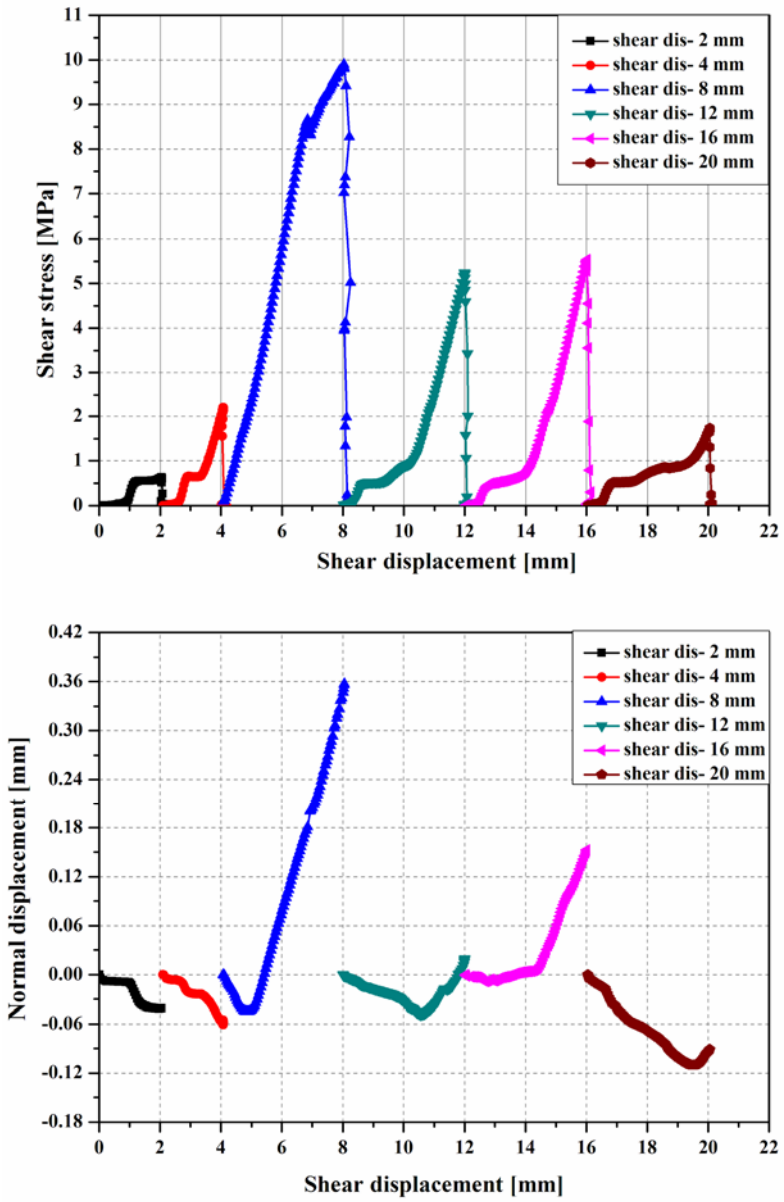

Fig. 4.8. Shear stress- shear displacement and normal displacement-shear displacement curve for G200B

4.3.1 Morphological characterization of facture surfaces

Fig. 4.9 and Fig 4.10 show examples of the upper surface height before and after shearing as contour maps for G100A and G200B, respectively. For better understanding theses two figures, examples of the PDF of the lower surface heights at different shear displacements for G150B and G200B are shown in Fig. 4.11. It can be said that the shear displacement does not have great effect on the peak value of PDF. Fig. 4.12 shows the effect of fracture size (G100A, G150A and G200B) on the PDF of the lower surface height. The peak value decreases with fracture size and the PDF becomes broader. For each fracture size, the standard deviation of the surface height was calculated and the results will be discussed later.

In order to investigate the surface damage evolution during shearing, direct measurement of the damaged area in both surfaces was performed by using pressure-sensitive film with different shear displacements of 2, 16 and 20 mm at normal stress of 10 MPa. Fig. 4.13 shows typical results for G200B. Note that the two surfaces of the fractures were at the original position without shear offset. The pressure-sensitive film (Fuji Presale Film) consists of three layers; the dye layer, the developing layer and the base layer, with a total thickness of 115 μm. The dye layer contains microcapsules that are ruptured by pressure of ≥ 10 MPa, tinting the developing layer with red of different color densities and with a spatial resolution of 100 μm, depending upon applied pressures. As can be seen in the figure, the damaged area (white zones) is gradually increased during shearing and the distribution of the damaged area is locally expanded with increasing the shear displacement.

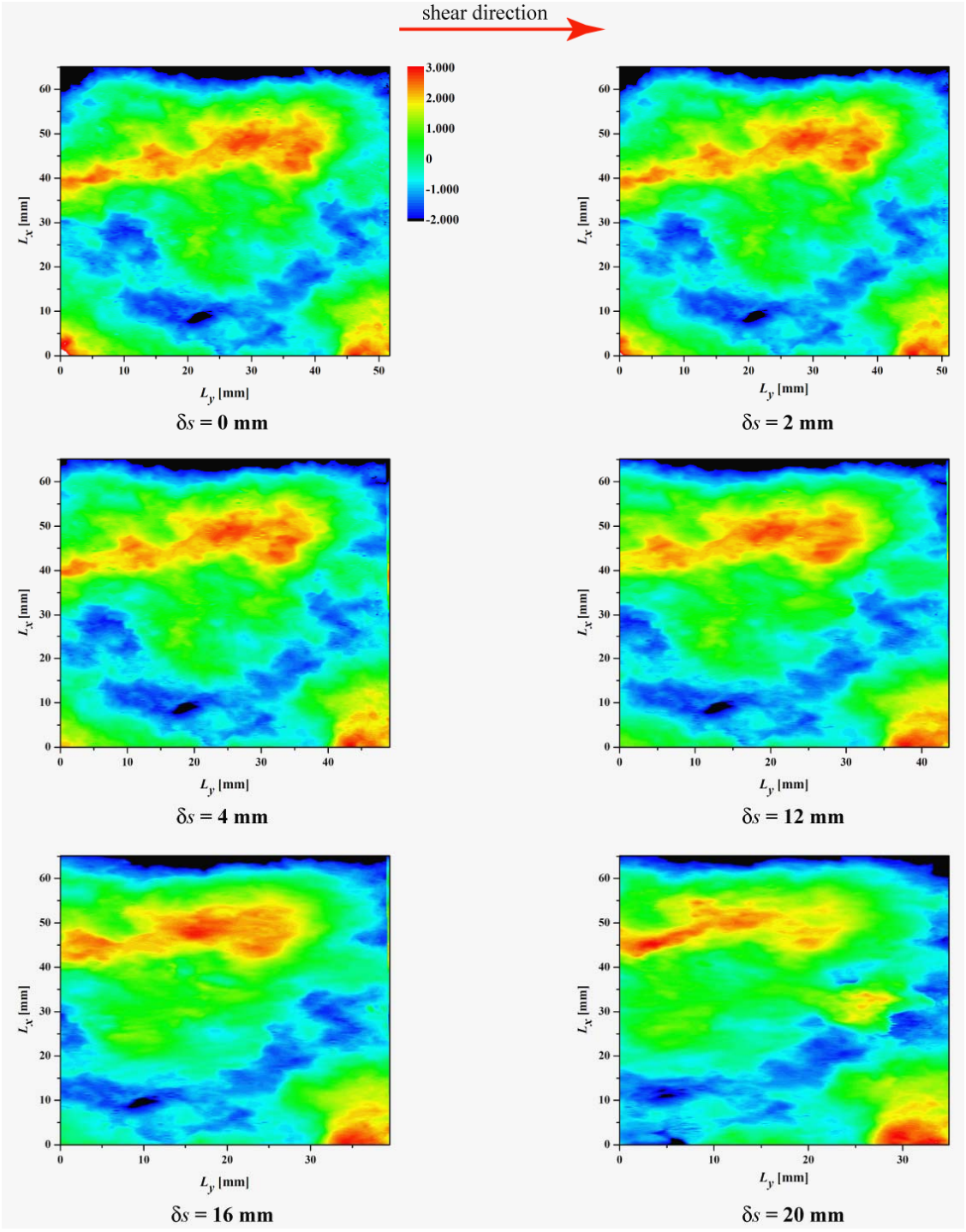

Fig. 4.9. Upper surface heights distribution before and after shearing for G100A.

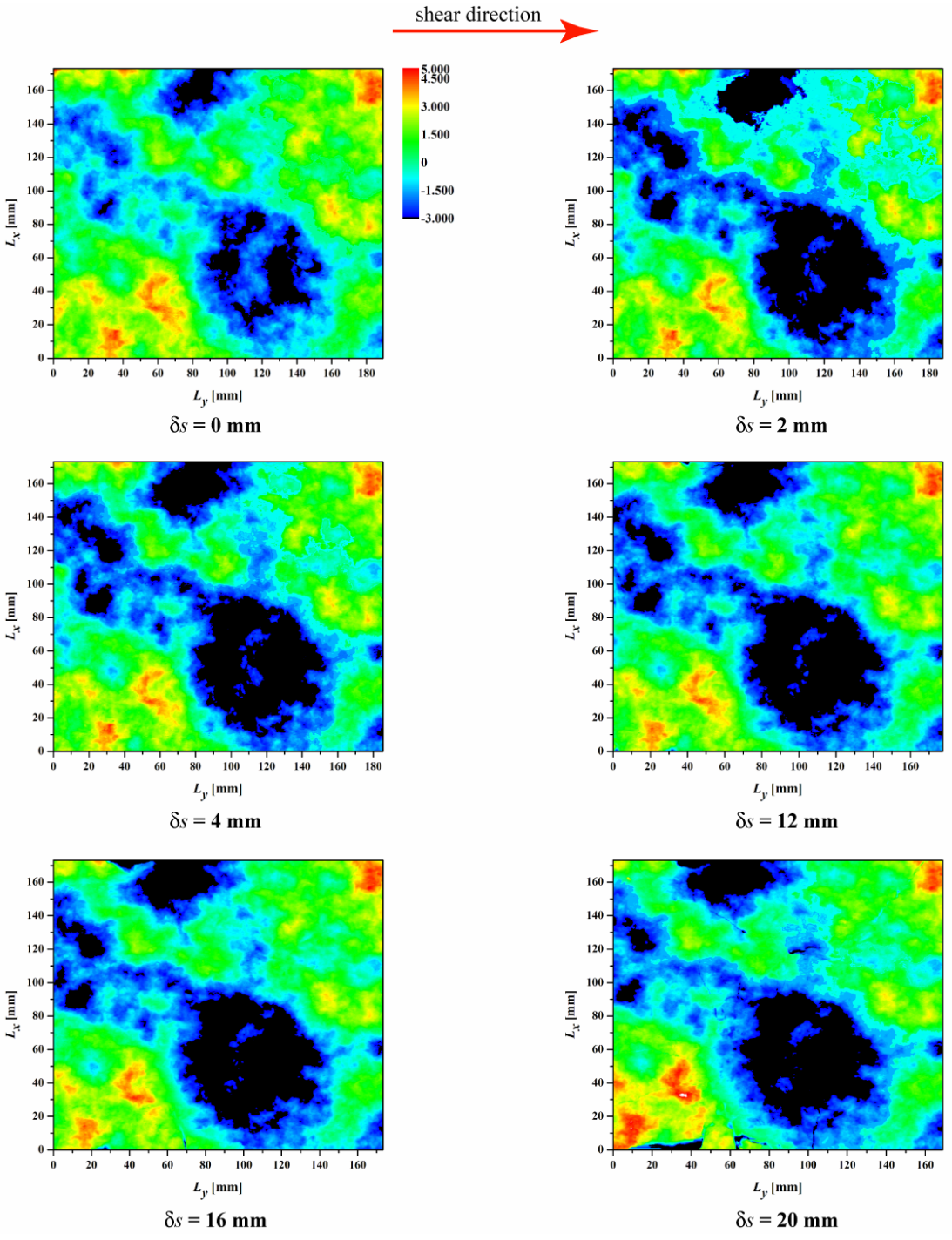

Fig. 4.10. Upper surface heights distribution before and after shearing for G200B.

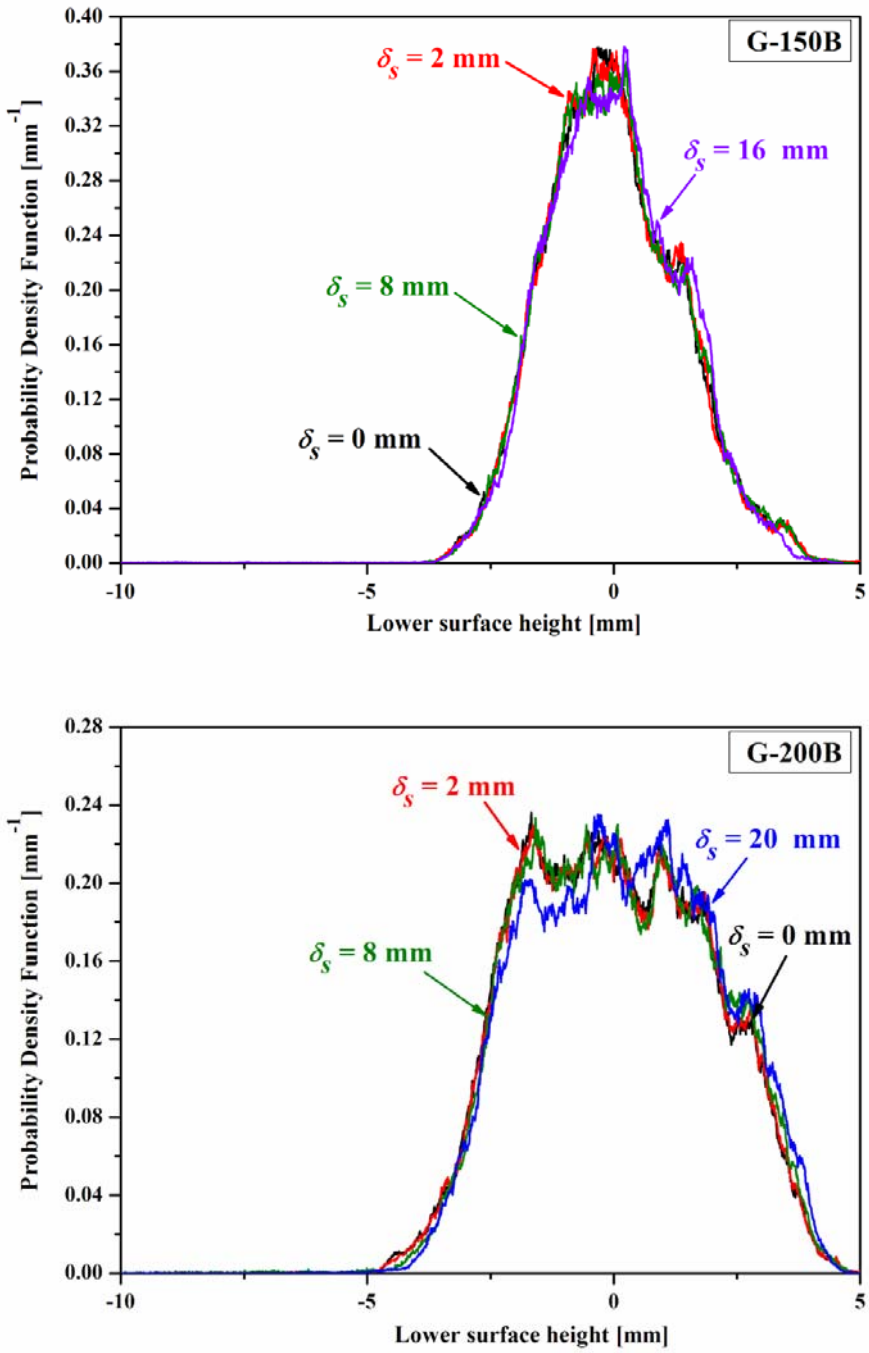

Fig. 4.11. Probability density function of the lower surface height of G150B & G200B as a function of shear displacement.

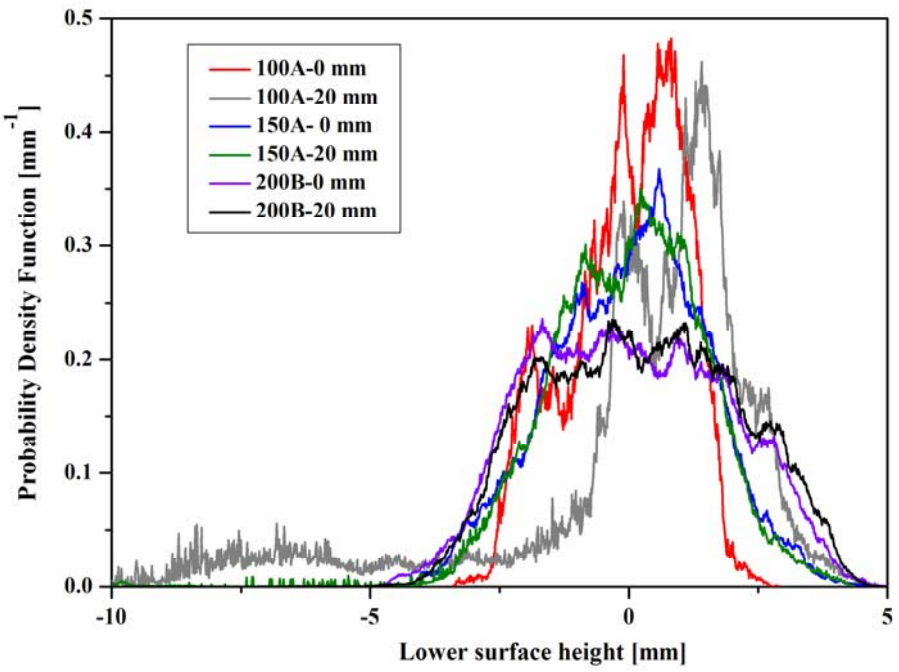

Fig. 4.12. Probability density function of the lower surface height as a function of fracture size.

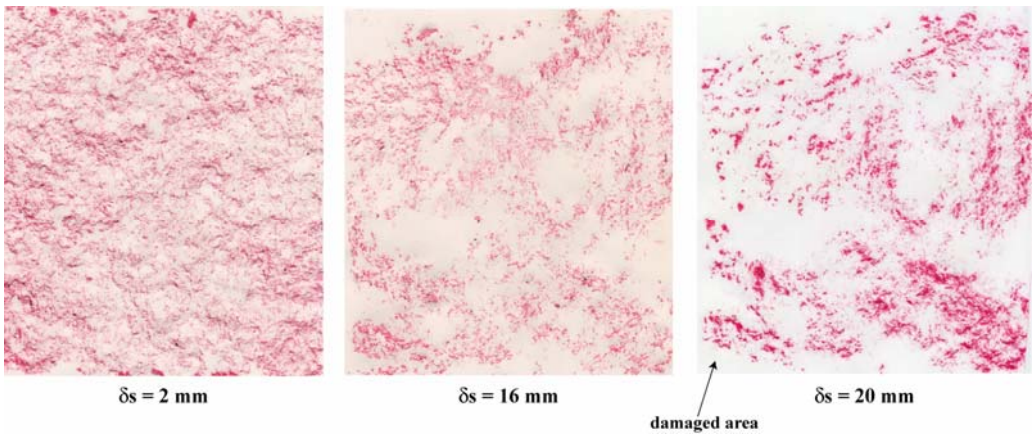

Fig. 4.13. An example of the damaged area measured by pressure-sensitive film during cyclic shear test performed for G200B at normal stress of 10 MPa.

4.3.2 Standard deviation of surface height

The fracture size effect on the SDs of the surface height for both upper (US) and lower (LS) surfaces for all shear displacements are summarized in Table 4.4 to Table 4.9. Obviously, the SD of the surface height increases with increasing the fracture size (scale-dependent behavior), while the shear displacement does not have a significant effect on the SD of the surface height. Thus, the SD of the surface height depends only on the fracture size since the surface amplitude increases with wavelength. For better understanding the effect of size on the obtained data, a relation between the average SD of the surface height and the shear displacement is shown in Fig. 4.14.

Table 4.4. Fracture size, size of measurement area and SD of the surface height of G200A.

δ_s mm	Fractured size mm	Measured area mm	SD (US) mm	SD (LS) mm
0	200 × 200 (A)	195.1 × 166.3	2.28	2.28
2		195.1 × 164.5	2.28	2.24
4		195.1 × 162.3	2.25	2.20
8		195.1 × 158.3	2.16	2.07
12		195.1 × 154.3	2.12	2.11

Table 4.5. Fracture size, size of measurement area and SD of the surface height of G200B.

δ_s mm	Fractured size mm	Measured area mm	SD (US) mm	SD (LS) mm
0	200 × 200 (B)	173.1 ×189.5	1.85	1.85
2		173.1 ×187.5	1.86	1.86
4		173.1 ×185.5	1.87	1.90
8		173.1 × 181.5	1.87	1.91
12		173.1 × 177.4	1.87	1.91
16		173.1 × 173.4	1.90	1.90
20		173.1 × 169.0	1.89	1.87

Table 4.6. Fracture size, size of measurement area and SD of the surface height of G150A.

δ_s mm	Fractured size mm	Measured area mm	SD (US) mm	SD (LS) mm
0	150 × 150 (A)	144.8 × 150	1.57	1.50
2		144.8 ×148	1.57	1.48
4		144.8 × 146	1.58	1.46
8		144.8 × 142	1.57	1.46
12		144.8 × 138	1.51	1.43
16		144.8 × 134	1.52	1.54
20		144.8 × 130	1.63	1.53

Table 4.7. Fracture size, size of measurement area and SD of the surface height of G150B.

δ_s mm	Fractured size mm	Measured area mm	SD (US) mm	SD (LS) mm
0	150 × 150 (B)	148.1 × 140.8	1.41	1.35
2		148.1 × 138.8	1.42	1.34
4		148.1 × 136.8	1.41	1.37
8		148.1 × 132.8	1.42	1.34
12		148.1 × 128.8	1.38	1.35
16		148.1 × 124.8	1.35	1.34

Table 4.8. Fracture size, size of measurement area and SD of the surface height of G100A.

δ_s mm	Fractured size mm	Measured area mm	SD (US) mm	SD (LS) mm
0	100 × 100 (A)	65.1 × 55.9	1.14	1.12
2		65.1 × 51.1	1.16	1.12
4		65.1 × 49.2	1.15	1.11
8		65.1 × 47.9	1.16	1.13
12		65.1 × 43.6	1.18	1.11
16		65.1 × 39.5	1.16	1.00
20		65.1 × 34.9	1.11	2.67

Table 4.9. Fracture size, size of measurement area and SD of the surface height of G100B.

δ_s mm	Fractured size mm	Measured area mm	SD (US) mm	SD (LS) mm
0	100 × 100 (B)	65.1 × 51.8	1.10	1.04
2		65.1 × 50.7	1.10	1.05
4		65.1 × 47.8	1.07	1.08
8		65.1 × 43.9	1.10	1.17
12		65.1 × 39.8	1.12	0.92
16		65.1 × 35.9	1.14	0.91
20		65.1 × 31.8	1.14	0.86

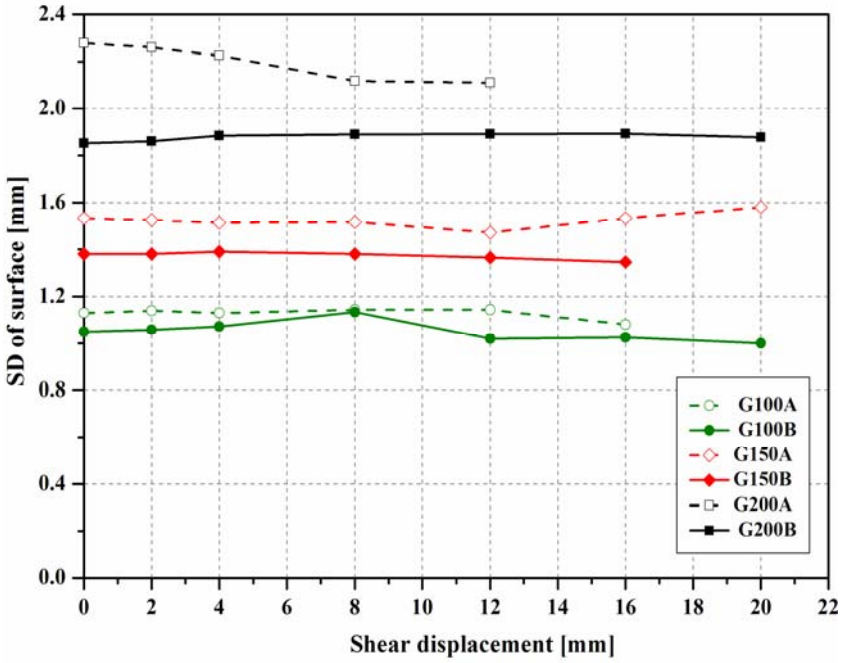

Fig. 4.14. Relation between shear displacement (δ_s) and the SD of the surface (σ_h) as a function of fracture size.

4.3.4 Mean and standard deviation of the initial aperture

The PDF of the initial aperture with different shear displacement are shown in Fig. 4.15 for G100A and G200A. The peak values of PDF decreases with shear displacement, except G100A-2 mm, and the PDF becomes broader. For each sample, the mean initial aperture and the SD of the initial aperture were determined, and summarized in Table 4.10 to Table 4.15.

To clarify the size effect during shear displacement on the initial aperture, the SDs of the initial aperture were plotted against shear displacement, as shown in Fig. 4.16. It can be seen that the SD of the initial aperture increases with both shear displacement and fracture size, and the increasing rate with respect to shear displacement tend to increase with fracture size. Thus, the correlation (matedness) between the two fracture surfaces decreases with both shear displacement and fracture size. Moreover, it can be stated that the SD of the initial aperture could be used as an index for the surface matedness. These results are in good agreement with the results obtained by Fardin [11], who clarified that the SD of the initial aperture in concrete replicas increases with fracture size during monotonic shearing test.

Fig. 4.17 shows the mean initial aperture during shear displacement versus the fracture size. Also, the mean aperture increases with fracture size as well as with shear displacement, and the increasing rates become smaller with the shear displacement. Typical examples of the initial aperture distribution for G100A and G200B are shown as contour maps in Fig. 4.18 and Fig. 4.19, respectively.

To study the changes in aperture and void space geometry with increasing shear displacement (δ_s = 0, 2 and 8 mm), direct measurement of the contact area with pressure-sensitive films (Fuji Presale Film) was performed by imposing normal stresses of 10 MPa to the fractures and the shear displacement (Fig. 4.20). The results show the contact area (isolated island) under shearing is gradually decreased and the distribution of the contact area is locally expanded with increasing the shear displacement. This result is in good agreement with the pervious studies [17, 69, 142]

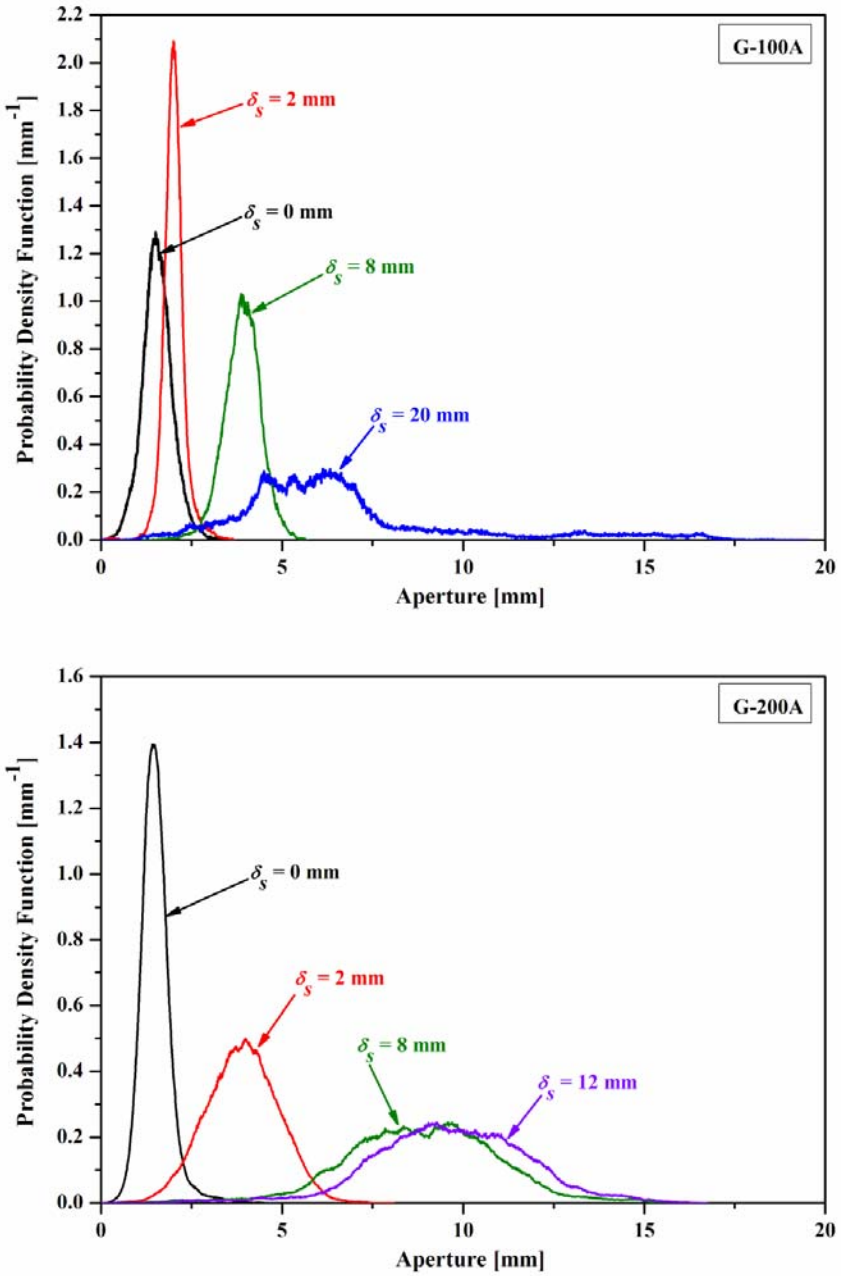

Fig. 4.15. Probability density function of the initial aperture of G100A and G200A with different shear displacement.

Table 4.10. Fracture size, size of measurement area, mean aperture and SD of the initial aperture of G200A.

δs mm	Fractured size mm	Measured area mm	Initial mean mm	SD mm
0	200 × 200 (A)	195.1 × 166.3	1.50	0.42
2		195.1 × 164.5	4.00	1.00
4		195.1 × 162.3	7.65	2.00
8		195.1 × 158.3	8.85	2.12
12		195.1 × 154.3	9.64	2.15

Table 4.11. Fracture size, size of measurement area, mean aperture and SD of the initial aperture of G200B.

δs mm	Fractured size mm	Measured area mm	Initial mean mm	SD mm
0	200 × 200 (B)	173.1 ×189.5	1.92	0.44
2		173.1 ×187.5	2.58	0.70
4		173.1 ×185.5	3.24	1.10
8		173.1 × 181.5	4.32	1.31
12		173.1 × 177.4	4.91	1.56
16		173.1 × 173.4	5.40	1.77
20		173.1 × 169.0	5.48	1.93

Table 4.12. Fracture size, size of measurement area, mean aperture and SD of the initial aperture of G150A.

δs mm	Fractured size mm	Measured area mm	Initial mean mm	SD mm
0	150 × 150 (A)	144.8 × 150	2.26	0.45
2		144.8 ×148	2.78	0.65
4		144.8 × 146	3.00	0.83
8		144.8 × 142	3.73	1.14
12		144.8 × 138	3.93	1.41
16		144.8 × 134	4.70	1.72
20		144.8 × 130	4.70	2.03

Table 4.13. Fracture size, size of measurement area, mean aperture and SD of the initial aperture of G150B.

δ_s mm	Fractured size mm	Measured area mm	Initial mean mm	SD mm
0	150 × 150 (B)	148.1 × 140.8	1.20	0.40
2		148.1 × 138.8	2.48	0.50
4		148.1 × 136.8	1.80	0.51
8		148.1 × 132.8	4.22	0.78
12		148.1 × 128.8	5.19	1.10
16		148.1 × 124.8	4.75	1.41

Table 4.14. Fracture size, size of measurement area, mean aperture and SD of the initial aperture of G100A.

δ_s mm	Fractured size mm	Measured area mm	Initial mean mm	SD mm
0	100 × 100 (A)	65.1 × 55.9	1.56	0.42
2		65.1 × 51.1	2.01	0.30
4		65.1 × 49.2	2.67	0.51
8		65.1 × 47.9	3.90	0.52
12		65.1 × 43.6	3.63	0.98
16		65.1 × 39.5	3.38	1.14
20		65.1 × 34.9	6.61	3.08

Table 4.15. Fracture size, size of measurement area, mean aperture and SD of the initial aperture of G100B.

δ_s mm	Fractured size mm	Measured area mm	Initial mean mm	SD mm
0	100 × 100 (B)	65.1 × 51.8	1.56	0.31
2		65.1 × 50.7	1.45	0.32
4		65.1 × 47.8	1.86	0.41
8		65.1 × 43.9	6.20	0.77
12		65.1 × 39.8	2.49	0.92
16		65.1 × 35.9	3.40	1.18
20		65.1 × 31.8	3.66	1.31

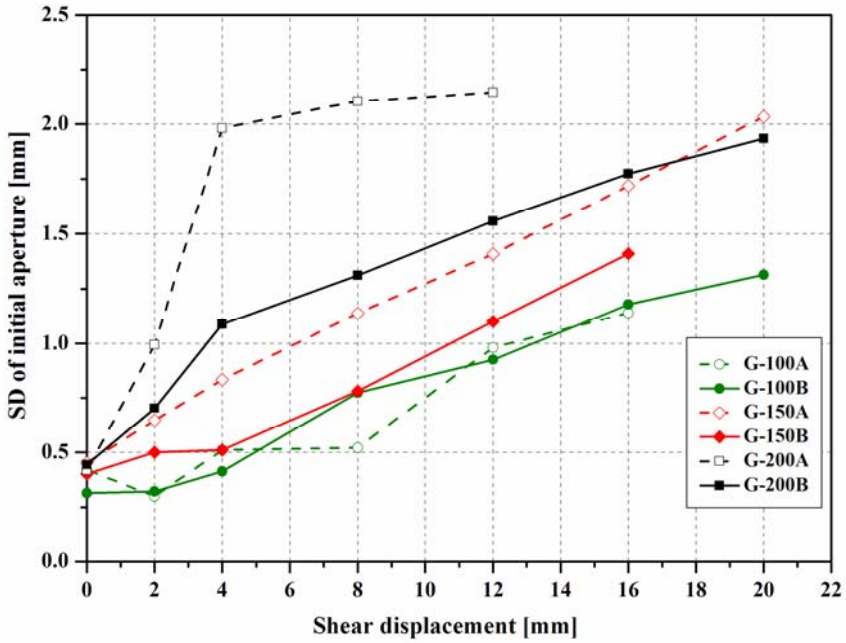

Fig. 4.16. Relation between shear displacement (δ_s) and the SD of the initial aperture (σ_0) as a function of fracture size.

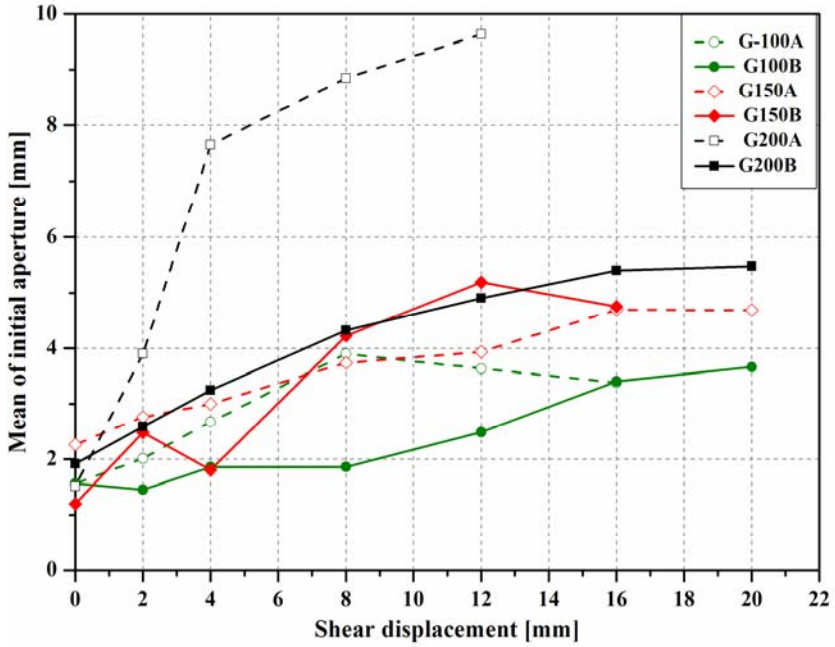

Fig. 4.17. Relation between shear displacement (δ_s) and the mean initial aperture as a function of fracture size.

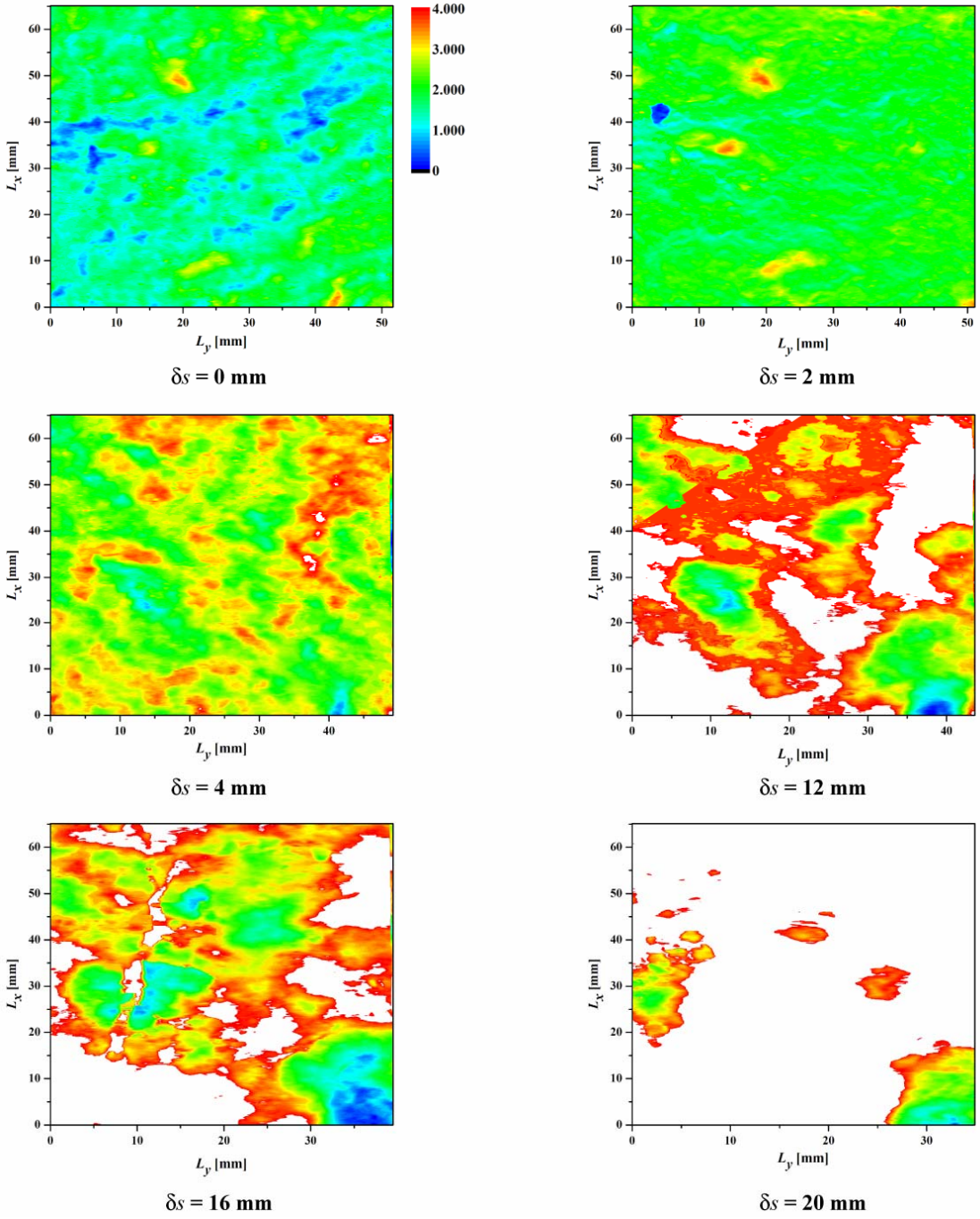

Fig. 4.18. Initial aperture distribution before and after shearing for G100A.

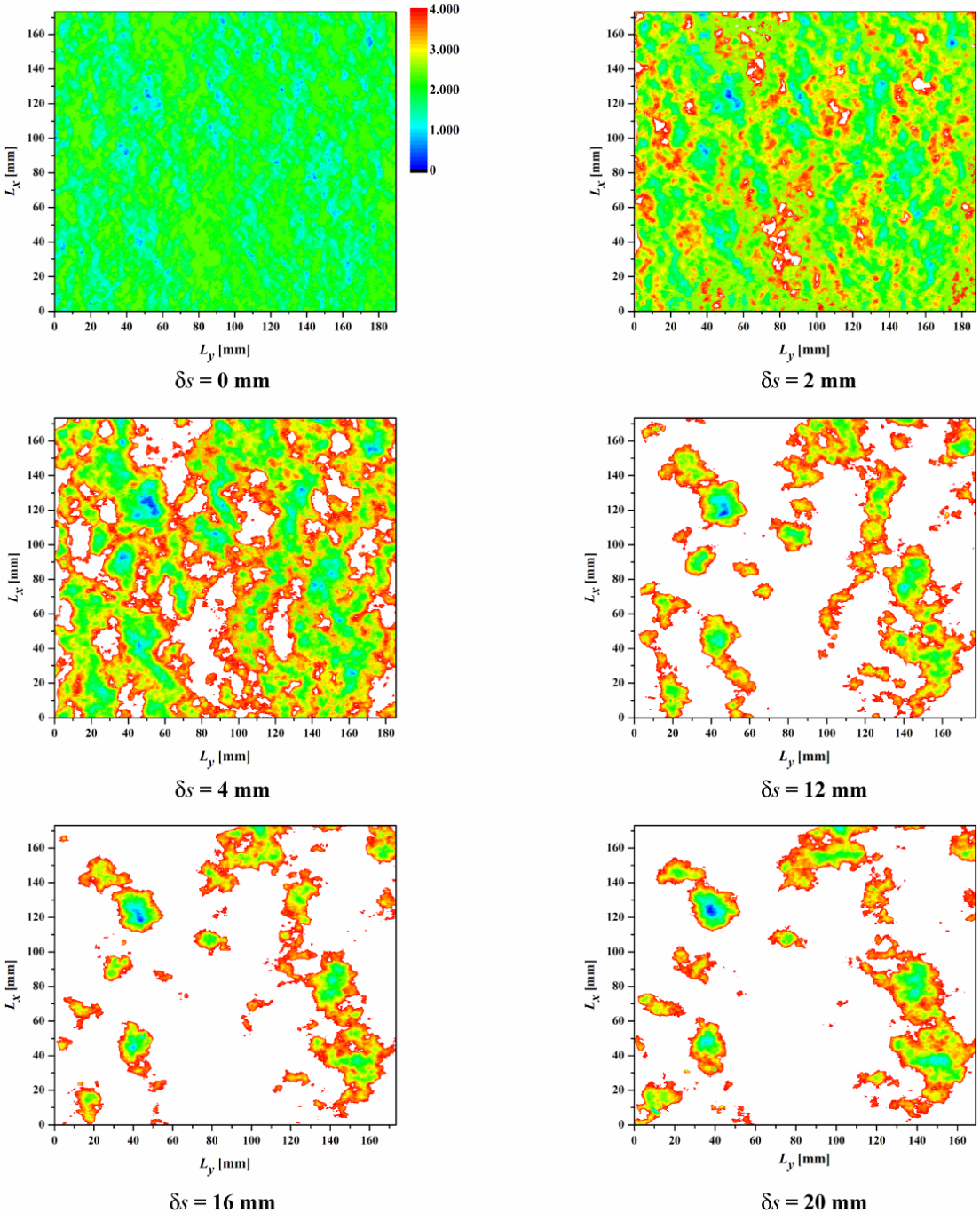

Fig. 4.19. Initial aperture distribution before and after shearing for G200B.

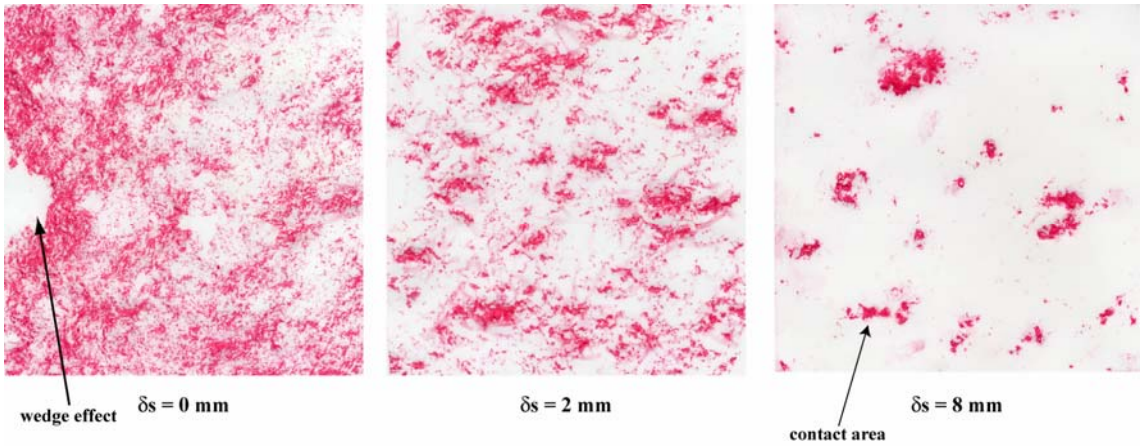

Fig. 4.20. Effect of shear displacement on contact area for G150A.

4.3.4 Power spectral density of surface height and aperture

The PSDs of the surface height and the initial aperture during shear were calculated using a fast Fourier transform (FFT) and plotted on a log-log diagram. Fig. 4.21 shows the PSDs of the upper (US) and lower (LS) surfaces heights during shearing for G100B, G150A and G200B, while Fig. 4.22 shows the PSDs of the initial aperture for the same fractures. These PSDs are ensemble-averaged for each specimen. The spatial frequency (mm^{-1}) is the inverse of the wavelength (mm). The relation for the surface height is approximately linear except for the highest frequencies. This deviation from linearity at high frequencies was considered due to an error in FFT.

Fig. 4.21 (a) shows that the PSD of the upper surface decreases with increasing shear displacement, especially for the shorter wavelengths with small asperities, for all fracture sizes. The amount of damages in small asperities with shorter wavelengths seems to decrease with increasing fracture size. However, US-G200B-20 mm was only slightly damaged contrary to this. Fig. 4.21 (b) shows that the PSD of the lower surface increases with shear displacement. This is because the gouges produced during shear are gathered on the lower surface and kept during the measurement process. Fig. 4.22 shows that the initial aperture has a power law spectrum only for at short wavelengths but flattens out at long wavelengths (low frequency).

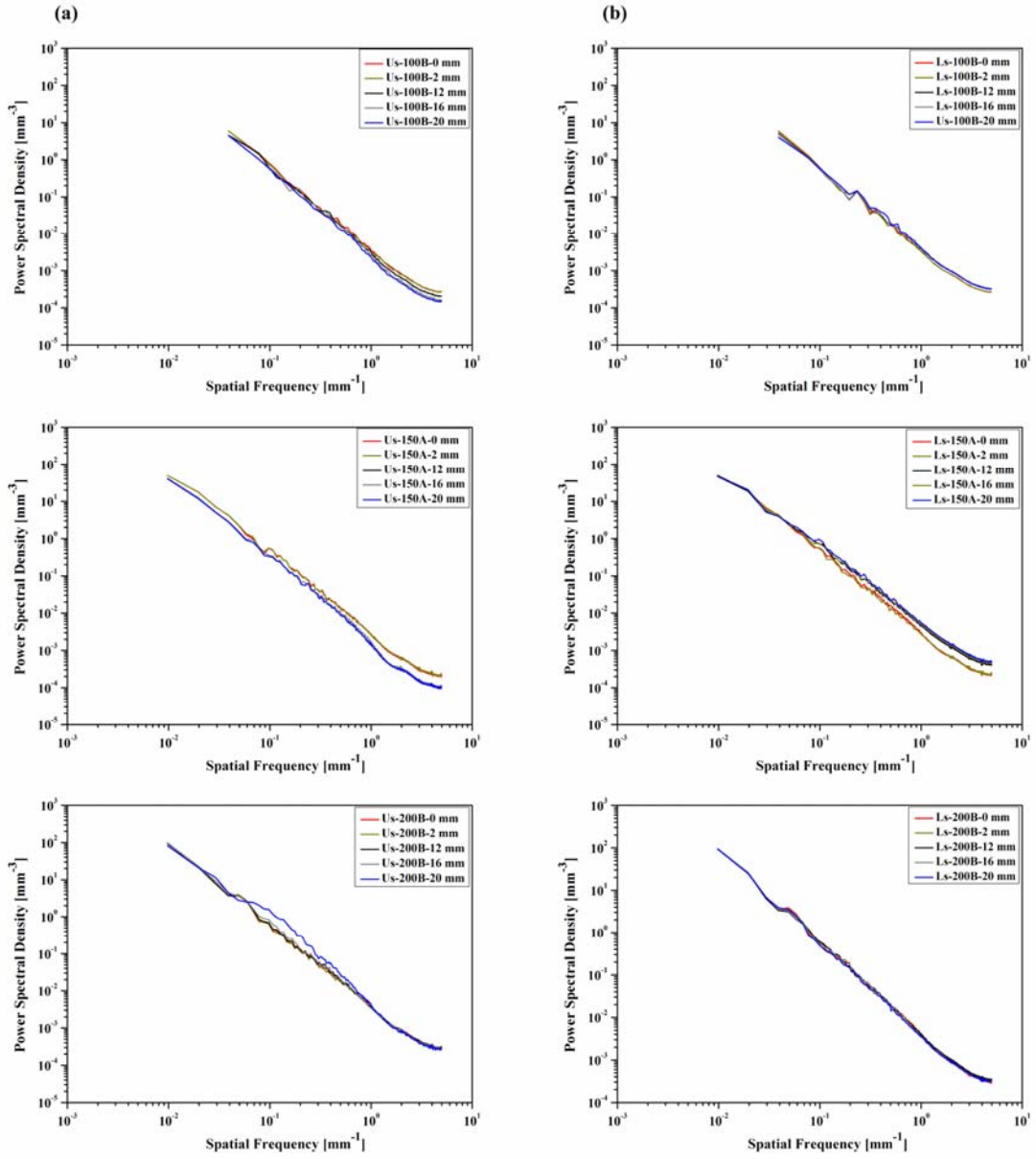

Fig. 4.21. Power spectral densities of the (a) upper and (b) lower surface heights of G100B, G150A and G200B.

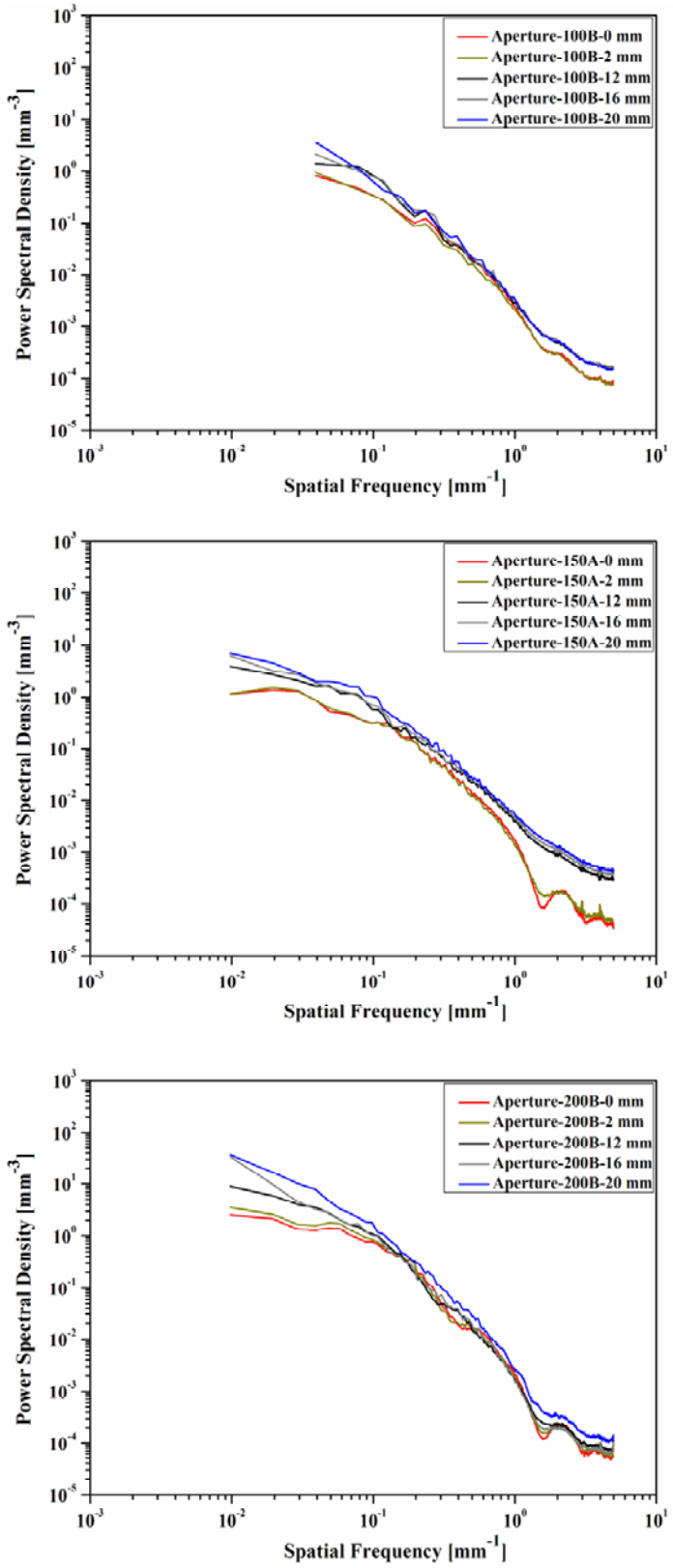

Fig. 4.22. Power spectral densities of initial aperture of G100B, G150A and G200B.

Fig. 4.23 shows the PSD of the upper surface height at shear displacements (δs) of 0 and 12 mm for G-100B and G-200A. This figure clearly shows that smaller asperities with shorter wavelengths were more damaged by shear for both fracture sizes, while larger asperities with longer wavelengths were not significantly damaged, as shown in Fig. 4.21(a). Moreover, Fig. 4.23 indicates that shearing-off mostly occurred for asperities with wavelengths less than about 2.5 mm for G-100B and about 5 mm for G-200A. Thus, large asperities with long wavelengths still have a great resistance to shear displacement for G-200A at the applied normal stress of 10MPa.

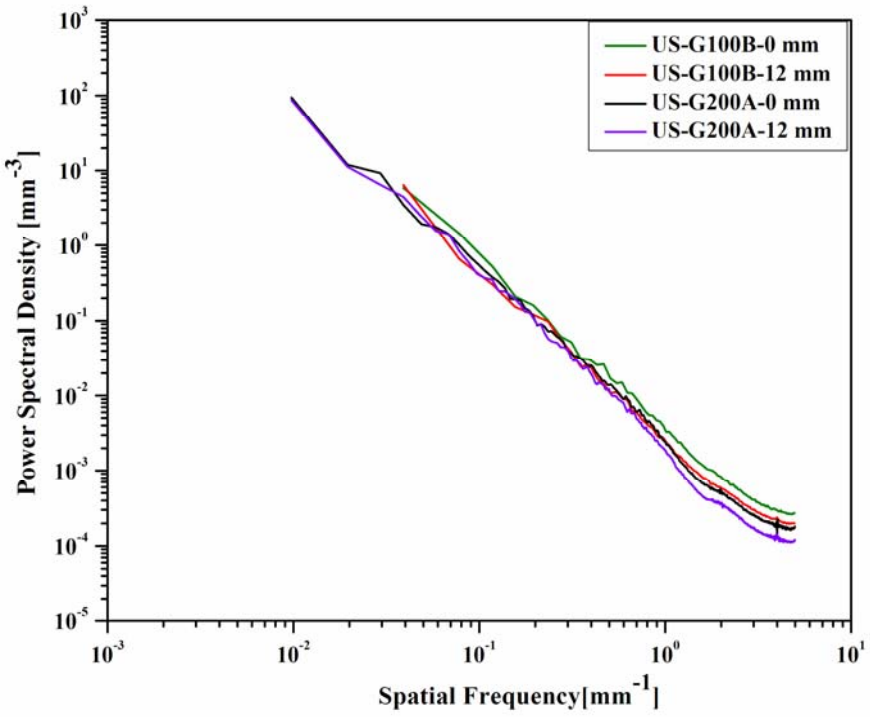

Fig. 4.23. Power spectral density of the upper surface height at shear displacements of 0 and 12 mm for G-100B and G-200A.

4.4 Size effect on mechanical behaviors

As mentioned in section 3.2, several shear tests have been performed on the tensile fracture created in granite with different sizes under normal stress of 10 MPa. In this section, the size effect on the mechanical behavior of the fracture sample was investigated and attention is mostly paid to the non-linearity of the closure curve and the normal and shear stiffnesses.

4.4.1 Closure curve

As stated earlier, the measurement of the closure curve was performed at shear displacements of 2, 4, 8, 12, 16 and 20 mm. Fig. 4.24 (a) and (b) shows the effect of shear displacement on the non-linearity of the closure curve for G100B and G150A, respectively. It can be said that the non-linearity increases with shear displacement since the matedness decreases with the shear displacement. Since G100B-16 mm was cracked during the test, an abrupt increase in the non-linearity of the closure occurred. Fig. 4.25 shows the effect of fracture size on the closure curve. This figure clearly shows that the non-linearity also increases with fracture size since the matedness decreases with fracture size and that the SD of the initial aperture increases with fracture size. Pervious studies have shown the same tendency of the closure curve under normal stress [9, 11, 13, 133]. Thus, it can be concluded that the closure of the fracture during shearing is scale dependent.

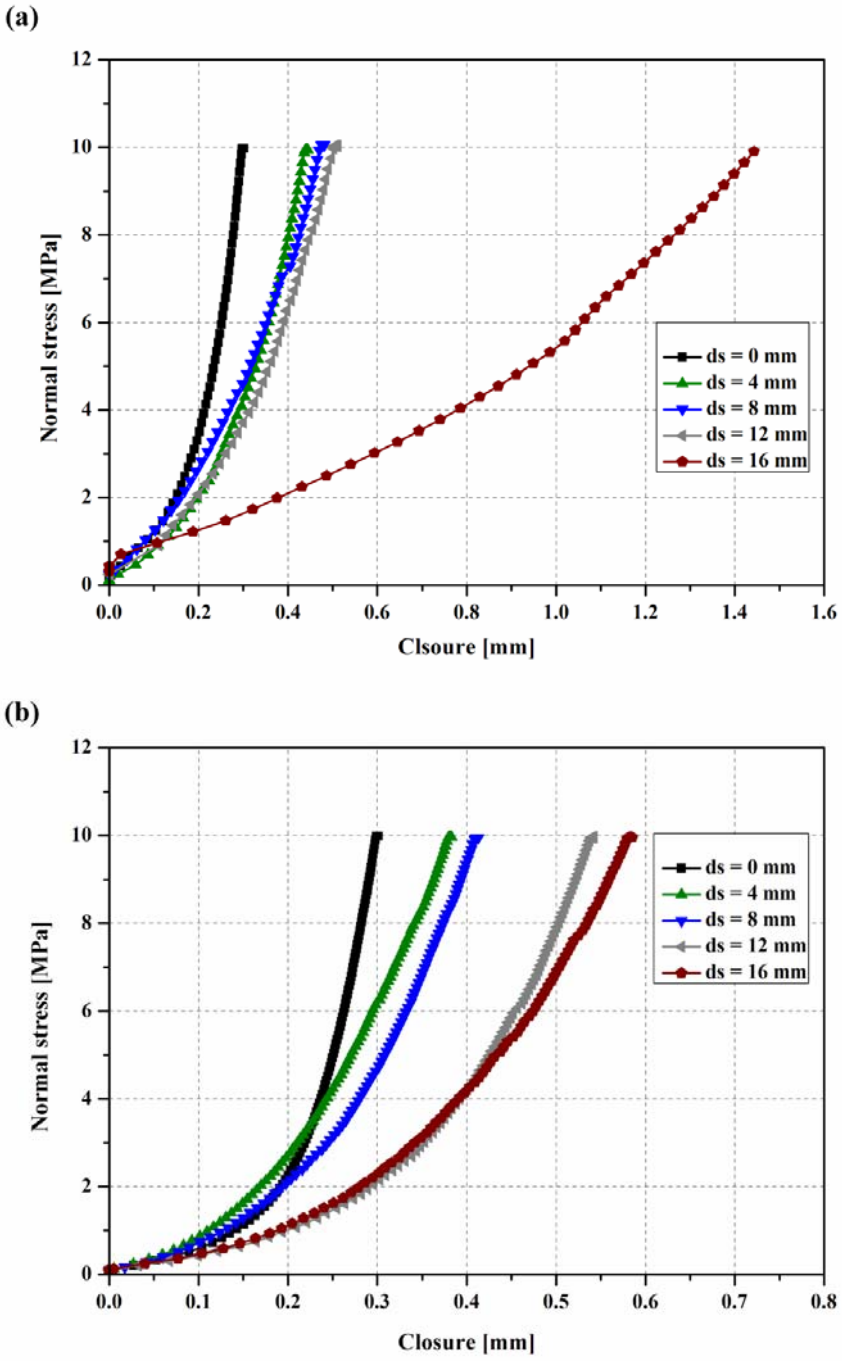

Fig. 4.24. Effect of shear displacement on closure curve for (a) G-100B and (b) G150A.

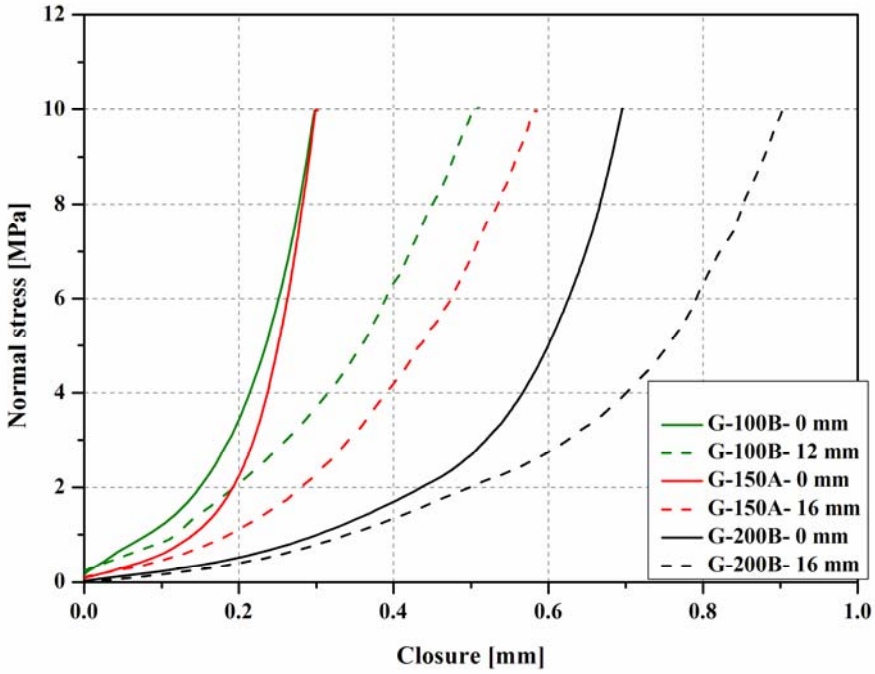

Fig. 4.25. Effect of fracture size on closure curve for G-100B, G150A and G200B.

It is well known that the shear stress applied to a fracture at low normal stresses many cause the asperities of surfaces to slide past one another, leading to large dilation/increasing in aperture. On the other hand, for a very high normal stress the frictional forces resisting slip may exceed the strength of the rock and the asperities will be sheared off. Consequently, dilation would be minimal in this case. For the sake of better understanding, Fig. 4.26(a) shows a series of shear stress versus shear displacement curves for a fracture tested under constant normal stresses ranging between A and $20A$, where A is an arbitrary number, while Fig. 4.26(b) shows a decrease in joint dilatancy as normal stress increases from A to $20A$ [143].

Previous studies considered that the shear dilation was mainly caused by the surfaces sliding over, which gives the dilation angle (Fig. 1.10, and Fig. 4.26) [6, 11, 14, 54, 61, 79, 143-145]. However, Fig. 4.24 and Fig. 4.25 indicate that the non-linearity of the closure increases with shear displacement because the contact area decreases, and accordingly the closure effect should be added when the dilation is considered, as schematically shown in Fig. 4.27. Thus, the normal displacement is determined by two factors: one is by the sliding over between the asperities and the other is by closure behavior at the normal stress. When the dilation caused by the geometry of the asperities is assumed to be constant, dilation should be reduced by an increase in the

non-linearity in the closure curve with shear displacement. Thus, the decrease in the dilation angle is caused not only by the damage in the asperities, but also by an increase in the non-linearity in the closure curve by shear displacement.

.

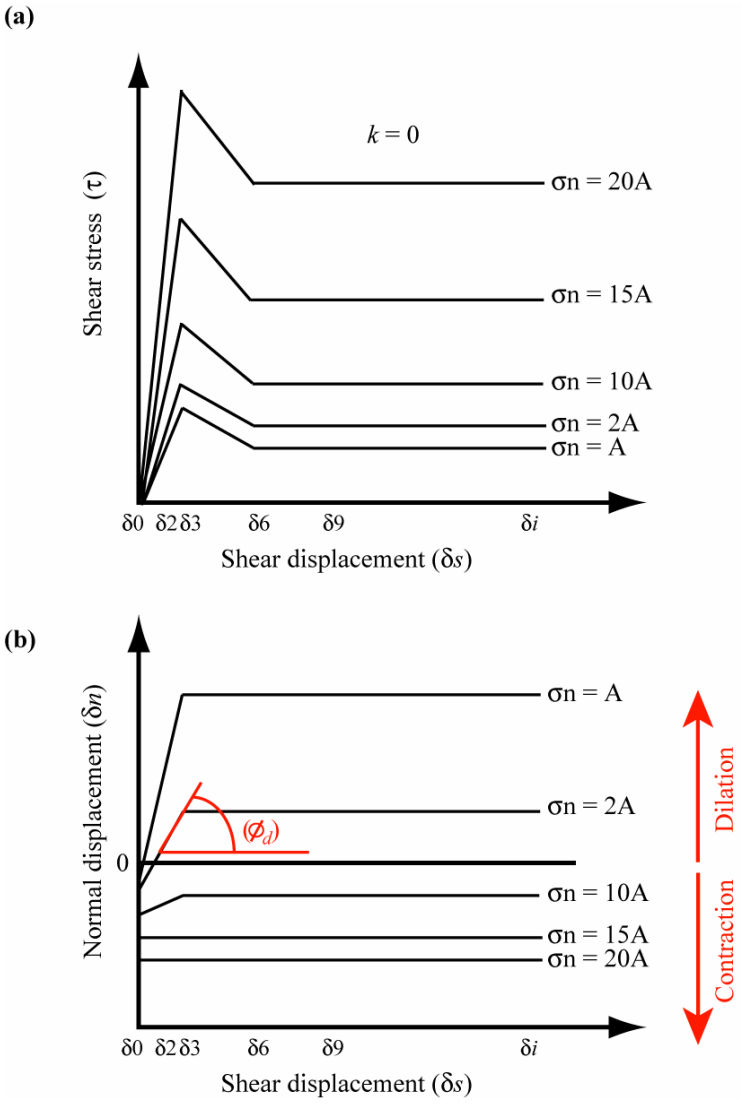

Fig. 4.26. Schematic of the curves for normal stresses ranging between A and 20A for (a) shear stress-displacement curve and (b) shear-normal displacement curve (Goodman and Boyle, 1985).

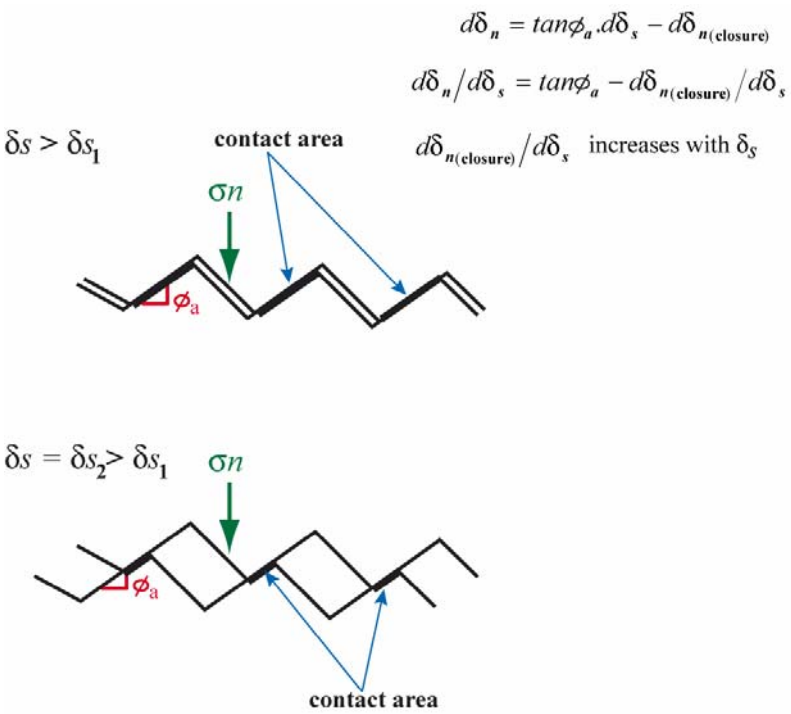

Fig. 4.27. Schematic of the effect of the non-linearity of the closure curve on shear dilation.

4.4.2 Normal and shear stiffnesses

The normal stiffness (k_n) is defined by

$$k_n = \frac{d\sigma_n}{d\delta_n}, \tag{4.5}$$

where σ_n = normal stress and δ_n = closure.

When the Goodman formula holds for the closure curve, the normal stiffness can be given by

$$k_n = \frac{B\sigma_n}{\ln(\sigma_n / A)}, \tag{4.6}$$

where A & B = constants determined by the least squares method under the assumption that $\sigma_n = Ae^{B\delta n}$.

The shear stiffness (k_s) is defined by

$$k_s = \frac{\Delta\tau}{\Delta\delta_s}, \tag{4.7}$$

where $\Delta\tau$ and $\Delta\delta$ are the differences in shear stress and shear displacement, respectively, for a given range. In this study, the secant modulus between the peak and 50% of the peak shear stress was used.

To investigate the effect of fracture size on the normal stiffness (k_n) with different shear displacements, k_n was estimated according to Equation (4.6) at normal stress of 3 and 10 MPa for G100A, G150A and G200B, as shown in Fig. 4.28. The k_n tends to decrease with fracture size, which is in agreement with previous studies [10, 11]. This is mainly due to the fact that unmatedness increases with fracture size as the SD of the initial aperture increases with fracture size. The effect of fracture size on the shear stiffness (k_s) is shown in Fig. 4.29. For all fracture sizes, k_s increases with the shear displacement in the initial stage, but after the peak at 4 mm of shear displacement, it decreases with shear displacement to reach an almost constant value at a certain amount of shear displacement. On the other hand, while k_s decreases with fracture size in the initial stage, which is consistent with pervious studies [6, 10, 11], k_s increases with fracture size in the residual stage. In the initial stage, k_s decreases with fracture size since the fracture surfaces are less mated for a larger fracture. However, smaller asperities with shorter wavelengths are more easily damaged by shearing, depending on the normal stress, and as a result, larger asperities with longer wavelengths remain to resist the shear displacement. Thus, k_s of a larger fracture that contains components of longer wavelengths are greater in the residual stage than that of a smaller fracture.

It should be mentioned that the results demonstrated above for the tendency of k_s were obtained under the ratio of the normal stress to tensile strength of about 1.5. Hence, these results would be only valid for the ratio of less than 1.5, since all asperities would be sheared off for a high value of the ratio.

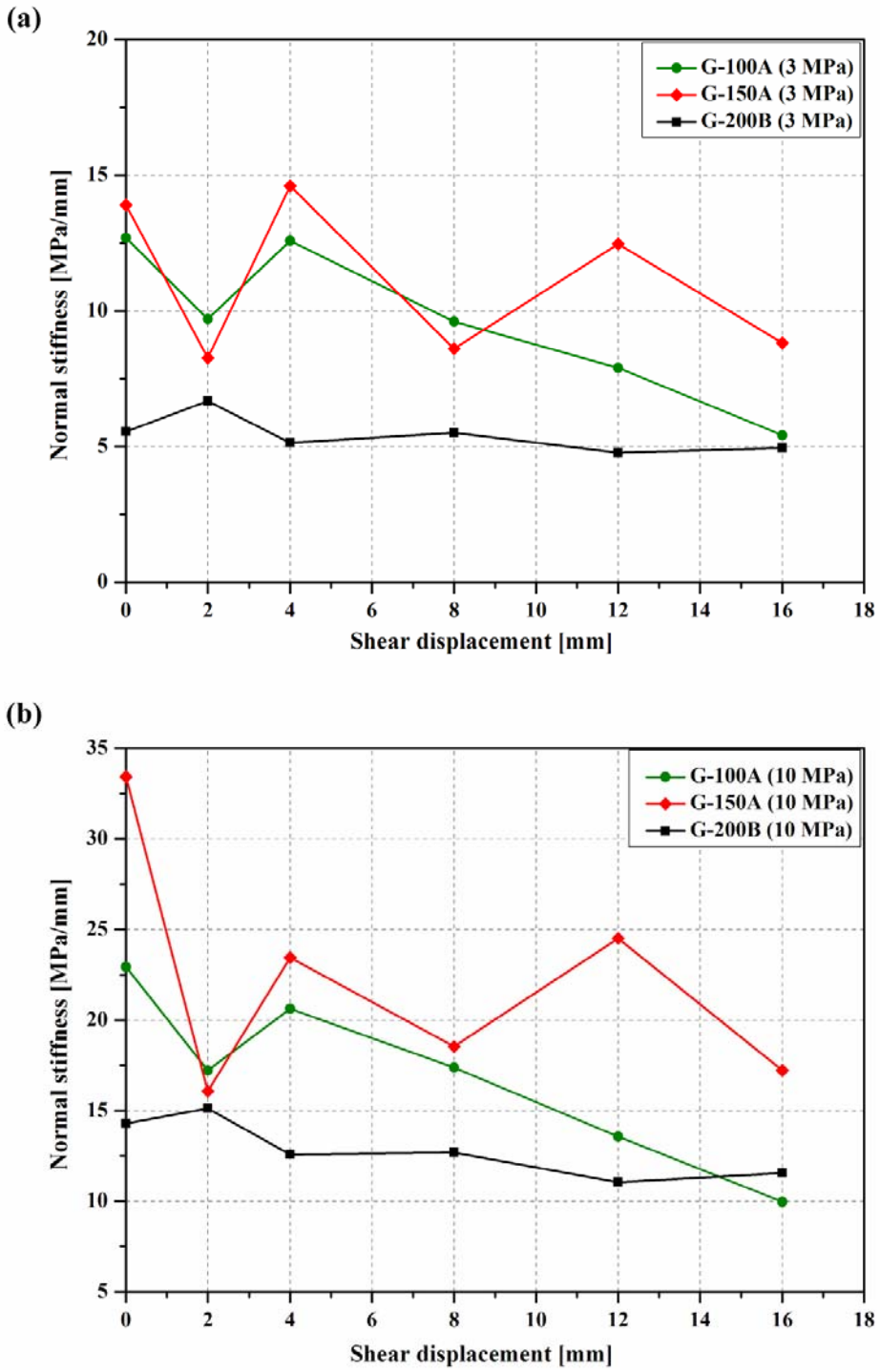

Fig. 4.28. Normal stiffness at normal stress of (a) 3 MPa and (b) 10 MPa as a function of shear displacement for G100A, G150A and G200B.

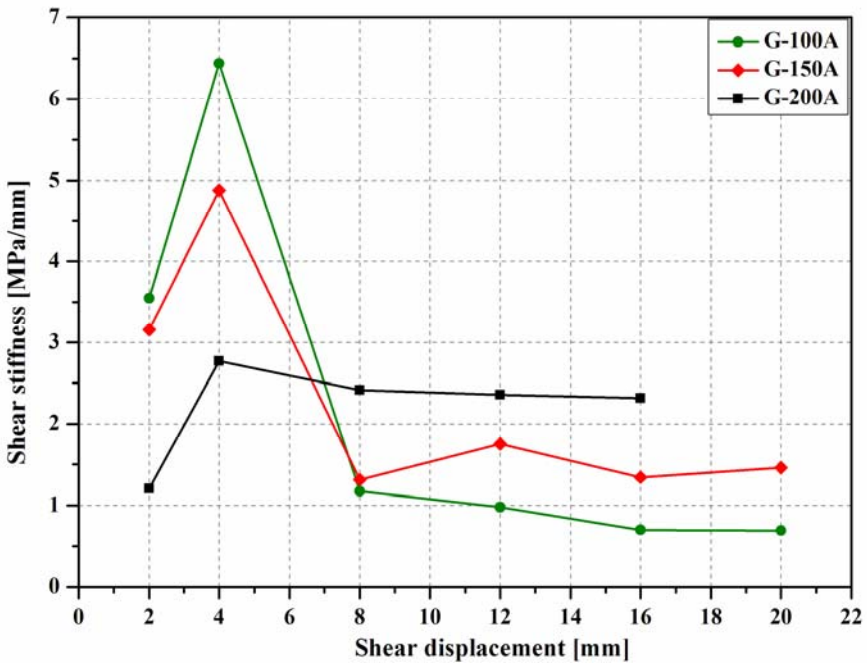

Fig. 4.29. Shear stiffness as a function of shear displacement for G100A , G150A and G200A.

4.5 Comparison between experimental and numerical results of the SD of the initial aperture

In the previous study [17], fractures were numerically sheared under a very low normal stress without considering breakage of surface asperities. In reality, the surfaces of a fracture would be more or less damaged when the fracture is sheared under a normal stress. Accordingly, the aperture distribution would be affected by the damage of the surfaces. Therefore, I aimed to investigate the effect of surface damage by comparing numerical simulation with experimental results.

Since all fracture surface heights were measured before shearing, shear displacement was numerically introduced. For each designated shear displacement value, statistical parameters were estimated and compared with the experimental results. Fig. 4.30 shows the difference between the SDs of the initial apertures that were estimated numerically without damage of the asperities and experimentally with damage of asperities. Clearly, the SD of the initial aperture that was estimated experimentally is greater than the numerical one. This is due to the fact that the matedness in the actual surfaces is less that in the simulated one because of the damage of the asperities. However, these differences are not so significant for this type of rock. As the aperture is produced from the mismatching of the two surfaces, Fig. 4.31 shows the simulation results of the SD of the upper and lower surfaces in comparison with the experimental results. Note that

only the effect of area reduction due to shear effect on the SD of the surface height is estimated in the simulation. Fig. 4.31(a) shows the results of the SD of the upper surface which was almost similar between the simulation and the experiment, except G150A-12 and 16 mm. Fig. 4.31(b) shows the SD of the lower surfaces for both conditions. Since all the gouges are gathered on the lower surface, the SD of the surface height obtained in the experimental tends to be greater than that obtained in the simulation.

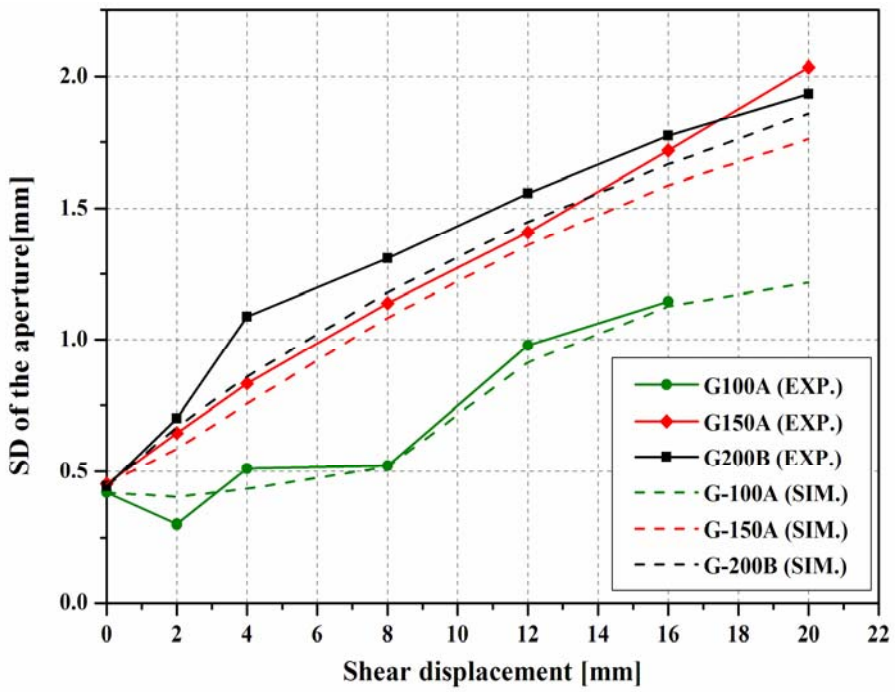

Fig. 4.30. Comparison of the SD of the initial aperture obtained by numerical and experimental methods.

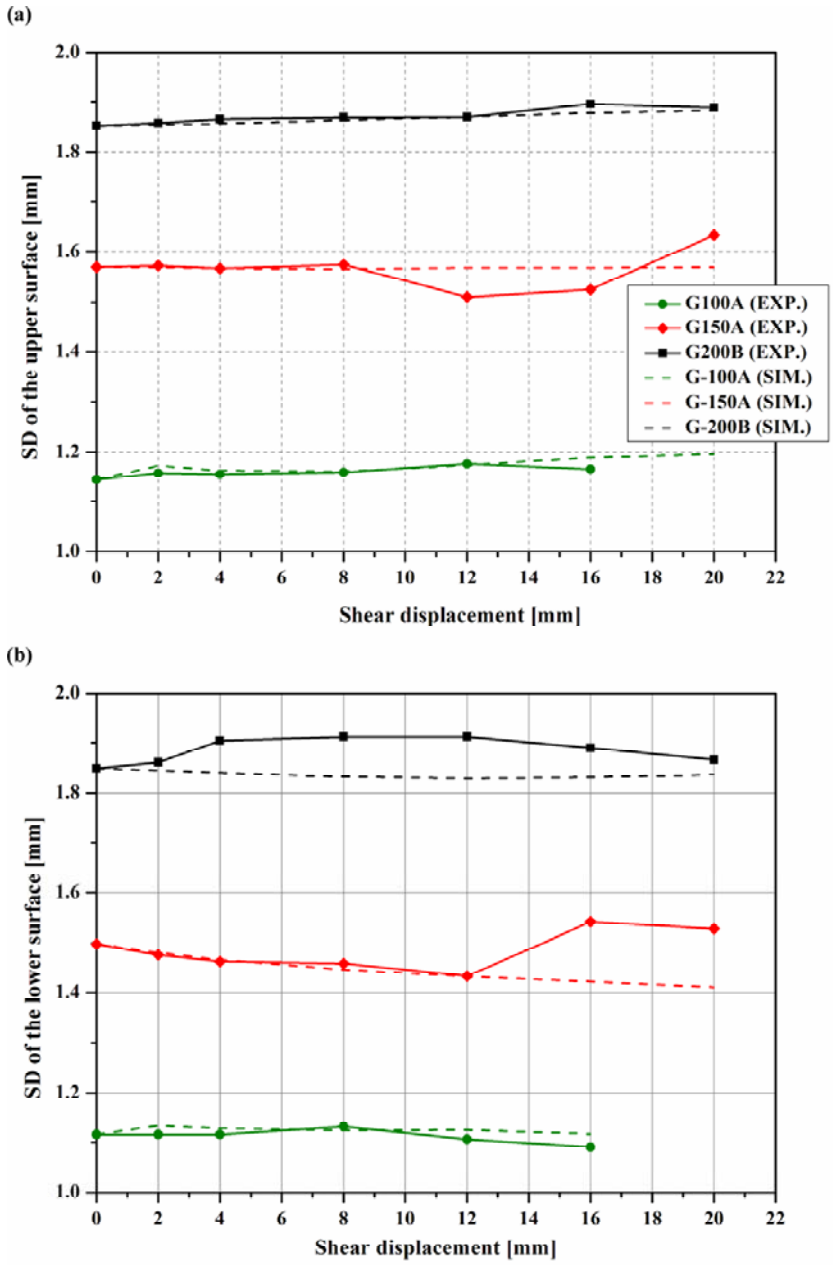

Fig. 4.31. Comparison of the SD of the surfaces obtained by numerical and experimental methods for the (a) upper surfaces and (b) lower surfaces.

4.6 Asperity degradation

During the shear sliding under normal and shear loads, both surfaces of a rock fracture are subjected to damage when the peak strength of the rock is reached. The area of damaged zone depends on the magnitude of the applied normal stress [146]. In general, shearing causes two main types of damage: crushing and shearing of asperities.

To understand how surfaces change with shearing, fracture surfaces of six samples were measured before and after shear tests. Fig. 4.32 and Fig. 4.34 show the areas when the heights of the upper surface decreased after shearing by 2, 4, 12 and 20 mm for G-100B, G150A and G200B, respectively. Clearly, damaged zones were enlarged in the direction of the shear displacement and localized with shear displacement. Furthermore, damage zones tend to form perpendicular to the shear displacement.

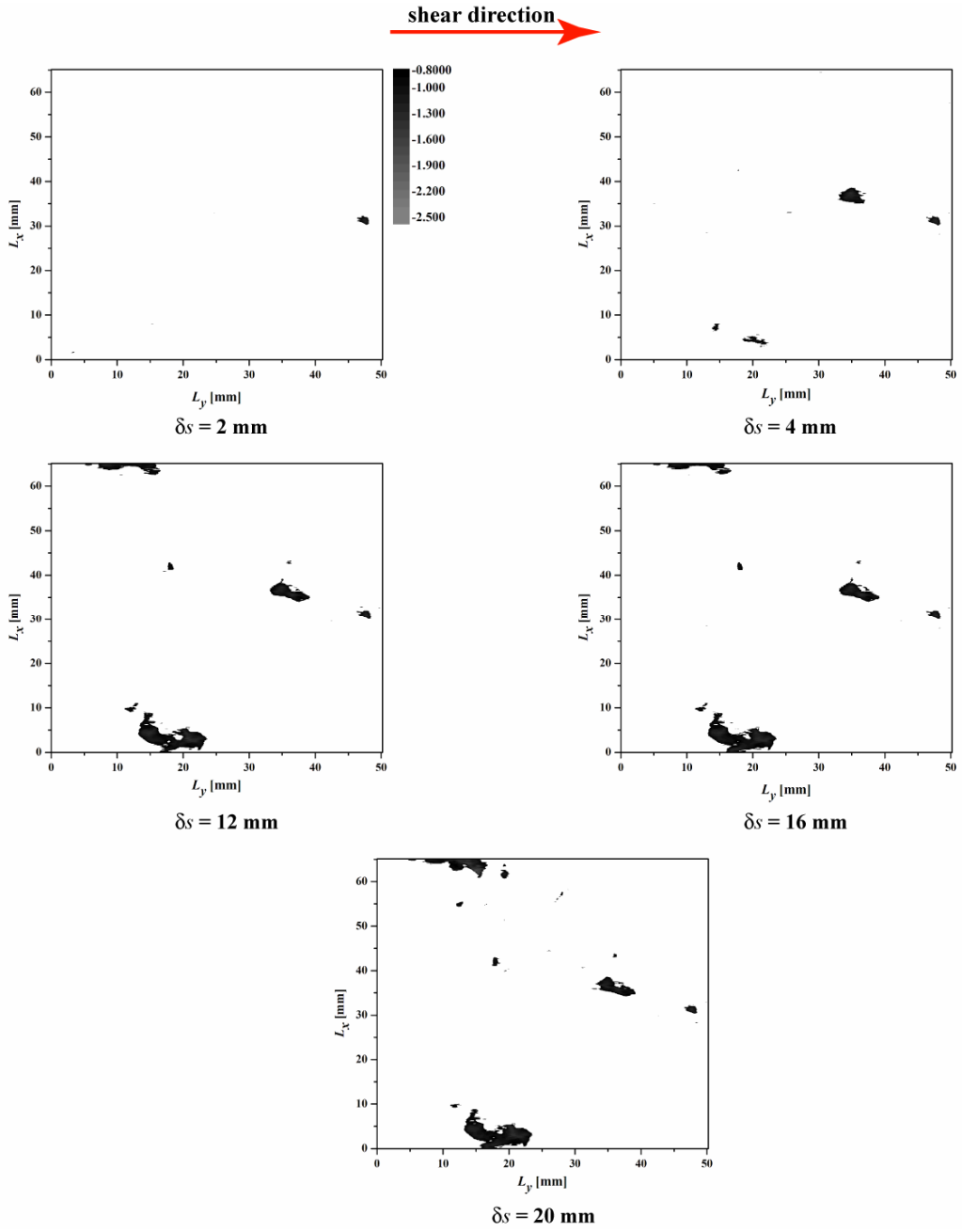

Fig.4.32. Effect of shear displacement (δ_s) on damaged areas in the upper surface for G-100B.

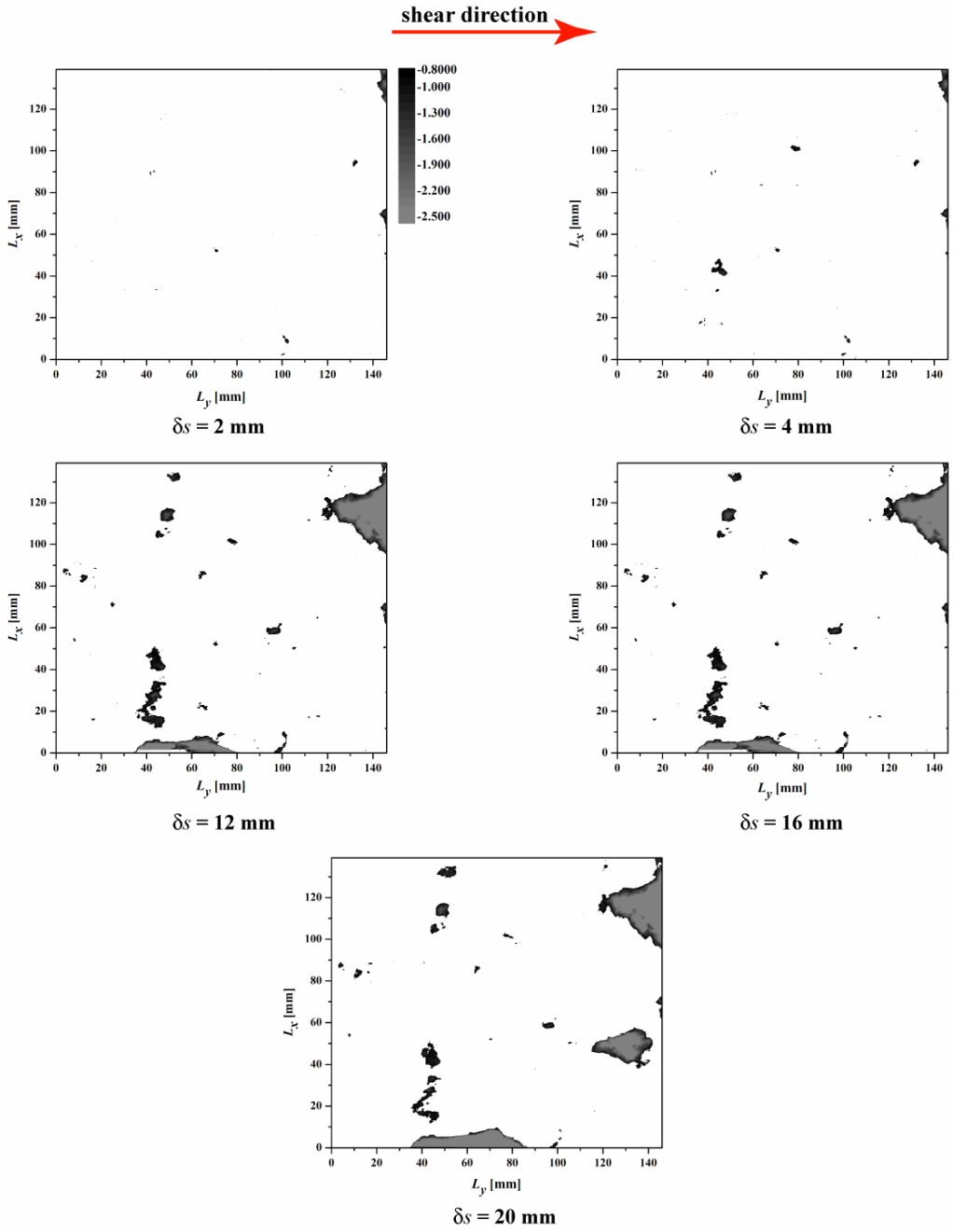

Fig.4.33. Effect of shear displacement (δ_s) on damaged areas in the upper surface for G-150A.

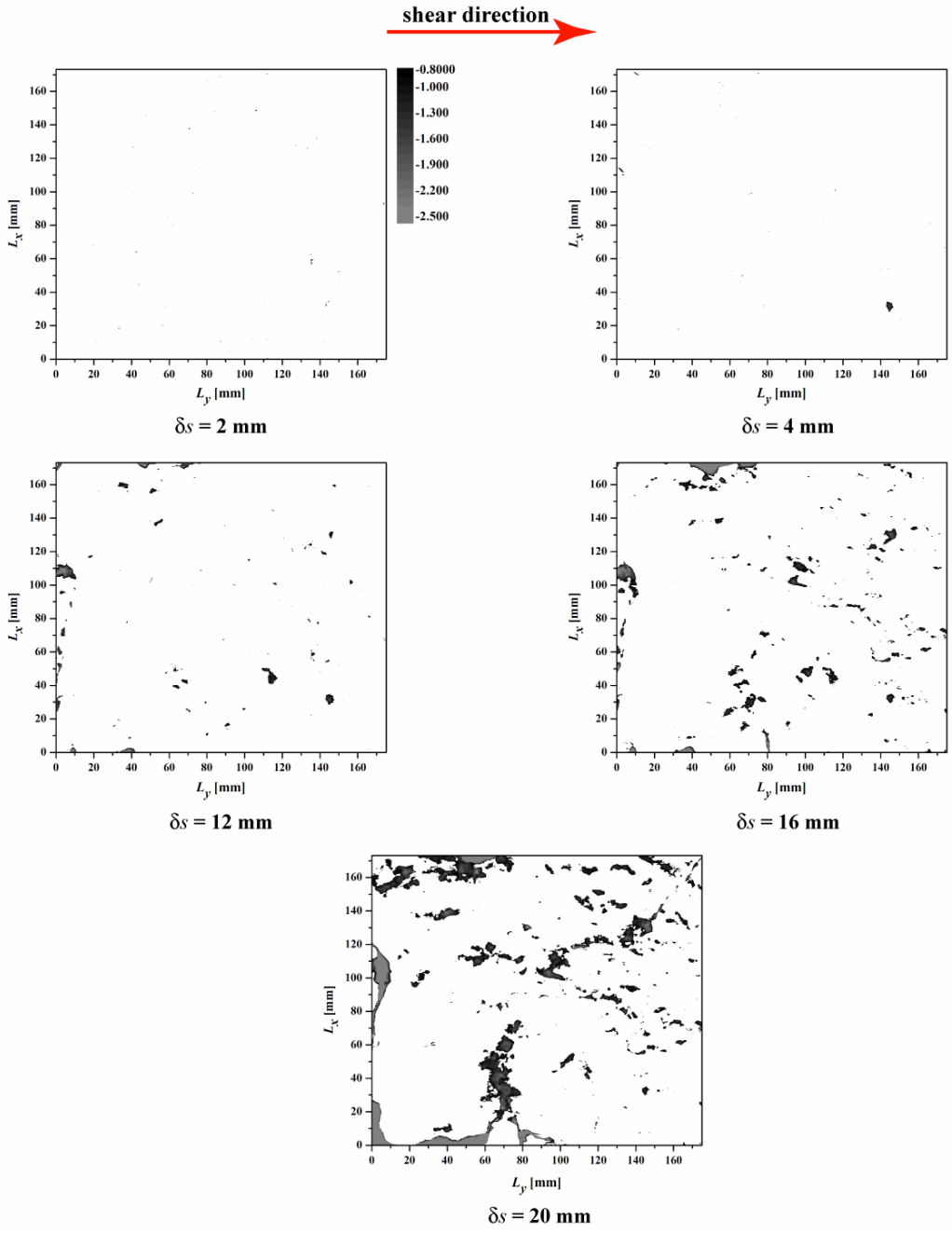

Fig.4.34. Effect of shear displacement (δ_s) on damaged areas in the upper surface for G-200B.

4.7 Summary

In this chapter, tensile fractures were created in a block of Inada granite by intending steel wedges to prepare fractures that measured from 100 mm to 200 mm. The size effect on the shear behavior of the fracture was investigated experimentally by performing cyclic shear loading under a normal stress of 10 MPa. The surface topography and the initial aperture were measured before and after shearing at designated shear displacements by a laser profilometer. The main findings can be summarized as follows:

1) The SD of the initial aperture increases with both shear displacement and fracture size. As a result, the closure curve tends to become more non-linear with shear displacement since the matedness of the fracture surfaces decreases with shear displacement. Thus, shear dilation is not only governed by the surfaces sliding over, but the increase in the non-linearity of the closure curve with shear displacement also has significant effects on shear dilation.
2) The normal and shear stiffnesses in the initial stage decrease with fracture size because the matedness decreases as the SD of the initial aperture increases with fracture size. However, the shear stiffness in the residual stage increases with fracture size. This can be attributed to the fact that only small asperities with short wavelengths are mainly damaged by shear, as indicated by the change in the PSD of the surface heights during shear.
3) Contact area gradually decreases during shearing due to the shear-offset. However, the distribution of the contact area is locally expanded with shear displacement.
4) The damaged zones are enlarged and localized with shear displacement, and tend to form perpendicular to the shear displacement.

5. EFFECTS OF SIZE AND NORMAL STRESS ON SHEAR BEHAVIOR OF MORTAR REPLICA

The effect of normal stress on the shear behavior was investigated in the direct shear tests by using mortar fracture replicas of sizes 100 mm × 100 mm, 150 mm × 150 mm and 200 mm × 200 mm, which were produced from a tensile fracture created in granite. Monotonic shear loading was applied at normal stresses of 0.3 and 1 MPa for shear displacements of 2 and 20 mm. The change in the surface topography under different normal stress was measured by using a profile measurement system with a laser profilometer to determine the evolution of surface damage and aperture during shear.

Moreover, within these experiments, the effect of gouge materials on the non-linearity of the closure was also investigated. In this chapter, after the closure was measured with the presence of the gouge, the specimen was removed from the shear box, and the surfaces were cleaned from the gouge material. Then, the specimen was put back into the shear box and the closure was measured again for the surfaces without the gouge materials.

5.1 Set-up procedure for shear test

To set the initial position of the specimen at the beginning of the test, the two halves of the fracture surfaces are matched together manually. For each shear test, the following producer was taken:

1) Fracture surface heights were measured once before shearing for each size,
2) Shear displacement was applied monotonically with a rate of 0.5 mm/min at normal stresses of 0.3 and 1 MPa and shear displacements of 2 and 20 mm, and
3) the statistical parameters and surface damage evolution as functions of normal stress and shear displacement were estimated.

5.2 Mechanical parameters of mortar replica

Since the decision was made to use the mortar fracture replica during these experiments, a step had to be taken to choose the hardest mortar among three water/cement mixing ratios of 0.4, 0.50 and 0.55. Hence, the mechanical properties of each mortar were tested for the judgment based on the results.

5.2.1 Uniaxial compression test

The uniaxial compressive strength (UCS) was determined according to ISRM recommendations [147] and tests were carried out for specimens of regular geometry. For each mixing ratio, five specimens were tested and their average values were calculated. Since the same testing producers that were applied in section (4.2) for granite specimen were followed, only final results are presented. It should be noted that all specimens were cured in water at 40^{o}C for 4 days before testing, as shown in Fig. 5.1.

Fig. 5.2 shows an example of the UCS test results (Sample No. 1). The final average test results are summarized in Table 5.1.

Fig. 5.1. Making and preparing the mortar core samples to be tested.

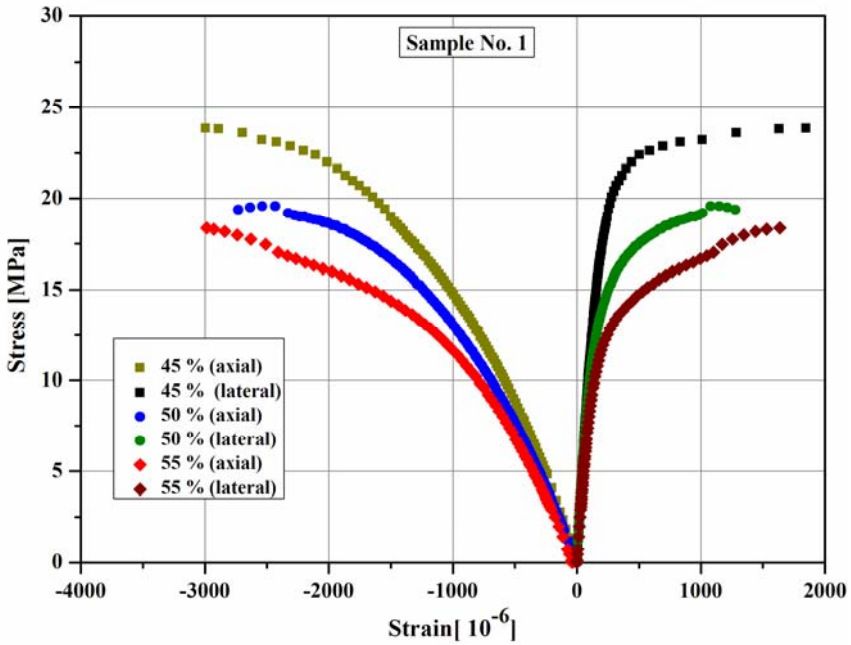

Fig. 5.2. Uniaxial compressive strength of the mortar replicas for 45%, 50% and 55% of mixing ratio.

Table 5.1. Mechanical properties of mortar replicas.

Mixing ratio W/C (%)	E (GPa)	ν	UCS (MPa)
55 %	10.70	0.37	19.00
50 %	11.86	0.26	19.38
45 %	14.70	0.20	26.14

5.2.2 Tensile Strength

The Tensile strength was estimated by the Brazilian test according to the ISRM suggestions [148], with the same testing producers that were applied in section (4.2). Fig. 5.3 illustrates an example of the result (Sample No.3, 45%). The final average test results are summarized in Table 5.2.

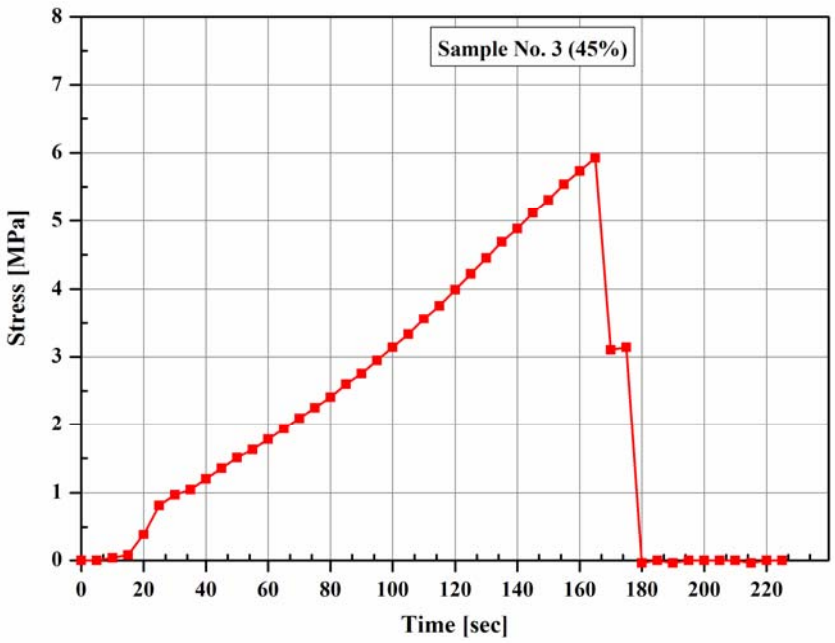

Fig. 5.3. Example of tensile strength test result for mortar replicas for 45% mixing ratio.

Table 5.2. Tensile strength test results of mortar replicas.

Mixing ratio, W/C (%)	Tensile strength (MPa)
55 %	2.53
50 %	3.50
45 %	3.65

Based on the mechanical properties results of the three mixing ratios, water/cement ratio of 45% was chosen to be used to produce the mortar replicas since it gave the greatest strength.

5.3 Effect of stress, size and shear displacement on surfaces and aperture

During the shear tests, the following parameters were recorded every 5 second: shear load, normal load, shear displacement and normal displacement. In total, 16 mortar replicas of sizes 200 × 200 × 80 mm, 150 × 150 × 80 mm and 100 × 100 × 80 mm, were reproduced and called M200, M150 and M100, respectively. Fig. 5.4 to Fig 5.5 show both the shear stress (τ)- shear displacement (δ_n) curve and the normal displacement (δ_n)- shear displacement (δ_s) curve that were obtained at 2 and 20 mm, respectively. For each normal stress and shear displacement, the surface topography was measured by using a profile measurement system with a laser profilometer to determine the statistical parameters and the PSD. Additionally, the evolution of the surfaces damage during the shear test under different values of normal stress was estimated. Keep in mind that for each fracture the surface heights were measured also before shearing.

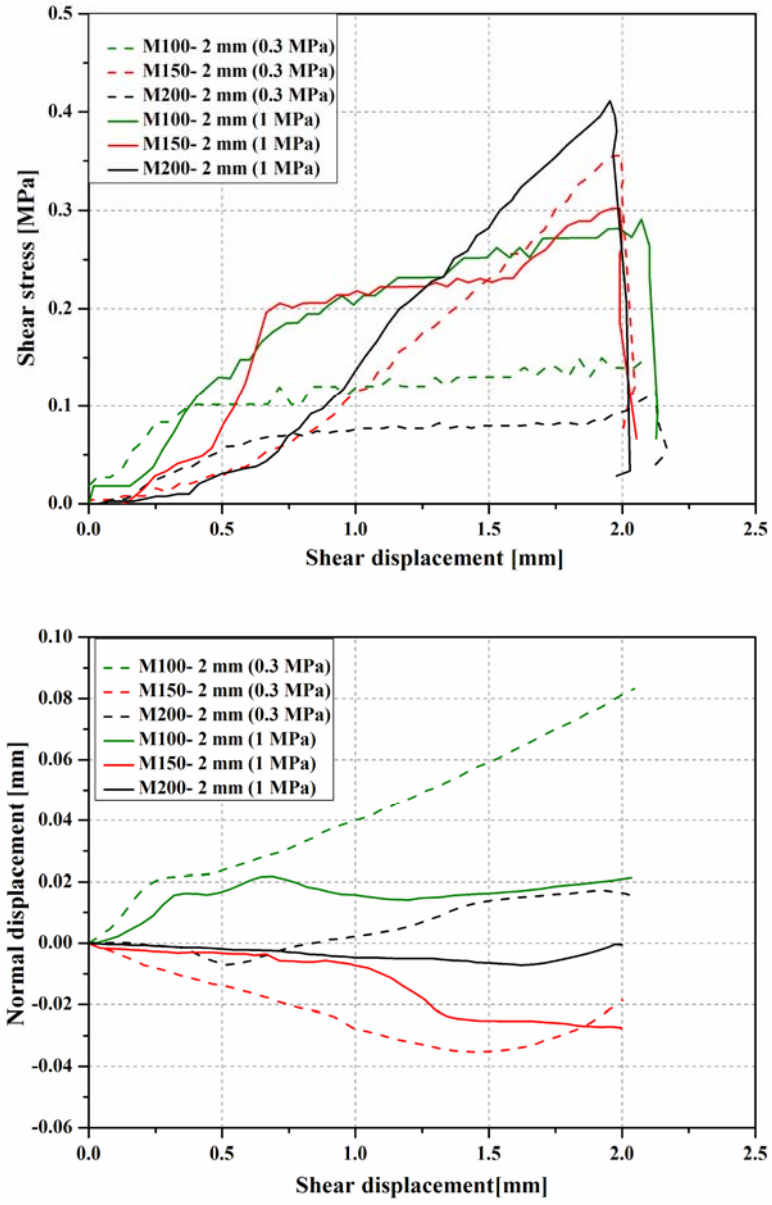

Fig. 5.4. Shear stress- shear displacement and normal displacement-shear displacement curve at 2 mm for all mortar replicas.

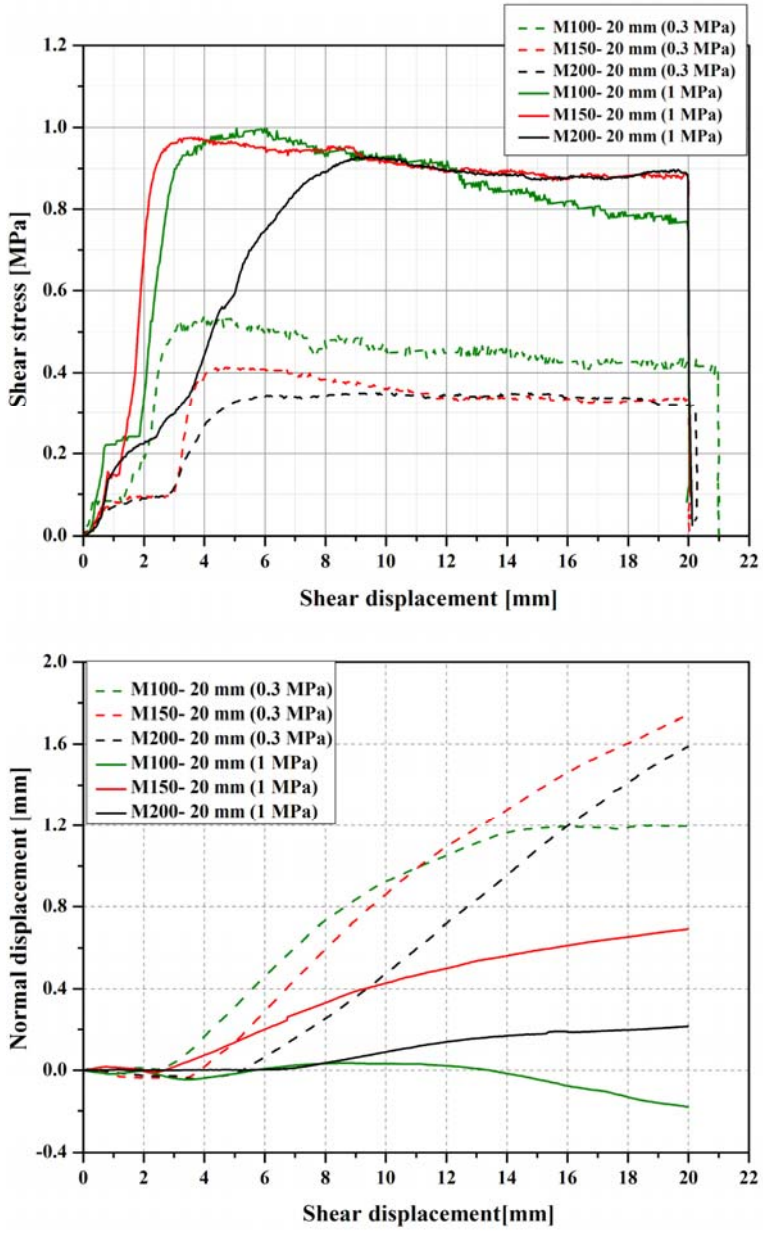

Fig. 5.5. Shear stress- shear displacement and normal displacement-shear displacement curve at 20 mm for all mortar replicas.

5.3.1 Morphological characterization of mortar replica

Fig. 5.6 shows the PDF of the lower surface heights for M100 at normal stresses of 0.3 and 1 MPa and shear displacements of 0, 2 and 20 mm. It can be said that the shear displacement does not have a great effect on the peak value of PDF, while the normal stress slightly increases the peak values of the PDF.

Fig. 5.7 shows an example of the effect of fracture size on the PDF of the lower surface height at normal stress of 0.3 MPa and shear displacement of 20 mm for M100, M150 and M200. The peak values decreases with fracture size and becomes broader. For each fracture size, the standard deviation of the surface height was calculated and the result will be discussed on the following section.

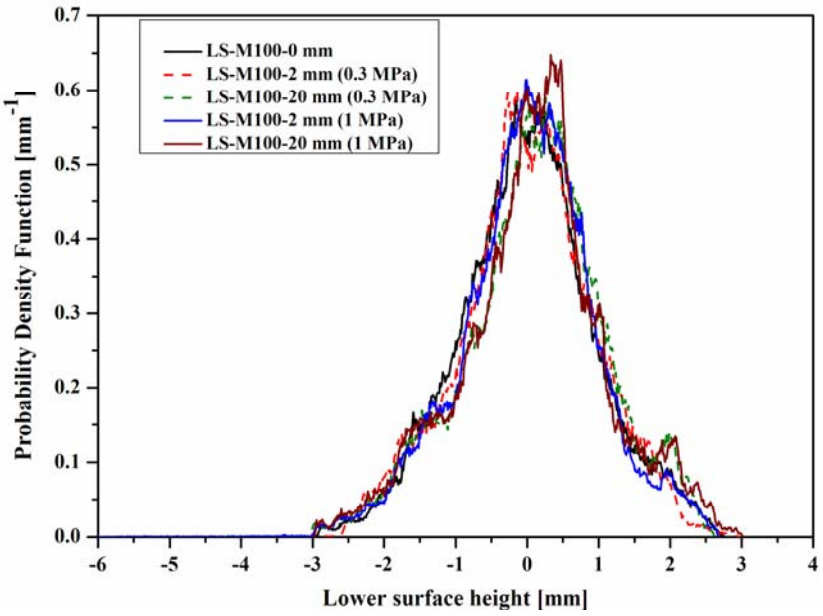

Fig. 5.6. Probability density function of the lower surface height of M100 as a function of normal stress and shear displacement.

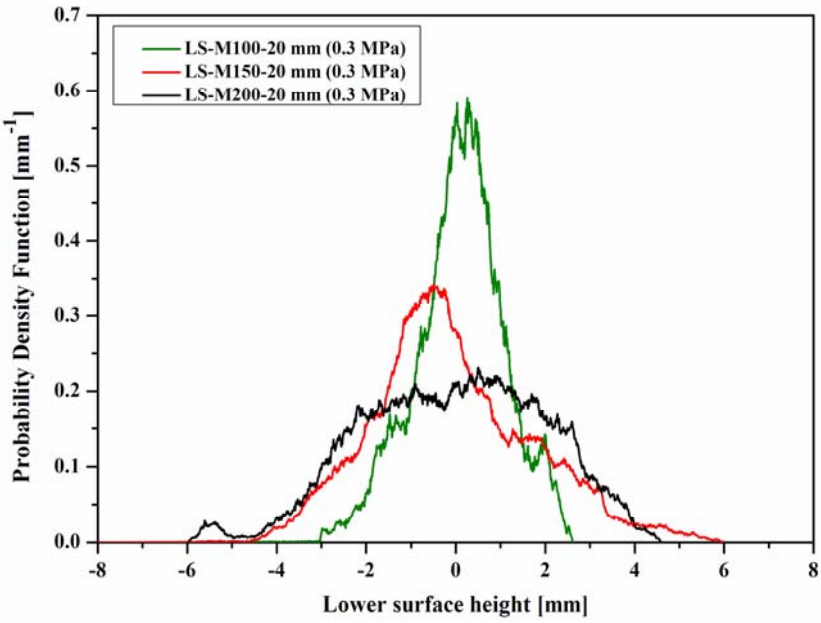

Fig. 5.7. Probability density function of the lower surface height of M100, M150 and M200 as a function of fracture size.

5.3.2 Standard deviation of mortar surface height

The effects of fracture size and normal stress on the SDs of the surface height for both upper (US) and lower (LS) surfaces are summarized in Table 5.3 to Table 5.5 for all shear displacements. For better understanding the effect of size and stress on the obtained data, a relation between the average SD of the surface height and shear displacement is shown in Fig. 5.8. Clearly, the damage increases as normal stress increases, and hence the SD of the surface height decreases with normal stress. Furthermore, the damage of the fracture surface decreases with decreasing fracture size.

Table 5.3. Fracture size, size of measurement area and SD of the surface height of M200.

σ_n MPa	δ_s mm	Fractured size mm	Measured area mm	SD (US) mm	SD (LS) mm
NA	0	200 × 200	175.1 × 180	1.926	1.998
0.3	2		175.1 × 178	1.897	1.963
	20		175.1 × 159.5	1.848	2.011
1	2		175.1 × 178	1.902	1.966
	20		175.1 × 159.5	1.697	1.930

Table 5.4. Fracture size, size of measurement area and SD of the surface height of M150.

σ_n MPa	δ_s mm	Fractured size mm	Measured area mm	SD (US) mm	SD (LS) mm
NA	0	150 × 150	136.5 × 142.7	1.876	1.826
0.3	2		136.5 × 141.0	1.864	1.832
	20		136.5 × 122.8	1.712	2.00
1	2		136.5 × 141.0	1.869	1.803
	20		136.5 × 122.8	1.801	1.804

Table 5.5. Fracture size, size of measurement area and SD of the surface height of M100.

σ_n MPa	δ_s mm	Fractured size mm	Measured area mm	SD (US) mm	SD (LS) mm
NA	0	100 × 100	85.1 × 91.6	0.948	0.950
0.3	2		85.1 × 90.5	0.957	0.942
	20		85.1 × 71.3	0.919	1.005
1	2		85.1 × 90.5	0.905	0.948
	20		85.1 × 71.3	0.872	1.018

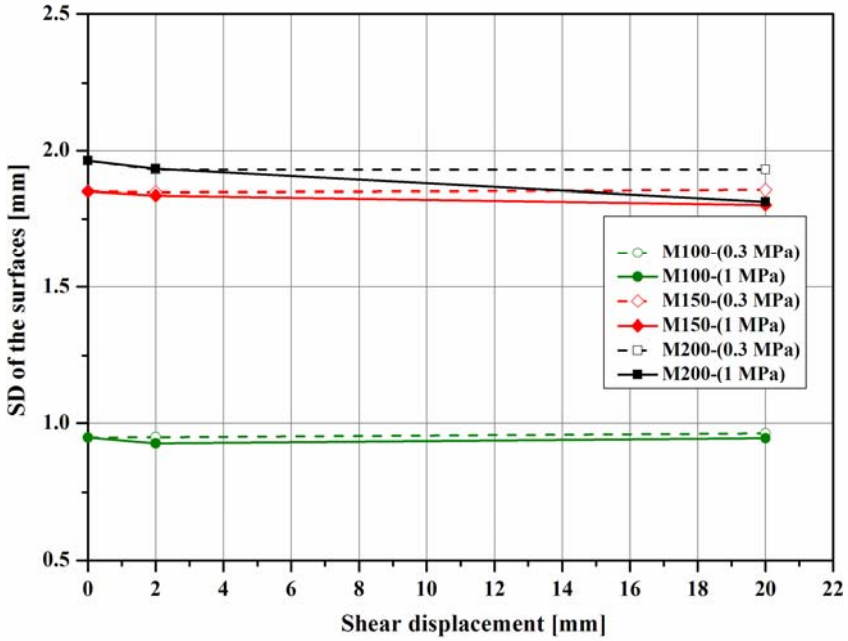

Fig. 5.8. Relation between shear displacement (δ_s) and the SD of the surface (σ_h) as a function of fracture size and normal stress.

5.3.3 Mean and the standard deviation of mortar aperture

The PDF of the initial aperture was determined from measured data. The PDF of the initial aperture for M100 at normal stresses of 0.3 and 1 MPa and shear displacements of 2 and 20 mm is shown in Fig. 5.9. The peak values of PDF decreases with normal stress for the same shear displacement and become broader. For each replica, the mean initial aperture and the SD of the initial aperture were determined, and summarized in Table 5.6 to Table 5.8.

To clarify the effect of fracture size and normal stress during shearing on the initial aperture, the SDs of the initial aperture were plotted against shear displacement, as shown in Fig. 5.10. It can be seen that the SD of the initial aperture increases with both normal stress and fracture size since the matedness between the two fracture surfaces decreases with fracture size and larger normal stress causes more damage on the asperities, which decrease the matedness of the fracture. Typical examples of the initial aperture distribution for M100 and M150 are shown as contour maps in Fig.5.11 and Fig. 5.12, respectively.

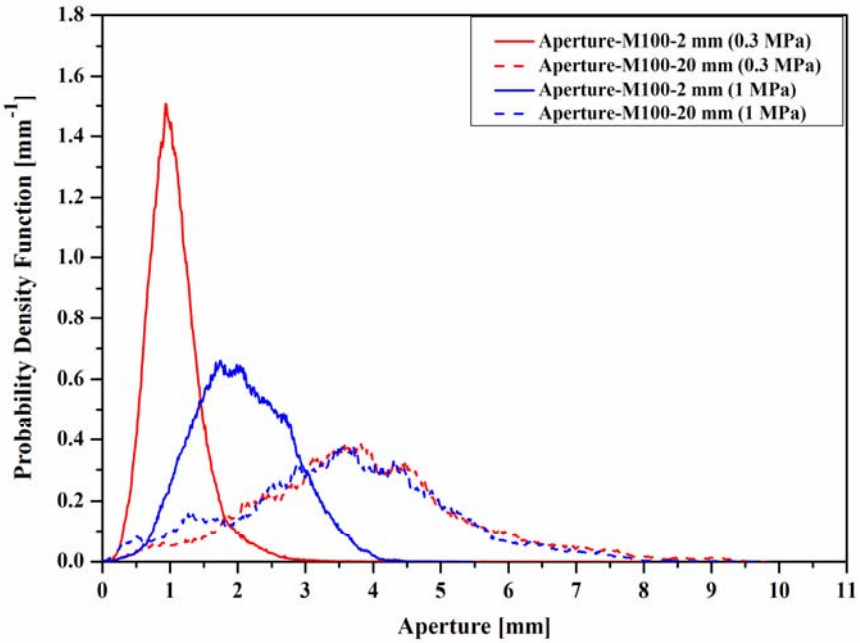

Fig. 5.9. Probability density function of the initial aperture of M100A as a function of normal stress.

Table 5.6. Fracture size, size of measurement area, mean aperture and SD of the initial aperture of M200.

σ_n MPa	δ_s mm	Fractured size mm	Measured area mm	Initial mean mm	SD mm
NA	0	200 × 200	175.1 × 180	3.717	0.583
0.3	2		175.1 × 178	2.493	0.659
	20		175.1 × 159.5	5.954	1.840
1	2		175.1 × 178	3.339	1.052
	20		175.1 × 159.5	6.441	1.900

Table 5.7. Fracture size, size of measurement area, mean aperture and SD of the initial aperture of M150.

σ_n MPa	δ_s mm	Fractured size mm	Measured area mm	Initial mean mm	SD mm
NA	0	150 × 150	136.5 × 142.7	2.310	0.661
0.3	2		136.5 × 141.0	3.121	0.865
	20		136.5 × 122.8	4.937	1.686
1	2		136.5 × 141.0	3.010	0.985
	20		136.5 × 122.8	5.387	1.887

Table 5.8. Fracture size, size of measurement area, mean aperture and SD of the initial aperture of M100.

σ_n MPa	δ_s mm	Fractured size mm	Measured area mm	Initial mean mm	SD mm
NA	0	100 × 100	85.1 × 91.6	1.319	0.303
0.3	2		85.1 × 90.5	1.071	0.417
	20		85.1 × 71.3	3.582	1.528
1	2		85.1 × 90.5	2.081	0.714
	20		85.1 × 71.3	3.860	1.554

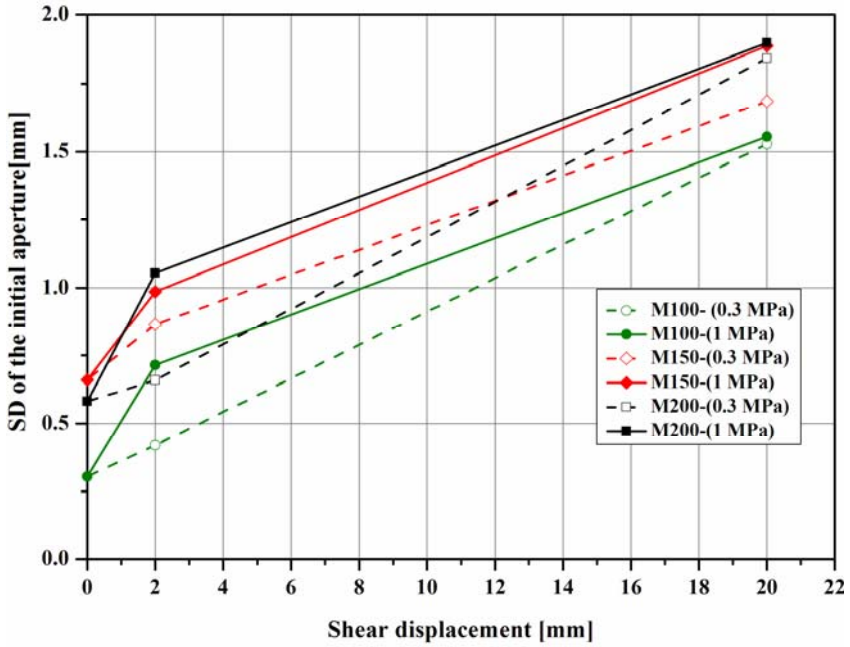

Fig. 5.10. Relation between shear displacement (δ_s) and the SD of the initial aperture (σ_0) as a function of normal stress and fracture size.

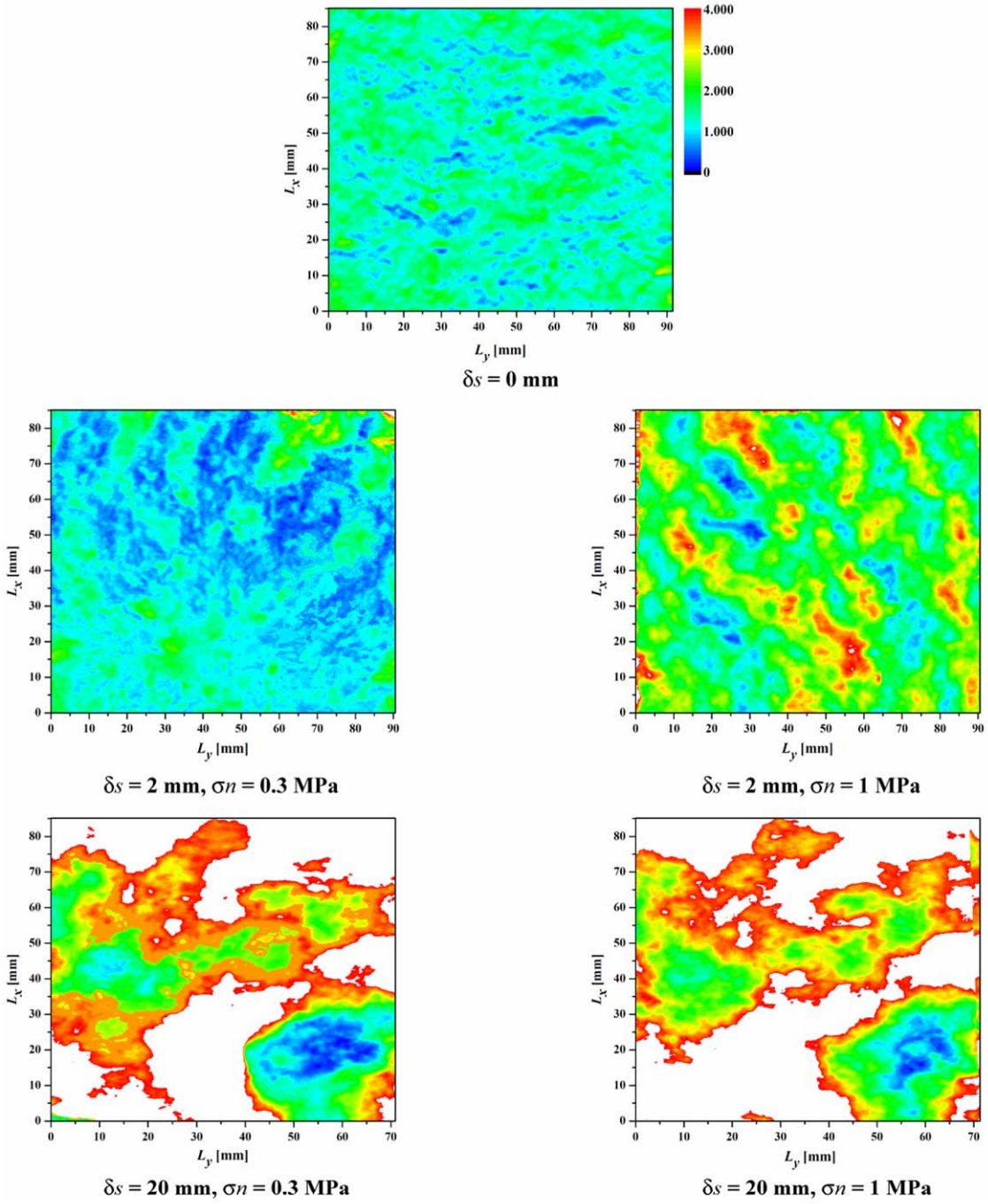

Fig. 5.11. Initial aperture distribution before and after shearing for M100.

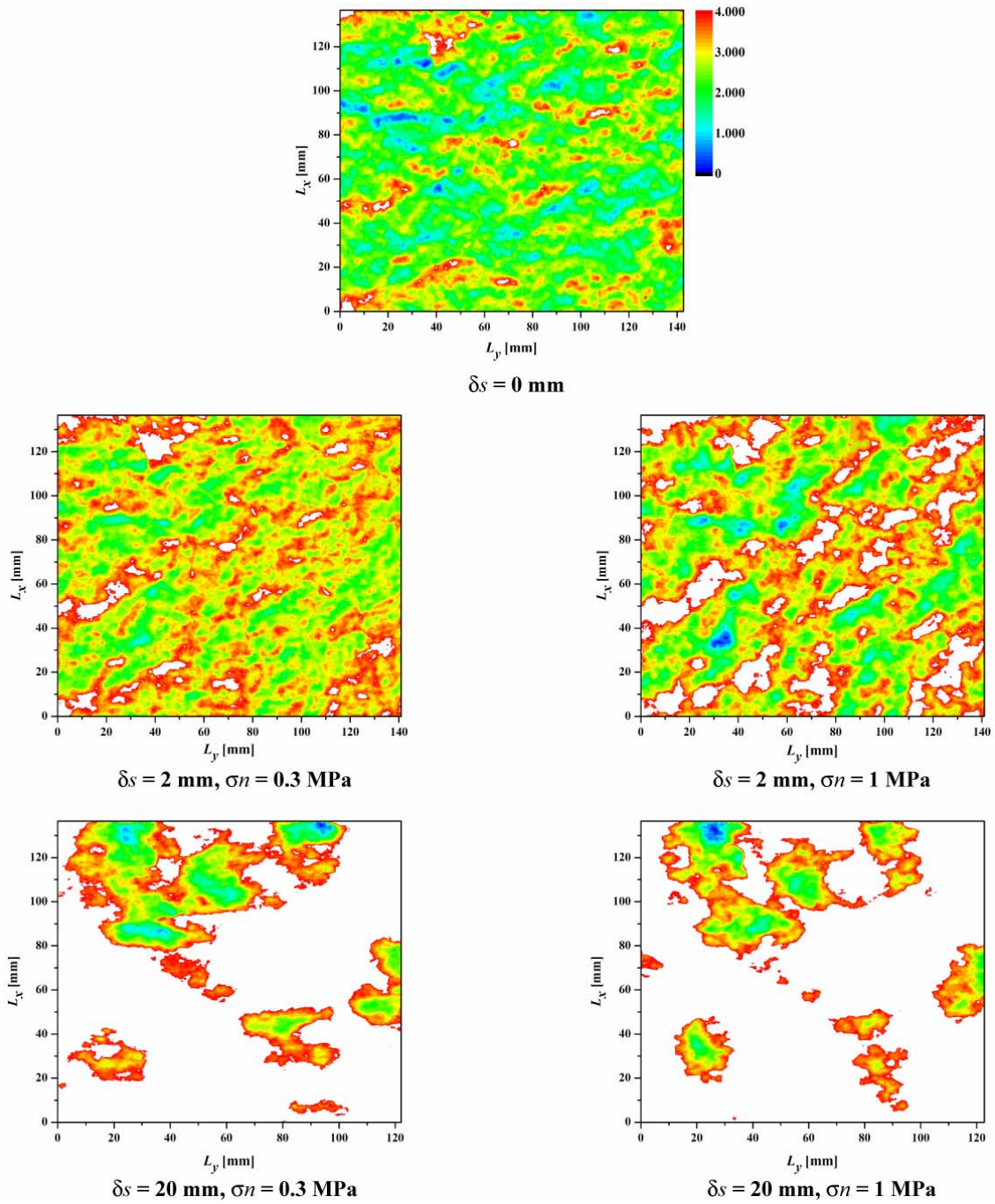

Fig. 5.12. Initial aperture distribution before and after shearing for M150.

5.3.4 Power spectral density of surface height and aperture

The PSDs of the surface height and the initial aperture at normal stresses of 0.3 and 1 MPa during shearing were calculated using a fast Fourier transform (FFT) and the PSDs are ensemble-averaged for each specimen. However, since the effect of shearing on the PSD was already discussed in chapter 4, only the effect of normal stress on the PSD is shown.

Fig. 5.13 shows PSD of the upper surface height at normal stresses of 0.3 and 1 MPa and shear displacements (δs) of 0 and 20 mm for M150. This figure shows that the smaller asperities with shorter wavelengths were more damaged by shearing at normal stress of 1 MPa. Furthermore, under a higher normal stress, the larger asperity with longer wavelengths seems to be damaged as well.

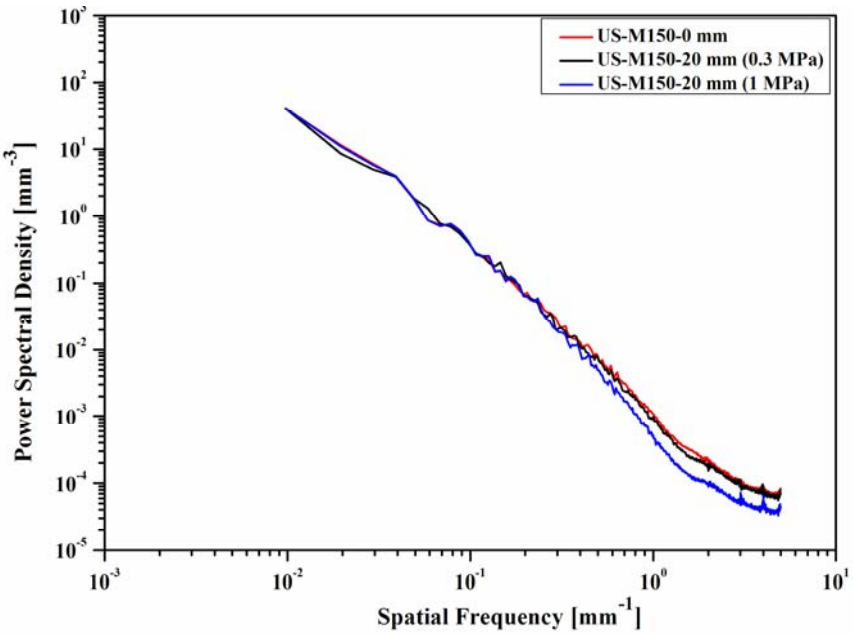

Fig. 5.13. Power spectral density of the upper surface height at normal stress of 0.3 and 1 MPa for shear displacements of 0 and 20 mm for M150.

5.4 Effect of stress and size on mechanical behaviors of mortar replica

In the previous chapter only the effect of fracture size was considered during the investigation of the mechanical behavior. However, normal stress should be considered as well because its strong influence on the shear behavior. Furthermore, one of the consequences of the asperities shearing is the generation of gouge materials between the sliding surfaces [149]. Although the gouge materials have a significant effect on the fracture behavior, especially the friction, shear strength and fluid transmissivity [33, 150, 151], progress in research on this subject has not been impressive for rock fracture. In fact, the difficulties lie in measuring the rate of gouge production, its distribution on the fracture surface, etc. Therefore, this contribution can be considered as a small step toward understanding and developing this aspect.

5.4.1 Closure curve and the effect of gouge on it

As mentioned earlier, the measurement was recorded at normal stresses of 0.3 and 1 MPa and shear displacements of 2 and 20 mm, while monotonic shear loading was conducted. Fig. 5.14 shows the effect of normal stress on the non-linearity of the closure for M100, M150 and M200 at shear displacement of 20 mm. Since the matedness decreases with normal stress, the non-linearity of the closure curve increase, except for M100 which seems to be a little different.

Fig. 4.15 shows the effect of gouge materials on the closure curve. Clearly, the non-linearity of the closure curve increases with gouge material/debris. This is mainly because the gouge is a soft material which can be easily deformed under the applied condition. Moreover, the non-uniformity distribution of the gouge material has great effects on the non-linearity of closure. In the previous simulation work [133], the gouge materials was not considered during the closure estimation, and thus closure was underestimated. It can be concluded that the effect of gouge material on the mechanical behavior should be considered, especially if a soft rock is used.

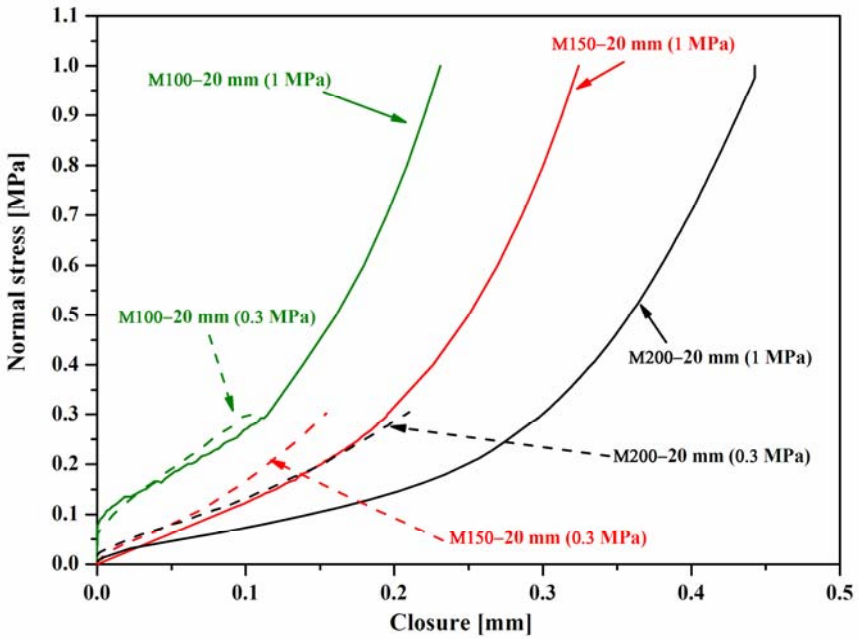

Fig. 5.14. Effect of normal stress on the closure curve for M100, M150 and M200.

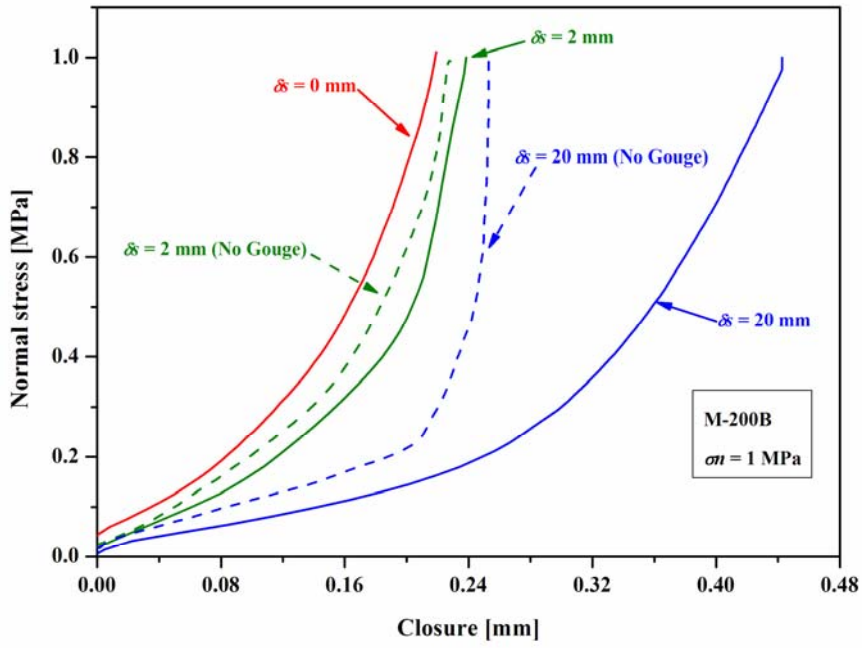

Fig. 5.15. Effect of the gouge materials on closure curve for M200 at 1 MPa.

5.4.2 Normal stiffness and the effect of gouge on it

The normal (k_n) stiffness is defined by Eq. 4.6. To investigate the effect of normal stress on the normal stiffness (k_n) with different shear displacements, k_n was estimated at normal stress of 0.2 MPa for all fractured specimens. Fig. 5.16 shows k_n decreases with increasing normal stress for M150 and M200. This is mainly due to the unmatedness increases with normal stress because of the damage on asperities. For the sake of comparison, the normal stiffness (k_n) was estimated with and without the presence of the gouge materials at normal stress of 0.2 MPa for M200, as shown in Fig. 5.17. Since the non-linearity of the closure curve increases with gouge material/debris, the k_n decreases with the presence of the gouge material.

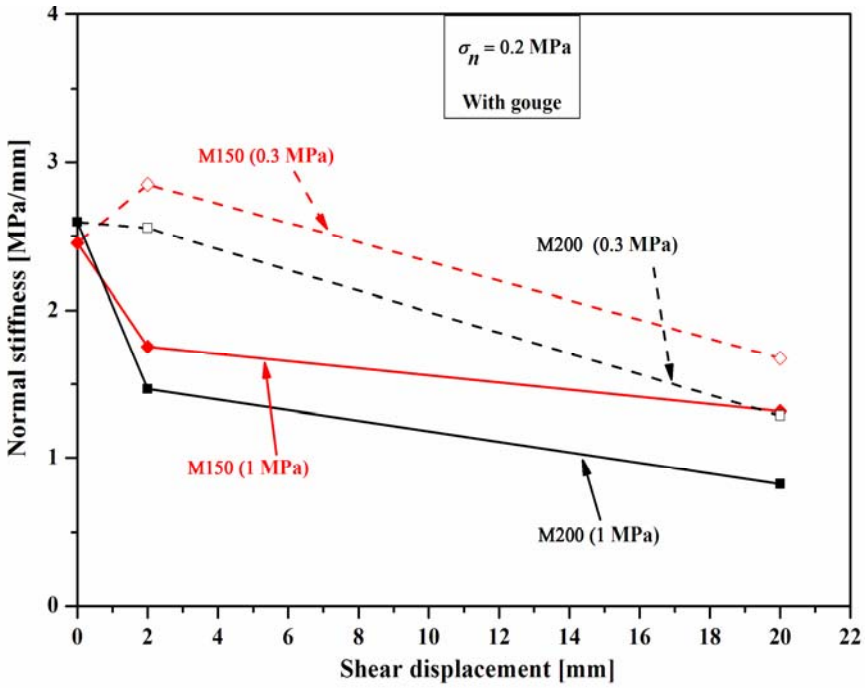

Fig. 5.16. Normal stiffness at normal stress at 0. 2 MPa for M150 and M200.

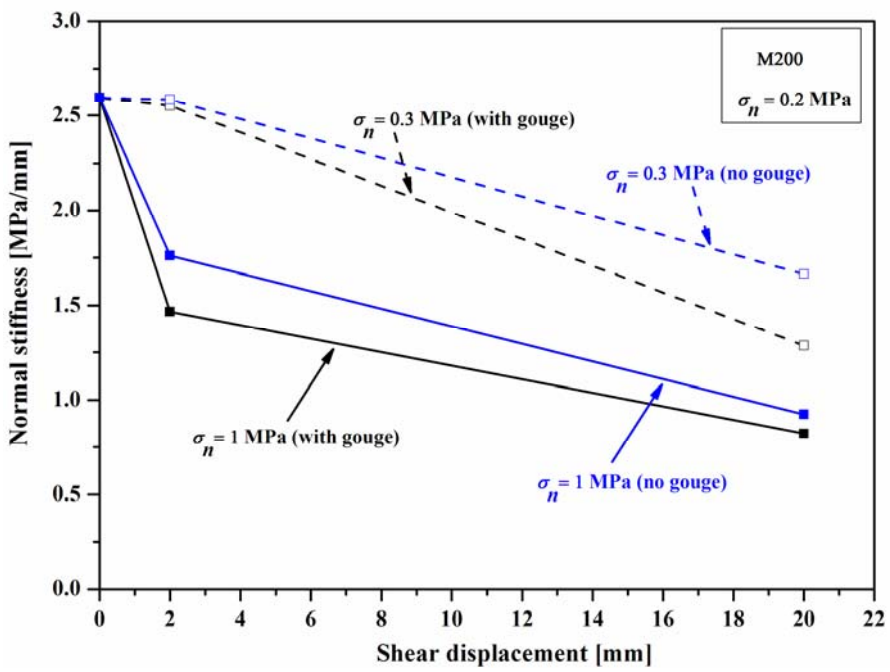

Fig. 5.17. Effect of gouge materials on normal stiffness at normal stress at 0. 2 MPa for M200.

5.5 Asperity degradation

When a rock fracture is subjected to shearing under normal and shear loads, both surfaces of the fracture are more or less damaged, and, the area of damaged zones depends on the magnitude of the applied normal stress [146]. To understand how the same surface changes with shearing under different normal stresses, fracture surfaces of the mortar replicas were measured before and after shear tests. Fig. 5.18 and Fig. 5.19 show the areas when the heights of the upper surface decreased after being sheared by 2 and 20 mm at normal stresses of 0.3 and 1 MPa for M100 and M150. Clearly, damaged zones were enlarged in the direction of the shear displacement and localized with shear displacement. Furthermore, for the same shear displacement, the number of damaged area is increased under a higher normal stress for this soft mortar.

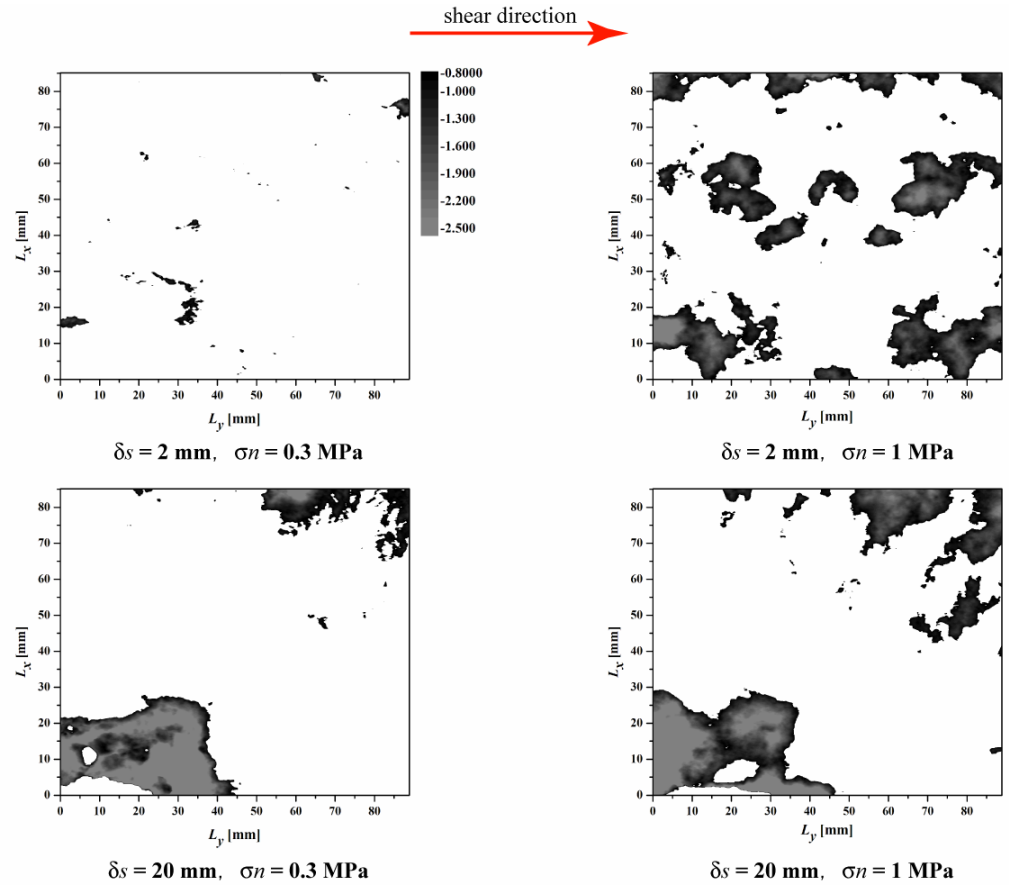

Fig. 5.18. Effect of shear displacement (δ_s) and normal stress (σ_n) on the damaged areas in the upper surface for M100.

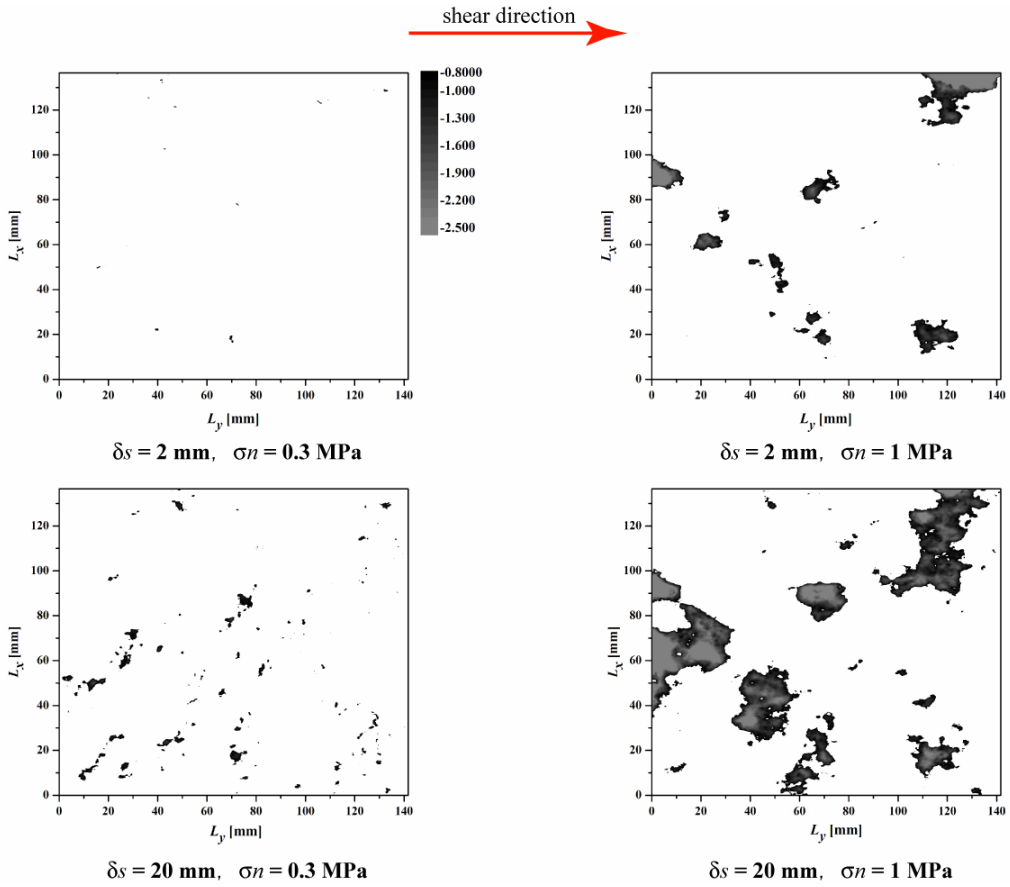

Fig. 5.19. Effect of shear displacement (δ_s) and normal stress (σ_n) on the damaged areas in the upper surface for M150.

5.6 Summary

In this chapter, mortar fracture replicas of sizes ranging from 100 mm to 200 mm were reproduced from a large tensile fracture that was created in Inada granite, to exclude the effect of the individual difference on the experimental results. The normal stress effect on the shear behavior of the fracture was experimentally investigated by performing monotonic shear loading under normal stresses of 0.3 and 1 MPa for shear displacements of 2 and 20 mm. The surface topography and the initial aperture were measured before and after shearing at the designated shear displacements by a laser profilometer. The main conclusion can be summarized as follows:

1) The SD of the initial aperture increases with normal stress since the matedness decreases due to the increase in the damage of the asperities as the normal stress increases.
2) The normal stiffness decreases with normal stress because the matedness decrease as the SD of the aperture increases with normal stress. Consequently, the non-linearity in the closure curve increases with normal stress.
3) The non-linearity of the closure increases with the gouge material. Therefore, the normal stiffness decreases with the presence of gouge material. Almost all numerical simulations have neglected the effect of gouge material produced by shear on the closure curve, and accordingly, the closure curve should have been underestimated.
4) The damaged zones are enlarged and localized with shear displacement. However, for the same shear displacement, the number of damaged area increases under a higher normal stress.

6. CONCLUSIONS

This work had the aim of clarifying the effects of size and normal stress on the shear behavior of a single fracture by utilizing the direct shear test. Therefore, both analytical and experimental investigations were performed. First, a 3D FEM analysis with quadratic joint elements as a fracture model was performed to examine the validity of the DST for a rock fracture by analyzing both the stress and deformation in fractured specimens of various sizes for a limited case of a set of normal and shear stresses (σ_n = 10 MPa and τ = 7 MPa). Then, a direct shear test apparatus including measuring devices, reference plates and matching bars were designed and developed.

Second, in order to study the effect of size and shear displacement on the shear behavior of a single facture, a tensile fracture was created in granite with sizes of 100 mm × 100 mm, 150 mm × 150 mm and 200 mm × 200 mm, and the direct shear tests were performed with a normal stress of 10 MPa. In this experiment, normal and shear stresses were unloaded at designated shear displacements and the change in the surface topography was measured by using a non-contact surface profile measurement system with a laser profilometer, to determine the evolution of surface damage and aperture during shear.

Finally, to clarify the effect of normal stress and gouge material on the shear behavior of a fracture, a tensile fracture in granite were reproduced by using mortar replicas with sizes of 100 mm × 100 mm, 150 mm × 150 mm and 200 mm × 200 mm, and the fracture replicas were tested in the direct shear test under two different values of normal stress (0.3 and 1 MPa) and shear displacements of 2 and 20 mm with and without cleaning the gouge materials that were produced during shear. The main results obtained in this work are summarized as follows:

1) Simulation analysis

- The non-uniformity of the traction distribution on the loading surfaces decreases as the specimen height decreases. Partial separation occupies only a small area in the loading surfaces and does not significantly affect the traction distributions or the mechanical behaviors of the fracture, for the values of the normal and shear stresses used in this study.
- The normal and shear stresses are significantly concentrated near the edges of the fracture, and are relatively uniform in the central part of the fracture. The concentrations of the normal and shear stresses in the fracture are much smaller than those in the intact specimen, since the fracture acts as a soft layer. Thus, the

stress concentrations in the residual stage are smaller than those in the initial stage.

- The stress concentrations decrease with a decrease in the specimen height, which can be attributed to the fact that the moment produced by the shear loads decreases with a decrease in the specimen height. The closure value is greater near the edges of the fracture where the normal stress is concentrated, and the concentration of closure increases with specimen height. However, this concentration of closure is not so significant due to the non-linear behavior of closure, i.e., closure does not significantly increase with normal stress at large normal stresses.
- Although the shear displacement is also greater near the edges of the fracture, the concentration of the shear displacement is much smaller than that of the closure since the shear stiffness increases with the normal stress.
- Based on this numerical investigation, a decision was made to use the smallest practical specimen height (h = 80 mm) throughout the experimental work since the height of 40 mm is too thin to avoid fracturing in the specimen when a normal stress is applied to the upper and lower surfaces.

2) Effect of size and shear displacement on the shear behavior of a facture

- The SD of the initial aperture increases with both shear displacement and fracture size. As a result, the closure curve tends to become more non-linear with shear displacement since the matedness of the fracture surfaces decreases with shear displacement. Thus, shear dilation is not only governed by the surfaces sliding over, but the increase in the non-linearity of the closure curve with shear displacement also has significant effects on shear dilation.
- The normal and shear stiffnesses in the initial stage decrease with fracture size because the matedness decreases as the SD of the initial aperture increases with fracture size. However, the shear stiffness in the residual stage increases with fracture size. This can be attributed to the fact that only small asperities with short wavelengths are mainly damaged by shear, as indicated by the change in the PSD of the surface heights during shear.
- Contact area gradually decreases during shearing due to the shear-offset. However, the distribution of the contact area is locally expanded with shear displacement.
- The damaged zones are enlarged and localized with shear displacement, and tend to form perpendicular to the shear displacement.

3) Effect of normal stress and the gouge material on the shear behavior of a fracture

- The SD of the initial aperture increases with normal stress since the matedness

decreases due to the increase in the damage of the asperities as the normal stress increases.

- The normal stiffness decreases with normal stress because the matedness decreases as the SD of the aperture increases with normal stress. Consequently, the non-linearity in the closure curve increases with normal stress.
- The non-linearity of the closure increases with the gouge material. Therefore, the normal stiffness decreases with the presence of gouge material. Almost all numerical simulations have neglected the effect of gouge material produced by shear on the closure curve, and accordingly, the closure curve obtained in the simulation should have been underestimated.
- The damaged zones are enlarged and localized with shear displacement. However, for the same shear displacement, the number of damaged area increases under a higher normal stress.

ACKNOWLEDGEMENTS

I would like to take this opportunity to express my deepest gratitude and appreciation to the people who have given me their assistance throughout my studies and during the preparation of this thesis. I would especially like to thank my advisor and committee chair ***Prof. Koji Matsuki*** for his continuous encouragement, and especially his academic and creative guidance. He has been my source for inspiration throughout my graduate studies.

I also wish to take this opportunity to thank and acknowledge my ***associate Prof. Kiyotoshi Sakaguchi***, who is my mentor and a guiding light in this research. I know in my heart that I would not be where I am today without the guidance I received from him.

I would also like to take this chance to thank the Ministry of Education, Culture, Sport, Science and Technology (***MEXT***), Japan, for giving me permission to pursue this study in Japan, as well as financial support (Grant No. 19360402).

I would like to thank ***Prof. Toshiyuki Hashida*** and ***Prof. Takatoshi Ito*** for serving as committee members, and I do very much indeed acknowledge their guidance and helpful comments while working toward my graduation.

I would like to thank ***Dr. Akihisa Kizaki*** for friendship and co-operation. I learned a lot from him I will continue our friendship forever.

Many thanks go to all the professors and staff of the ***Graduate School of Environmental Studies***. I appreciated them for their kindness every moment I spent at the school.

I would like to thank my dear mother and all my family, my wife ***Amna*** in particular, for enduring patience, and freeing me from other obvious duties to fully dedicate my time to study and research.

I am going to remember these years of hard work with the greatest pleasure. To all of you, I appreciate what you have done to help me during my stay in Japan. I consider myself lucky with lots of helping hands and cheerful friends around me all the time. I know I still have much to learn, but with continued support and encouragement from people like you (my friends) I know I can accomplish a great deal.

AUSAMA GIWELLI

SENDAI, AUGUST 2010

REFERENCES

[1] Gale JE. Comparison of coupled fracture deformation and fluid flow models with direct measurements of fracture pore structure and stress-flow properties. In: Proceedings of the 28th US Symposium on Rock Mechanics (USRMS). Balkema: Rotterdam, Tucson, AZ; 1987. p. 1213-22.

[2] Gentier S, Billaux D, Van Vliet L. Laboratory Testing of the voids of a fracture (Technical note). Rock Mech Rock Eng 1989;22:149-57.

[3] Hakami E. Aperture distribution of rock fractures. PhD. thesis, Division of Engineering Geology, Royal Institute of Technology (KTH), Stockholm, Sweden, 1995.

[4] Iwano M, Einstein HH. Laboratory experiments on geometric and hydromechanical characteristics of the three different fractures in grandiorite In: Proceedings of the 8th International Congress on Rock Mechanics. Japan; 1995 p. 743-50.

[5] Brown SR. Fluid flow through rock joints: the effect of surface roughness. J Geophys Res 1987;92:1337-47.

[6] Bandis S, Lumsden AC, Barton NR. Experimental studies of scale effects on the shear behaviour of rock joints. Int J Rock Mech Min Sci & Geomech Abstr 1981;18:1-21.

[7] Tanoli SK, Stesky RM. An experimental study of the mechanics of fracture closure. Geol Bull Univ Peshawar 1987;20:77-97.

[8] Matsuki K, Lee JJ, Sakaguchi K. Size effect in flow conductance of a closed small-scale hydraulic fracture in granite. Geotherm Sci & Tech 1999; 6:113-38.

[9] Raven KG, Gale JE. Water flow in a natural rock fracture as a function of stress and sample size. Int J Rock Mech Min Sci & Geomech Abstr 1985;22(4):251-61.

[10] Yoshinaka R, Yamabe T. Joint stiffness and the deformation behavior of discontinuous rock. Int J Rock Mech Min Sci 1986;23(1):19-28.

[11] Fardin N. The effect of scale on the morphology, mechanics and transmissivity of single rock fractures PhD thesis, Department of land and water resources engineering, Royal Institute of Technology (KTH), Stockholm, Sweden, 2003.

[12] Marache A, Riss J, Gentier G. Experimental and modelled mechanical behavior of a rock fracture under normal stress. Rock Mech Rock Eng 2008;41:869-92.

[13] Giwelli AA, Sakaguchi K, Matsuki K. Experimental study of the effect of fracture size on closure behavior of a tensile fracture under normal stress. Int J Rock Mech Min Sci 2009;46:462-70.

[14] Goodman RE. Methods of geological engineering in discontinuous rocks. USA: West Publishing Company; 1976.

[15] Brown SR. Simple mathematical model of a rough fracture. J Geophys Res

1995;100:5941-52.

[16] Glover PWJ, Matsuki K, Hikima R, Hayashi K. Synthetic rough fractures in rocks. J Geophys Res 1998;103(B5):9609-20.

[17] Matsuki K, Chida Y, Sakaguchi K, Glover PWJ. Size effect on aperture and permeability of a fracture as estimated in large synthetic fractures. Int J Rock Mech Min Sci 2006;43:726-55.

[18] Sakaguchi K, Tomono J, Okumura K, Ogawa Y, Matsuki K. Asperity height and aperture of a artificial tensile fracture of metric size. Rock Mech Rock Eng 2008;41(2):325-41.

[19] Yoshinaka R, Yoshida J, Shimizu T, Arai H, Arisaka S. Scale effect in shear strength and deformability of rock joints. In: Proceedings of the 7th ISRM congress on rock mechanics. Aachen, Germany; 1991. p. 371-4.

[20] Yoshinaka R, Arisaka S, Sasaki K, Yoshida J. Mechanism of scale effect in rock joint. In: Proceedings of the international workshop on rock foundation. Yoshinaka & kikuchi (eds), Tokyo, Japan; 1995. p. 223-8.

[21] Lanaro F. Geometry, Mechanics and Transmissivity of rock fractures. PhD thesis, Department of civil and environmental engineering, Royal Institute of Technology (KTH), Stockholm, Sweden, 2001.

[22] Pyrak-Nolte LJ, Myer LR, Cook NGW, Witherspoon PA. Hydraulic and mechanical properties of nature fractures in low permeability rock. In: Proceedings of the 6th International Congress on Rock Mechanics. Canada; 1987. p. 225-31

[23] Hakami E, Lannaro E. Aperture measurements and flow experiments on a single natural fracture. Int J Rock Mech Min Sci & Geomech Abstr 1996;33 (4): 395-404.

[24] Hakami E, Barton N. Aperture measurement and flow experiments using transparent replicas of rock joints. In: Proceedings of the rock joints. Leon, Norway; 1990. p. 383-90.

[25] Gentier S, Hopkins DL. Mapping fracture aperture as a function of normal stress using a combination of casting, image analysis and modeling. Int J Rock Mech Min Sci 1997;34 (Paper No. 132):3-4.

[26] Yeo IW, Freitas DMH, Zimmerman RW. Effect of shear displacement on the aperture and permeability of a rock fracture. Int J Rock Mech Min Sci 1998;35(8):1051-70.

[27] Kostakis K, Harrison JP, Heath SM. Silicone rubber castings for aperture measurement of rock fractures (Technical note). Int J Rock Mech & Min Sci 2003;40:939-45.

[28] Jafari MK, Pellet F, Boulon M, Hosseini KA. Experimental study of mechanical behavior of rock joints under cyclic loading. Rock Mech Rock Eng 2004;37(1):3-23.

[29] Lawrence WT. Permeability changes during shear deformation of fractured rock. In: Proceedings of the 28th US symposium on rock mechanics. Tucson, AZ; 1987. p. 473-80.

[30] Lamas LN. An experimental study of the hydromechanical properties of granite joints. In: Proceedings of the 8th international congress on rock mechanics ISRM, Tokyo, Japan; 1995. p.

733-8.

[31] Watanabe N, Hirano N, Tsuchiya N. Diversity of channeling flow in heterogeneous aperture distribution inferred from integrated experimental-numerical analysis on flow through shear fracture in granite. J Geophys Res 2009;114:1-17.

[32] Sakaguchi K, Goto M, Matsuki K. Experimental study of heterogeneous water flow in a sheared fracture. In: Proceedings of the 44th US rock mechanics symposium. Salt lake city, USA; 2010. p. 1-8, ARMA 10-315.

[33] Abola MP, Mohanty S, Makurat A. Coupled mechanical shear and hydraulic flow behavior of natural rock joints. In: Stephansson O, Jing L and Tsang CF, (editor). Coupled Thermo-hydro-mechanical Processes of Fractured Media (Developments in Geotechnical Engineering): Elsevier; 1996. 79, p. 393-423.

[34] Goodman RE, Ohnishi Y. Undrained shear testing of jointed rock. Rock Mechanics 1973;5(3):129-49.

[35] Jing L, Nordlund E, Stephansson O. An experimental study on the anisotropy and stress-dependency of the strength and deformability of rock joints. Int J Rock Mech Min Sci & Geomech Abstr 1992;29(6):535-42.

[36] Afidi AJ, Kwon S, Wilson WJ. Investigation of rock failure in a direct shear machine. Institution of Mining and Metallurgy 2001;110:158-62.

[37] Cresswell AW, Barton ME. Direct shear tests on an uncemented and a very slightly cemented locked sand. Quart J Eng Geol & Hydro 2003;36:119-32.

[38] Dermot M. Ross-Brown, Geoffrey W. A portable shear box for testing rock joints. Rock Mech Rock Eng 1975;7:129-53.

[39] Crawford AM, Curran JH. The influence of shear velocity on the frictional resistance of rock discontinuities. Int J Rock Mech Min Sci & Geomech Abstr 1981;18:505-15.

[40] Boulon M. A 3D direct shear device for testing the mechanical behaviour and hydraulic conductivity of rock joints. In: Proceedings of mechanics of jointed and faulted rock. Rossmanith: Balkema, Austria; 1995. p. 407-13.

[41] Esaki T, Nakahara K, Jiang Y, Kimura T, Mitani Y. shear-flow coupling properties of rock joints. In: Proceedings of the 8th international congress on rock mechanics Tokyo, Japan; 1995. p. 739-42.

[42] Indraratna B, Haque A. Experimental study of shear behavior of rock joints under constant normal stiffness conditions. Int J Rock Mech & Min Sci 1997;34:3-4 (paper No. 141).

[43] Esaki T, Du S, Mitani Y, Ikusada K, Jing L. Development of a shear-flow test apparatus and deformation of coupled properties for a single rock joint. Int J Rock Mech Min Sci 1999;36:461-650.

[44] Lee HS, Park YJ, Cho TF, You KH. Influence of asperity degradation on the mechanical

behavior of rough rock joints under cyclic shear loading. Int J Rock Mech & Min Sci 2001;38:967-80.

[45] Olsson R, Barton N. An improved model for hydromechanical coupling during shearing of rock joints. Int J Rock Mech & Min Sci 2001;38:317-29.

[46] Lee HS, Cho TF. Hydraulic characteristics of rough fractures in linear flow under normal and shear load. Rock Mech Rock Eng 2002;35(4):299-318.

[47] Hans J, Boulon M. A new device for investigating the hydro-mechanical properties of rock joints. Int J Numer Anal Meth Geomech 2003;27:513-48.

[48] Jiang Y, Xiao J, Tanabashi Y, Mizokami T. Development of an automated servo-controlled shear apparatus applying a constant normal stiffness condition. Int J Rock Mech Min Sci 2004;41:275-86.

[49] Nakagawa M, Jiang Y, Kawakita M, Yamada Y, Akiyama Y. Evaluation of mechanical properties of natural rock joints for discontinuous numerical analysis. In: Proceedings of the 3rd ARMS. Ohnishi & Aoki (eds), Kyoto, Japan; 2004. p. 989-94.

[50] Jiang Y, Bo Li, Tanabashi Y. Estimating the relation between surface roughness and mechanical properties of rock joints. Int J Rock Mech Min Sci 2006;43:837-46.

[51] Bo Li. Coupled shear-flow and deformation properties of fractured rock mass. PhD thesis, Graduate school of science and tenchnology, Nagasaki University, Nagasaki, Japan, 2009.

[52] Barton N. A relationship between joint roughness and joint shear strength. In: Proceedings of the international symposium on rock mechanics. Nancy, France 1971. p. 1-18.

[53] Goodman RE. Introduction to rock mechanics. New York: John Wiley & Snos; 1980.

[54] Barton N. Review of a new shear-strength criterion for rock joints. Eng Geol 1973;7:287-332.

[55] Barton N. Rock mechanics review: the shear strength of rock and rock joints. Int J Rock Mech Min Sci & Geomech Abstr 1976;13:255-79.

[56] Barton N, Choubey V. The shear strength of rock joints in theory and practice. Rock Mechanics 1977;10:1-54.

[57] Krahn J, Morgenstern NR. The ultimate frictional resistance of rock discontinuities. Int J Rock Mech Min Sci & Geomech Abstr 1979;16:127-33.

[58] Tse R, Cruden DM. Estimating joint roughness coefficients. Int J Rock Mech Min Sci & Geomech Abstr 1979;16:303-7.

[59] Bandis S, Lumsden AC, Barton NR. Fundamentals of rock joint deformation. Int J Rock Mech Min Sci & Geomech Abstr 1983;20(6):249-68.

[60] Swan G. Determination of stiffness and other joint properties from roughness meaurements. Rock Mech Rock Eng 1983;16:19-38.

[61] Barton N, Bandis S, Bakhtar K. Strength, deformation and conductivity coupling of rock

joints. Int J Rock Mech Min Sci & Geomech Abstr 1985;22(3):121-40.
[62] Brown SR, Scholz CH. Broad bandwidth study of the topography of natural rock surfaces. J Geophys Res 1985;90(B14):12575-82.
[63] Swan G, Zongqi S. Prediction of shear behavior of joints using profiles. Rock Mech Rock Eng 1985;18:183-212.
[64] Lee YH, Carr JR, Barr DJ, Haas CJ. The fractal dimension as a measure of the roughness of rock discontinuity profiles. Int J Rock Mech Min Sci & Geomech Abstr 1990;27(6):453-64.
[65] Maerz NH, Franklin JA, Bennett CP. Joint roughness measurement using shadow profilometry. Int J Rock Mech Min Sci & Geomech Abstr 1990;27(5):329-43.
[66] Maerz NH, Franklin JA. Roughness scale effects and fractal dimension. In: Proceedings of the 1st international workshop on scale effects in rock masses. A. Pinto da Cunha, Loen, Norway; 1990. p. 121-6.
[67] Power WL, Tullis TE. Euclidean and fractal models for the description of rock surface roughness. J Geophys Res 1991;96(B1):415-24.
[68] Durham WB, Bonner BP. Peak: a new kind of surface microscope (Technical note). Int J Rock Mech Min Sci & Geomech Abstr 1993;30(7):699-702.
[69] Odling NE. Natural fracture profiles, fractal dimension and joint roughness coefficients. Rock Mech Rock Eng 1994;27(3):135-53.
[70] Maksimovic M. The shear strength components of a rough rock joint. Int J Rock Mech Min Sci & Geomech Abstr 1996;33(8):769-83.
[71] National Research Council. Rock fractures and fluid flow: contemporary understanding and applications: National Academies Press; 1996.
[72] Roko RO, Daemen JJK, Myers DE. Variogram characterization of joint surface morphology and asperity deformation during shearing. Int J Rock Mech & Min Sci 1997;34(1):71-84.
[73] Power WL, Durham WB. Topography of natural and artificial fractures in granite rocks: implications for studies of rock friction and fluid migration. Int J Rock Mech & Min Sci 1997;34(6):979-89.
[74] Shirono T, Kulatilake PHSW. Accuracy of the spectral method in estimating fractal/spectral parameters for self-affine roughness profiles. Int J Rock Mech & Min Sci 1997;34(5):789-804.
[75] Xie H, Wang JA, Xie WH. Fractal effects of surface roughness on the mechanical behavior of rock joints. Chaos, Solitons & fractal 1997;8(2):221-52.
[76] Yang ZY, Chen GL. Application of the self-affinity concept to the scale effect of joint roughness. Rock Mech Rock Eng 1999;32(3):221-9.
[77] Indraratna B, Haque A. Shear behavior of rock joints. Netherlands: A.A. Balkema,

Potterdam 2000.

[78] Fardin N, Jing L, Stephansson O. Heterogeneity and anisotropy of roughness of rock joints. In: Proceedings of the eurock 2001, Rrock mechanics- a challenge for society. Särkkä & Eloranta (eds), Espoo, Finland; 2001. p. 223-7.

[79] Grasselli G. Shear strength of rock joints based on quantified surface description. PhD thesis, Rock mechanics, Swiss Federal Institute of Technology of Lausanne (EPFL), Lausanne, Switzerland, 2001.

[80] Grasselli G, Wirth J, Egger P. Quantitive three-dimensional description of a rough surface and parameter evolution with shearing. Int J Rock Mech & Min Sci 2002;39:789-800.

[81] Feng Q, Fardin N, Jing L, Stephansson O. A new method for in-situ non-contact roughness measurement of large rock facture surfaces. Rock Mech Rock Eng 2003;36(1):3-25.

[82] Jing L, Hudson JA. Fundamentals of the hydro-mechanical behavior of rock fractures: roughness characterization and experimental aspects. In: Proceedings of the sinorock 2004. Elsevier (Int J Rock Mech Min Sci), China; 2004. p. 1-6, CD-ROM (paper 1A 26).

[83] Son BK, Lee YK, Lee CI. Elasto-plastic simulation of direct shear test on rough rock joints. In: Proceedings of the sinorock 2004. Elsevier (Int J Rock Mech Min Sci), China; 2004. p. 1-6, CD-ROM (paper 2A 07).

[84] Unal M, Unver B. Characterization of rock joint surface degradation under shear loads. In: Proceedings of the sinorock 2004. Elsevier (Int J Rock Mech Min Sci), China; 2004. p. 1-6, CD-ROM (paper 1A 24).

[85] Kulatilake PHSW, Balasingam P, Park J, Morgan R. Natural rock joint roughness quantification through fractal techniques. Geotech Geol Eng 2006;24:1181-202.

[86] Mlynarczuk M. Description and classification of rock surfaces by means of laser profilometry and mathematical morphology. Int J Rock Mech & Min Sci 2010;47(1):138-49.

[87] Jing L, Stephansson O. fundamentals of discrete element methods for rock engineering: theory and application: Elsevier; 2007.

[88] Witherspoon PA, Amick CH, Gale JE, Iwai K. Observations of a potential effect in experimental determination of the hydraulic properties of fractures. Water Resour Res 1979;15(5):1142-6.

[89] Barton N, Bandis S. Some effects of scale on the shear strength of joints (Technical note). Int J Rock Mech Min Sci & Geomech Abstr 1980;17:69-73.

[90] Baecher GB, Einstein HH. Size effect in rock testing. Geophys Res Lett 1981;8(7):671-4.

[91] Barton N, Bandis S. Effect of block size on the shear behavior of jointed rock. In: Proceedings of the 23rd symposium on rook mechanics (Keynote Lecture). The University of California, Berkeley, California; 1982. p. 739-60.

[92] Long JCS, Remer JS, Wilson CR, Witherspoon PA. Porous media equivalents for networks

of discontinuous fractures. Water Resour Res 1982;18(3):645-58.

[93] Tsang YW, Witherspoon PA. The dependence of fracture mechanical and fluid flow properties on fracture roughness and sample size. J Geophys Res 1983;88(B3):2359-66.

[94] Barton N. Scale effects or sampling bias? In: Proceedings of the 1st international workshop on scale effects in rock masses. Loen, Norway; 1990. p. 31-55.

[95] Chappell BA. Size effects, stress and couple stress gradients in jointed rock. Mining Science and Technology 1990;11:1-18.

[96] Kulatilake PHSW, Wang S, Stephansson O. Scale effects on the deformability of jointed rock at the three-dimensional level. In: Proceedings of the 2nd international workshop on scale effects in rock masses. Pinto da Cunha (eds), Lisbon, Portugal; 1993. p. 265-76.

[97] Moon HK, Jue KS, Song MK. Estimation of the mechanical, thermal and hydraulic properties of jointed rock masses and their scale effect In: Proceedings of the 8th international congress on rock mechanics. Tokyo, Japan; 1995. p. 715-9.

[98] Vermilye JM, Scholz CH. Relation between vein length and aperture. J Struct Geol 1995;17(3):423-34.

[99] Bhasin R, Hoeg K. Numerical modelling of block size effects and influence joint properties in multiply jointed rock. Tunnelling and Underground Space Technology 1997;12(3):407-15.

[100] Renshaw CE, Park JC. Effect of mechanical interactions on the scaling of fracture length and aperture. Nature 1997;386:482-4.

[101] Castelli M, Re F, Scavia C, Zaninetti A. Experimental evaluation of scale effects on the mechanical behavior of rock joints. In: Proceedings of the eurock 2001, Rock mechanics- a challenge for society. Särkkä & Eloranta (eds), Espoo, Finland; 2001. p. 205-10.

[102] Matsuki K, Fukuoka N, Tomono J, Sakaguchi K. Size effect on fracture permeability estimated by using synthetic fractal fracture (In Japanese with English abstract). J Geotherm Res Soc Japan 2001;23(2):127-39.

[103] Thuro K, Plinninger RJ, Zah S, Schutz S. Scale effects in rock strength properties. Part 1: Unconfined compressive test and Brazilian test. In: Proceedings of the eurock 2001, Rock mechanics- a challenge for society Särkkä & Eloranta (eds), Espoo, Finland; 2001. p. 169-74.

[104] Thuro K, Plinninger RJ. Scale effects in rock strength properties. Part 2: point load test and point load strength index. In: Proceedings of the eurock 2001, Rock mechanics- a challenge for society. Särkkä & Eloranta (eds), Espoo, Finland; 2001. p. 175-80.

[105] Szymakowski JB, Haberfield CM. Direct shear testing of large, jointed, soft rock masses-preliminary results. In: Proceedings of the eurock 2001, Rock mechanics- a challenge for society. Särkkä & Eloranta (eds), Espoo, Finland; 2001. p. 307-12.

[106] Vallier F, Mitani Y, Esaki T, Boulon M. Development of a new shear model for rock joints, application to scale effect. In: Proceedings of the 3rd ARMS. Ohnishi & Aoki (eds), Kyoto,

Japan; 2004. p. 983-8.

[107] Giwelli A, Sakaguchi K, Matsuki K. Scale effect on closure of a tensile fracture under normal stress. In: Proceedings of the 5th international workshop on water dynamics. Sendai, Japan; 2007. p. 39-45.

[108] Giwelli AA. Experimental study of size effect on closure of a tensile fracture under normal stress. Ms thesis, Graduate School of Environmental Studies, Tohoku University, Sendai, Japan, 2007.

[109] Baghbanan A. Scale and stress effects on hydro-mechanical properties of fractured rock massed. PhD thesis, Department of land and water resources engineering, Royal Institute of Technology (KTH), Stockholm, Sweden, 2008.

[110] Hencher SR, Toy JP, Lumsden AC. Scale dependent shear stength of rock joints. In: Proceedings of the 2nd international workshop on scale effects in rock masses. A. Pinto da Cunha, Lisbon, Portugal; 1993. p. 233-40.

[111] Matsuki K, Sakaguchi K, Inoue Y. Analysis of shear dilation and permeability of a hydraulic fracture in granite. In: Proceedings of the 9th international congress on rock mechanics. G. Vouille & P. Berest, Paris, France; 1990. p. 765-8.

[112] Fardin N, Stephansson O, Jing L. Scale effect on the geometrical and mechanical properties of rock joints. In: Proceedings of the 10th congress technology roadmap for rock mechanics. South African 2003a. p. 319-24.

[113] Fardin N, Stephansson O, Jing L. The scale dependence of rock joint surface roughness. Int J Rock Mech & Min Sci 2001;38:659-69.

[114] Liu SH. Simulating a direct shear box test by DEM. Can Geotech J 2006;43(2):155-68.

[115] Potts DM, Dounias GT, Vaughan PR. Finite element analysis of the direct shear test. Geotechnique 1987;37(1):11-23.

[116] Zhang L, Thornton C. A numerical examination of the direct shear test. Geotechnique 2007;57(4):343-54.

[117] Johannes H, Jin YO. Experiments and simulation of direct shear tests: porosity, contact friction and bulk friction. Granular Matter 2008;10:263-71.

[118] Matusoka H, Liu S. Simplified direct box shear test on granular materials and its application to rockfill materials. Soils Found 1998;38(4):275-84.

[119] Schneider HJ. The laboratory direct shear test-an analysis and geotechnical evaluation. Bull Int Assoc Eng Geo 1978;18:121-6.

[120] Fardin N. Influence of structural non-stationarity of surface roughness on morphological characterization and mechanical deformation of rock joints. Rock Mech Rock Eng 2008;41(2):267-97.

[121] Kutter HK. Stress distribution in direct shear test samples. In: Proceedings of the ISRM

Symposium, Mécanique des Roches. Nancy, France; 1971. p. II6-1-II6-12.
[122] Kusumi H, Tatsumi S, Matsuoka T, Ashida Y. Simulation analysis of shear behavior of rock joint by distinct element method. In: Proceedings of the ISRM international symposium 3rd ARMS. Kyoto, Japan; 2004. p. 1287-92.
[123] Karami A, Stead D. Asperity degradation and damage in the direct shear test: A hybrid FEM/DEM approach. Rock Mech Rock Eng 2008;41(2):299-66.
[124] Park JW, Song JJ. Numerical simulation of a direct shear test on a rock joint using a bonded-particle model. Int J Rock Mech Min Sci 2009;46:1315-28.
[125] Zienkiewizc OC. The finite element method in engineering sciences. New York, USA: McGraw-Hill; 1977.
[126] Pande GN, Beer G, Williams JR. Numerical methods in rock mechanics. New York, USA: Wiley; 1990.
[127] Wittke W. Rock mechanics-theory and applications. Berlin, Germany: Springer; 1990.
[128] Beer G, Watson JO. Introduction to finite boundary element method for engineers. New York, USA: Wiley; 1992.
[129] Goodman RE, Taylor RL, Brekke TL. A model for the mechanics of jointed rock. J Soil Mech Found Div, ASCE 1968;94(3):637-60
[130] Mitani Y, Esaki T, Nakashima Y. An experimental study on the anisotropy of flow in a rock joint. In: Proceedings of ISRM Regional Symposium on Rock Engineering. Seoul, Korea; 2002. p. 281-8.
[131] Matsuki K, Wang EQ, Sakaguchi K, Okumura K. Time-dependent closure of a fracture with rough surfaces under constant normal stress. Int J Rock Mech Min Sci 2001;38:607-19.
[132] Brown SR, Scholz CH. Closure of random elastic surfaces in contact. J Geophys Res 1985;90(B7):5531-45.
[133] Matsuki K, Wang EQ, Giwelli AA, Sakaguchi K. Estimation of closure of a fracture under normal stress based on aperture data. Int J Rock Mech Min Sci 2008;45:194-209.
[134] Matsuki K, Nakama S, Sato T. Estimation of regional stress by FEM for a heterogeneous rock mass with a large fault. Int J Rock Mech Min Sci 2009;46:31-50.
[135] Johnson KL. Contact mechanics. New York, USA: Cambridge University Press; 1985.
[136] Chryssanthakis P, Barton N. Joint roughness (JRCn) characterisation of a rock joint and joint replica at 1 m scale rock joints. In: proceedings of the international symposium on rock joints. Nick Barton and Ove Stephansson, Loen, Norway; 1990. p. 27-33.
[137] Isakov E, Ogilvie SR, Taylor CW, Glover PWJ. Fluid flow through rough fractures in rocks I: high resolution aperture determinations. EPSL 2001;191:267-82.
[138] Hopkins DL. The implications of joint deformation in analyzing the properties and behavoir of fractured rock masses, underground excavations, and faults. Int J Rock Mech &

Min Sci 2000;37:175-202.
[139] ISRM. Suggested methods for determining the uniaxial compressive strength of rock materials, 1972.
[140] ISRM. Suggested methods for determining tensile strength of rock materials. Int J Rock Mech Min Sci & Geomech Abstr 1978;15:99-103.
[141] ISRM. Suggested methods for determining water content, density, absorption and related properties and swelling and slake properties, 1972.
[142] Nemoto K, Watanabe N, Hirano N, Tsuchiya N. Direct measurement of contact area and stress dependence of anisotropic flow through rock fracture with heterogeneous aperture distribution. EPSL 2009;281:81–7.
[143] Goodman RE, Boyle W. Non-linear analysis for calulating the support of a rock block with dilatant joint faces. In: Proceedings in the 34th Geomechanics Colloquy. Salzburg, Austria; 1985. p. 203-8.
[144] Sabe S, Amadei B. Modelling rock joints under shear and normal loading. Int J Rock Mech Min Sci & Geomech Abstr 1992;29:267-78.
[145] Sabe S, amadei B. Modelling joint respose under constant or variable normal stiffness boundary conditions (Technical note). Int J Rock Mech Min Sci & Geomech Abstr 1990;27:213-7.
[146] Huang TH, Chang CS, Chao CY. Experimental and mathematical modeling for fracture of rock joint with regular asperities. Eng Fract Mech 2002;69:1977-96.
[147] International, society, for, rock, mechanics. Suggested methods for determining the uniaxial compressive strength of rock materials, 1972.
[148] International, society, for, rock, mechanics. Suggested methods for determining tensile strength of rock materials. Int J Rock Mech Min Sci & Geomech Abstr 1978;15:99-103.
[149] Engelder T. Aspects of asperity-surface interaction and surface damage of rocks during experimental frictional sliding. Pure Appl Geophys 1978;116:705-16.
[150] Olsson WA. The effect of slip on the flow of fluid through a fracture. Geophys Res Lett 1992;19(6):541-3.
[151] Teufel LW. Permeability changes during shear deformation of fractured rock. In: Proceedings of the 28th US symposium on rock mechanics. Tusson, Arizona; 1987. p. 473-80.